2009

Validation Of Quickscat Radiometer (qrad) Microwave Brightness Temperture Measurments

Rafik Hanna
University of Central Florida

VALIDATION OF QUICKSCAT RADIOMETER (QRAD) MICROWAVE BRIGHTNESS TEMPERTURE MEASURMENTS

by

RAFIK HANNA
B.S. Banha Higher Institute of Technology, 1994
M.S. University of Central Florida, 2007

A dissertation submitted in partial fulfillment of the requirements
for the degree of Doctor of Philosophy
in the School of Electrical Engineering and Computer Science
in the College of Computer Engineering and Computer Science
at the University of Central Florida
Orlando, Florida

Summer Term
2009

Major Professor: W. Linwood Jones

ABSTRACT

After the launch of NASA's SeaWinds scatterometer in 1999, a radiometer function was implemented in the Science Ground Data Processing Systems to allow the measurement of the earth's microwave brightness temperature. This dissertation presents results of a comprehensive validation to assess the quality of QRad brightness temperature measurements using near-simultaneous ocean Tb comparisons between the SeaWinds on QuikSCAT (QRad) and WindSat polarimetric radiometer on Coriolis. WindSat was selected because it is a well calibrated radiometer that has many suitable collocations with QuikSCAT; and it has a 10.7 GHz channel, which is close to QRad frequency of 13.4 GHz. Brightness temperature normalizations were made for WindSat before comparison to account for expected differences in *Tb* with QRad because of incidence angle and channel frequency differences.

Brightness temperatures for nine months during 2005 and 2006 were spatially collocated for rain-free homogeneous ocean scenes (match-ups) within 1° latitude x longitude boxes and within a ± 60 minute window. To ensure high quality comparison, these collocations were quality controlled and edited to remove non-homogenous ocean scenes and/or transient environmental conditions, including rain contamination. WindSat and QRad *Tb's* were averaged within 1° boxes and these were used for the radiometric inter-calibration analysis on a monthly basis. Results show that QRad calibrations are stable in the mean within ± 2K over the yearly seasonal cycle.

To my Wife

Gina Hanna

ACKNOWLEDGMENTS

This dissertation would not be possible without the guidance and assistance from many people. First and foremost, I would like to extend my deepest appreciation to Professor W. Linwood Jones, my professor and advisor who has patiently mentored and provided me guidance throughout my graduate study. Dr. Jones provided me with the invaluable opportunity of sharing in his teaching experiences. Through this experience, he taught me how to combine research into teaching. In addition, I am thankful for the financial assistance he provided me throughout my tenure in the program. I would not be where I am today without him. I also want to thank Mr. James Johnson for editing my dissertation and my colleagues at the Central Florida Remote Sensing Lab, especially Pete, Salem, Suleiman and Ruba. Their help, support, and friendship will never be forgotten.

TABLE OF CONTENTS

LIST OF FIGURES

LIST OF TABLES

LIST OF ACRONYMS/ABBREVIATIONS

ADEOS	Advanced Earth Observing Satellite (JAXA)
AMSR	Advanced Microwave Scanning Radiometer
DMSP	Defense Meteorological Satellite Program
GDAS	Global Data Assimilation System
GMF	Geophysical Model Function
JAXA	Japan Aerospace Exploration Agency (formerly NASDA)
JPL	Jet Propulsion Laboratory
LEO	Low Earth Orbit
NASA	National Aeronautics and Space Administration
NASDA	National Space Development Agency (currently JAXA)
NCEP	National Centers for Environmental Prediction
NESDIS	National Environmental Satellite, Data, and Information Service
NWP	Numerical Weather Prediction
QuikSCAT	Quick Scatterometer
SSM/I	Special Sensor Microwave/Imager
SST	Sea Surface Temperature
WVC	Wind Vector Cell

CHAPTER 1: INTRODUCTION

1.1 Background

In 1999, NASA launched the QuikSCAT satellite with the SeaWinds Scatterometer on-board and began the mission to fill a wind vector measurements gap caused by the loss of data from the NASA Scatterometer (NSCAT) on the ADEOS-1 satellite when ADEOS-1 power subsystem failed in June 1997. SeaWinds on QuikSCAT continues to provide the only NASA scatterometer wind speed and direction measurements available today. Since the launch of QuikSCAT, the Central Florida Remote Sensing Lab (CFRSL), at UCF, has been developing SeaWinds algorithms for improving the identification of rain contamination in wind measurements. This dissertation is the latest extension of that work.

There are major differences between NSCAT and SeaWinds that enabled the identification of rain contaminated wind measurements for SeaWinds. First, NSCAT used six stationary fan-beam antennas, but SeaWinds employed two conically scanning pencil beams, one H polarization and the other V, from a rotating parabolic dish antenna. The NSCAT fan beam systems used Doppler processing to resolve scatterometer measurement cells on the surface, whereas SeaWinds illuminates distinct, beam limited measurement cells. This allows for the use of a receiver noise measurement to estimate surface brightness temperature, T_b, and the corresponding brightness temperature along the line-of-sight of each wind vector cell, and therefore rain contamination.

Second the SeaWinds receiver was designed with this noise measurement in mind, providing 2 signal paths, or channels, so that the echo signal and noise signal could be separated out of the received signal-plus-noise. In 2001, after the launch of the QuikSCAT satellite, a data processing algorithm was developed by CFRSL [1, 2] that enabled SeaWinds to measure the ocean brightness temperature corresponding to each wind vector cell. The motivation for this work was to provide a means of identifying, or "flagging," rain contamination cell-by-cell. The idea behind the algorithm was to use the transfer functions of the two channels, each with its own gain and bandwidth, to separate signal and noise and use noise-only to infer brightness temperature. According to the CFRSL specifications, this radiometric measurement, known as the QuikSCAT Radiometer (QRad) was implemented by the Jet Propulsion Laboratory (JPL) in the Science Ground Data Processing Systems, and brightness temperature was incorporated into the L2A radar backscatter science data product.

In 2001, CFRSL developed the initial algorithm for inferring SeaWinds instantaneous oceanic rain rate using microwave brightness temperatures measured by QRad. The algorithm was based on the correlation of QRad with the corresponding rain rates retrieved from the Tropical Rainfall Measurement Mission (TRMM) Microwave Imager (TMI) [3, 4]. JPL has implemented this algorithm into the Science Ground Data Processing Systems and incorporated estimated rain rate into the QuikSCAT L2B wind vector data product. This allows users of L2B data to both identify rain contamination and to use quantified rain rate to evaluate rain effects on wind vector measurements [5].

Most recently CFRSL has improved the rain rate algorithm by using the correlation between the radar backscatter (active) with T_b (passive measurements) from SeaWinds and simultaneously rain rate retrievals for TMI [6, 7], which resulted in slight improvement in estimating rain rate from SeaWinds measurements.

Since the rain rate algorithm is based on estimated microwave brightness temperatures, it is very important to evaluate and validate QRad's measurement of Tb; therefore, the focus of this dissertation is to evaluate, validate, and characterize the radiometric performance of QRad. In particular, a method was developed to allow inter-satellite radiometric calibration of QRad T_b's by comparison to selected WindSat channels and provide a validated QRad radiometric transfer function. Also, previously observed time dependent biases during eclipse were characterized, and antenna pattern effects on ocean T_b at land/ocean boundaries were assessed.

1.2 QRad Calibration

This dissertation presents the first comprehensive evaluation and characterization of QRad radiometric performance. It includes an evaluation of QRad brightness temperatures over the oceans for a one-year period to establish the long-term accuracy and stability of QRad. The evaluation method that was used was based in near-simultaneous inter-satellite ocean Tb comparisons between the SeaWinds on QuikSCAT (QRad) and the WindSat polarimetric radiometer on Coriolis. The Tb comparisons were made during both the continuously sunlit and the eclipse orbits. Studies were also

conducted to determine antenna pattern effects on measurements near land/ocean boundaries, and to identify error sources in the QRad algorithm.

1.2.1 WindSat Comparisons

The primary QRad Tb calibration was conducted over oceans during continuous sunlit orbits (February through mid-November). The purpose of this calibration was to establish absolute QRad's brightness temperatures (T_b) accuracy, to estimate the mean brightness temperatures biases relative to WindSat observation, and to establish QRad's radiometric precision (NEDT). Brightness temperatures during July 2005 through June 2006 were spatially collocated for rain-free homogeneous ocean scenes (match-ups) within 1° latitude x longitude boxes and within a ± 60 minute window. WindSat and QRad Tb comparisons were performed on a monthly basis. A radiative transfer model, RTM, was used to normalize the WindSat measurements to the QRad frequency and incidence angles, and this RTM is validated using WindSat measurements as part of the normalization technique development.

1.2.2 Performance During Eclipse

Previous research shows that there are significant differences between radiometric calibrations for identical SeaWinds instruments on ADEOS-2 (SRad) and on QuikSCAT (QRad) [8, 9]. The SRad brightness temperatures varied systematically with orbital position (latitude) with an average bias of approximately 6 Kelvin between ascending and descending orbits. A hypothesis was developed that identified the most probable cause

for this discrepancy as the on-orbit thermal environment of the SeaWinds instrument. The QuikScat satellite is usually in continuous illumination of sunlight (~97%), but ADEOS-2's orbit underwent day (descending) and night (ascending) portions, which are subject to large (physical) temperature changes. The physical temperatures of the SeaWinds front-end losses are not measured; thus, errors are introduced by the modeled physical temperatures in the QRad Algorithm.

Each year from November 14th through January 30th, QuikSCAT experiences a short solar eclipse on every orbit. For the duration of these periods, the rapid temperature transient (from sunlight to night) will cause time varying radiometer biases. This data is compared to WindSat and examined for similar effects to those experienced by SRad in order to characterize QRad performance during eclipse.

1.2.3 Algorithm Error Analyses

This dissertation investigates the cause of systematic Tb calibration biases and identifies the reason within the QRad Tb algorithm. The eclipse results were analyzed to determine probable error sources due to the SeaWinds front-end thermal environment and losses, data near land/ocean boundaries were analyzed to quantify biases due to antenna pattern effects, and measurements over land were used to tune a gain normalization factor in the algorithm that affects the estimate of signal–noise.

The temperature of the SeaWinds reflector and feed are not measured on-orbit. In the QRad transfer function, the physical temperature for the front-end loss is assumed to be

equal to the measured rotary-joint temperature, although the rotary-joint resides in a thermally controlled environment. Thus, the large transient physical temperature swings of the feed horns and platform waveguide are most likely underestimated during the solar eclipses, causing the difficulty with QRad maintaining radiometric calibration during eclipse.

The QRad measured brightness temperature is the result of the convolution of the SeaWinds antenna radiation pattern $F_n(\theta,\Phi)$ with the apparent brightness temperature of the scene over the sphere surrounding the antenna. For ocean brightness temperatures near land or sea ice, there may be significant T_b contributions due to sidelobes viewing radiometrically hot land or ice. QRad radiometric biases (QRad – WindSat_normalized) in 0.25° pixels over a ten-day period in August 2005 along the west coast of North America were examined to assess antenna pattern effects as a function of distance from shore.

Measurements over land were used to tune the value of a quantity called the gain normalization factor, β, used in the QRad algorithm. The algorithm basically returns an estimate of observed T_b from a measurement of the differential energy between echo and noise for SeaWinds, and β determines the amount of echo to be subtracted from noise. Since the echo over land is approximately 5 times that over the ocean, the sensitivity of estimated T_b to the value of β is magnified, so WindSat comparisons over land were used to tune β in the algorithm.

These calibration procedures and results are presented as described in the next section.

1.3 Dissertation Organization

This dissertation consists of 5 chapters, including this introduction. Chapter 2 discusses the QuikSCAT Radiometer Apparent Brightness Temperature Algorithm. This includes a full discription of SeaWinds instrument on QuikSCAT, an overview of mocrowave radiometry, total power radiometer techniqes, and the radiometeric transfer function for QRad. Chapter three is the description of the results of previous QRad calibrations and current inter-sattelite caliberation of QRad using the normalized WindSat measurements. This includes a description of the Radiative Transfer Model (RTM) used for Tb normalization for the WindSat data, and discussion of the normalization results. Chapter 4 includes all of the results of the QRad calibration exercises for sunlit and eclipse orbits, for open ocean and near land, and for measurements strictly over land. Chapter 5 summarizes these results and provides conclusions, as appropriate. Finally, there are recommendations for extending the research that has been accomplished in this dissertation.

CHAPTER 2: QUIKSCAT RADIOMETER APPARENT BRIGHTNESS TEMPERATURE ALGORITHM

Since June 1999, the SeaWinds scatterometer has operated on the QuikSCAT satellite in a sun-synchronous polar orbit. SeaWinds has a wide swath that covers nearly 90% of the earth daily, and the measurement geometry is shown in Fig 2.1. Two polarizations (H-pol, V-pol) are measured with a pencil beam, conically scanning antenna with two feeds, each feed corresponding to a different polarization and incidence angle at 46^{o} for H-pol and 54.1^{o} for V-pol. Because of its lower incidence angle, H-pol has a narrower swath width (1400 km) than does the V-pol (1800 km). The conical scan with dual polarization provides four independent backscatter measurements (forward and aft for both H-pol and V-pol) for wind vector cells (WVC) as shown in Fig 2.2.

The QuikSCAT radiometric (QRad) measurements are implemented with ground signal processing of SeaWinds received noise for both V-pol and H-pol, this signal processing algorithm description is the subject of this chapter.

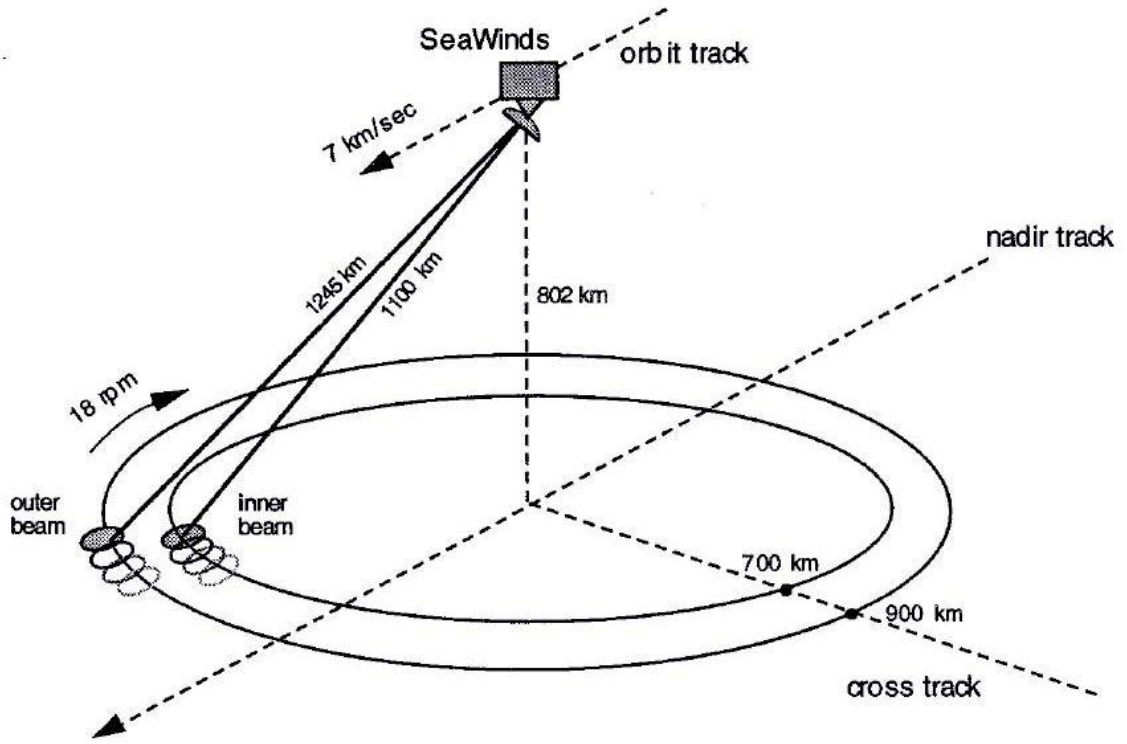

Fig 2.1: Geometry of the SeaWinds Scatterometer on QuikSCAT.

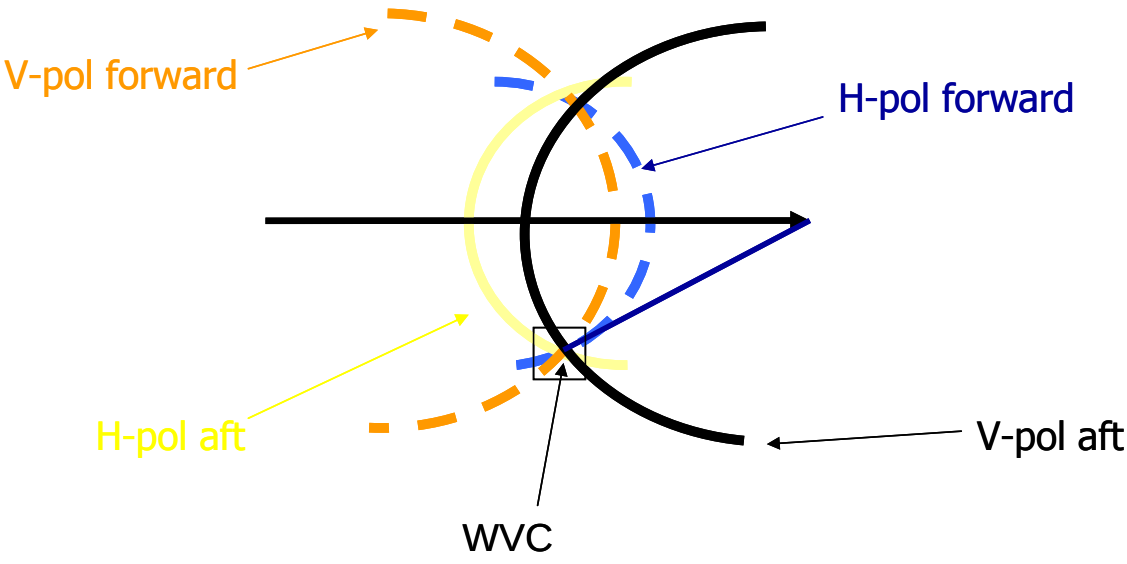

Fig 2.2: WVC sampling by dual polarized forward and aft looking antenna beams.

2.1 Microwave Brightness Temperature

The energy received by a microwave radiometer is due to natural noise emission by the scene that is collected by the antenna. The power (P) emitted by a medium in the microwave region is directly proportion to its physical temperature (T_{phy}) as described by the Rayleigh-Jeans radiation law. For an ideal blackbody scene, the power received by the antenna is

$$P_{Blackbody} = k\, T_{phy}\, B \tag{2-1}$$

where k is the Boltzman's constant, and B is the radiometer bandwidth.

For natural scenes, which are not blackbodies, the emission (P_{media}) is less than that of a blackbody for the same physical temperature. For these cases we define the radiometric emission efficiency or emissivity to be

$$e = P_{media} / P_{Blackbody} \leq 1 \tag{2-2}$$

and the radiometric brightness temperature T_b is defined

$$T_b = e\, T_{phy} \tag{2-3}$$

Thus, the brightness temperature is the effective "noise temperature" of the media that results in the measured emission power.

2.2 Total Power Radiometer

A simplified block diagram of a total power radiometer consists of an antenna, RF amplifier, square-law detector and an integrator as shown in Fig 2.3. The apparent brightness temperature collected by the antenna is input to the receiver and is amplified along with internally generated receiver noise. The receiver brightness temperature (power) output is a function of the system noise temperature (T_{sys}), receiver bandwidth (B) and receiver gain (G):

$$T_{out} = k * T_{sys} * B * G \tag{2-4}$$

where k is Boltzmann's constant.

The system brightness temperature is the sum of apparent (antenna) brightness (T_{ap}) temperature and internal receiver noise (T_{rec}),

$$T_{sys} = T_{ap} + T_{rec} \tag{2-5}$$

The dc output of the square-law detector is linearly proportional to its input brightness temperature (power); and this is followed by a low-pass filter (integrator) to remove the ac noise component in the output. The integrator output voltage is a scaled version of the receiver output brightness temperature (T_{out})

$$V_{out} = C_d * T_{out} \tag{2-6}$$

where C_d is the detector constant.

The total power radiometer calibration procedure for establishing the receiver transfer function is usually completed in two steps (see Fig. 2.4):

1. The antenna is replaced by a calibration noise source with known noise temperature T_{cal}

2. Since the output voltage is linearly related to the calibration temperature, it suffices to measure V_{out} at two known noise temperatures (T_{hot} and T_{cold})

The square-law (power) detector yields a linear equation for the calibration transfer function as shown in Fig. 2.4:

$$V_{out} = C_d * G\,(T_{cal} + T_{rec}) \tag{2.7}$$

The integrator reduces the level of the ac component of noise to yield a standard deviation equal to:

$$\Delta T = T_{sys} / (B * \tau)^{1/2} \tag{2.8}$$

where τ is the integration time and ΔT is the standard deviation of the integrator output, which is known as the precision of the total power radiometer measurement.

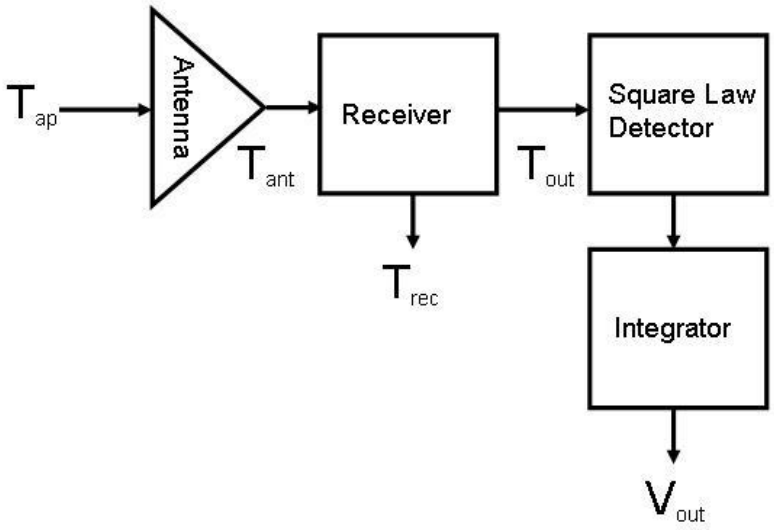

Fig 2.3: Total Power Radiometer.

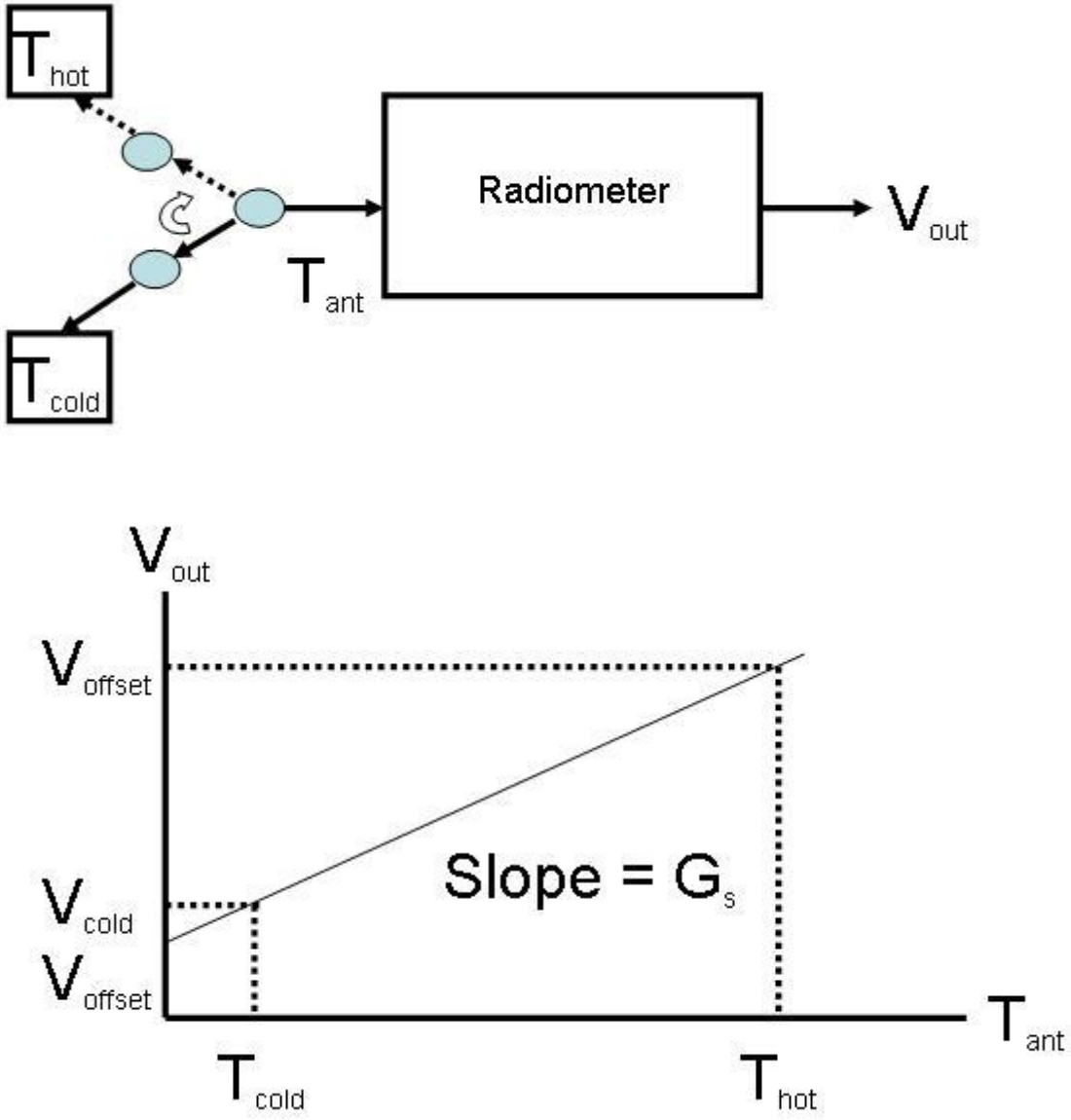

Fig 2.4: The Radiometer calibration.

2.3 QuikSCAT Radiometric Measurements

Radars sensors typically make only relative power measurements; but microwave scatterometers make absolute received power measurements (similar to total power radiometers). Because of this, it was possible to implement the QuikSCAT radiometer (QRad) function, and shortly after launch, the measurement functions were expanded to include brightness temperature of the oceans [1]. This change involved no new hardware, only additional signal processing of available data in the JPL Science Data Processing System Level-1A and Level-1B science data records. The QuikSCAT radiometer (QRad) simplified block diagram (shown in Fig 2.5) is used to develop the QRad transfer function. For simplicity, non-essential hardware components (e.g., the transmitter) are omitted and other details changed to create an equivalent functional signal flow diagram.

For the SeaWinds scatterometer, there are two parallel receiver channels: wideband (1 MHz, ”noise channel”) and narrow band (250 KHz, ”echo channel”). The signal (radar echo) plus blackbody noise are received from the target (i.e., the ocean surface) and measured in the echo channel. Also, simultaneously both blackbody noise and radar echo are received and measured in the overlapping noise channel. This results in about -6 dB reduction in the signal-to-noise ratio in the “noise channel” compared to the “echo channel”. For scatterometer signal processing, it is possible to use these two channel received powers to remove the noise power and solve for the echo received power. Thus, the normalized difference of these measurements from the two channels is equivalent the signal (surface backscatter) without the noise. For the QRad processing, the procedure is

reversed to yield the antenna noise without the signal present [1, 2], which will be discussed later in this chapter.

From a functional stand point, QRad is configured as a total power radiometer with four major parts: an antenna, a microwave switch assembly, a receiver and a power-detector/integrator. The simplified block diagram (Fig. 2.5) illustrates these components with their internal dissipative losses identified.

The radiometer Antenna Subsystem consists of a one-meter diameter parabolic dish reflector, with two offset feeds for conical beams and a spin motor assembly. In the antenna assembly there are three dissipative losses modeled:

1. *Lf,* feed assembly losses (horn and waveguide)
2. *Lrj,* microwave rotary joint loss
3. *Lwg,* platform waveguide loss between the antenna and the SeaWinds Electronic Subsystem (SES), which contains the switch assembly and the receiver electronics.

In Fig. 2.5, the front-end loss (*L1*) is the sum of L*f* , *Lrj*, and *Lwg*, and *A* and *B* refer to the inner and outer beam respectively.

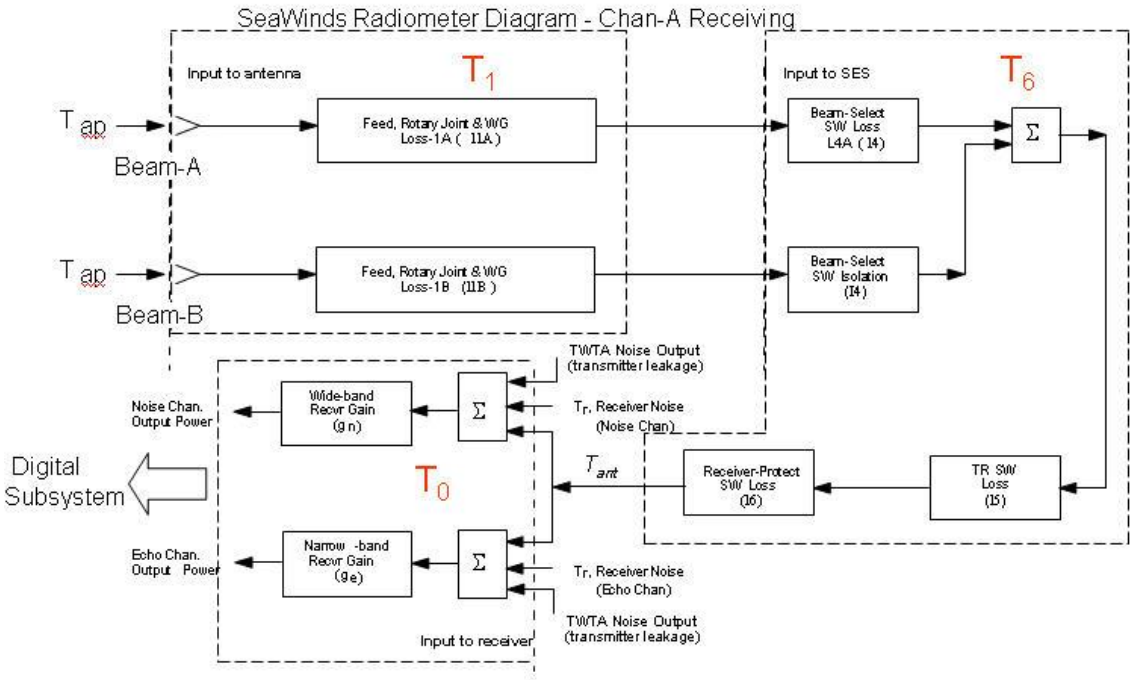

Fig 2.5: The equivalent simplified block diagram for the QuikSCAT Radiometer.

The switch assembly comprises three microwave circulator switches:

2. *L4*, beam select switch loss
3. *L5*, transmit/receive switch loss
4. *L6*, receiver protect switch loss

The receiver consists of a low noise amplifier, frequency down-converter and an IF frequency amplifier, followed by a power splitter with two parallel receiver channels. The echo and noise channels are connected to the SeaWinds Digital Subsystem, where they are converted into digital counts using an A/D converter and passed through digital

filters. The filter outputs are power detected using a Fast Fourier Transform and the squaring of the spectral components.

2.4 QRad Transfer Function

For scatterometer ocean backscatter measurements, the received echo signal plus noise is measured simultaneously in two overlapping channels as shown in Fig 2.6: a narrow band (echo) channel with a bandwidth of 250 KHz and a wider-band (noise) channel with a bandwidth of 1 MHz. The output power of the echo channel (Pe) and noise channel (Pn) are:

$$P_e = g_{re} * P_s * L_{eff} + g_{re} * T_{eff} * B_e * \mathrm{k}$$
$$P_n = g_{rn} * P_s * L_{eff} + g_{rn} * T_{eff} * B_n * \mathrm{k} \quad (2\text{-}9)$$

where

g_{rn} is the noise channel power gain

g_{re} is the echo channel power gain

B_n is the noise channel bandwidth

B_e is the echo channel bandwidth

P_s is the radar echo signal power

L_{eff} is the total loss between the antenna and the receiver input

k is boltzman's constant

T_{eff} is the system noise temperature at the receiver input

In (2-9), the first term is the echo signal power at the receiver output, and the second term is the noise power at the receiver output. The ratio of the bandwidths and gains of the noise and echo channels are respectively defined as

$$\alpha = \frac{B_n}{B_e} \quad \text{and} \quad \beta = \frac{g_{r_n}}{g_{r_e}} \tag{2-10}$$

It should be noted that the majority of the receiver gain is common to both the echo and noise channels and that the differential gain is determined by the insertion loss of digital filters, following the power splitter.

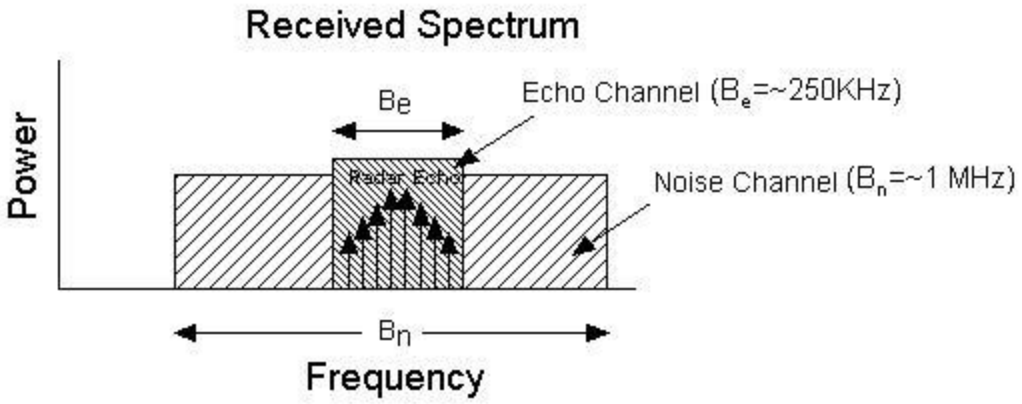

Fig 2.6: The received power spectrum for Echo and Noise channels.

Also note that both channels have the same radar echo and the noise power density input, but the output noise powers differ because of different receiver gains and bandwidths. To estimate the signal power, the echo channel is used; and the noise (in the echo channel) is

estimated and subtracting to improve the signal-to-noise ratio. The output noise power of the echo channel, after suitable weighting by the gain and bandwidth ratios, is

$$N_e = \frac{\beta * P_e - P_n}{\beta - \alpha * \beta} = \left(\frac{1}{1-\alpha}\right) * \left(P_e - \frac{P_n}{\beta}\right) \tag{2-11}$$

For the radiometer measurement, the excess noise (N_x) is defined as the output noise power in the noise channel contributed by the input noise density outside of the overlapping echo channel bandwidth (see Fig. 2.7). In terms of N_e , this is

$$N_x = (\alpha - 1) * \beta * N_e \tag{2-12}$$

and N_x in terms of measured receiver outputs, P_e and P_n , is

$$N_x = P_n - \beta * P_e = N_0 * (B_n - B_e) * g_n \tag{2-13}$$

where

N_o is the input noise power density = $k*T_{eff}$

Solving for the effective temperature yields

$$T_{eff} = \frac{N_x}{k * g_n * (B_n - B_e)} \tag{2-14}$$

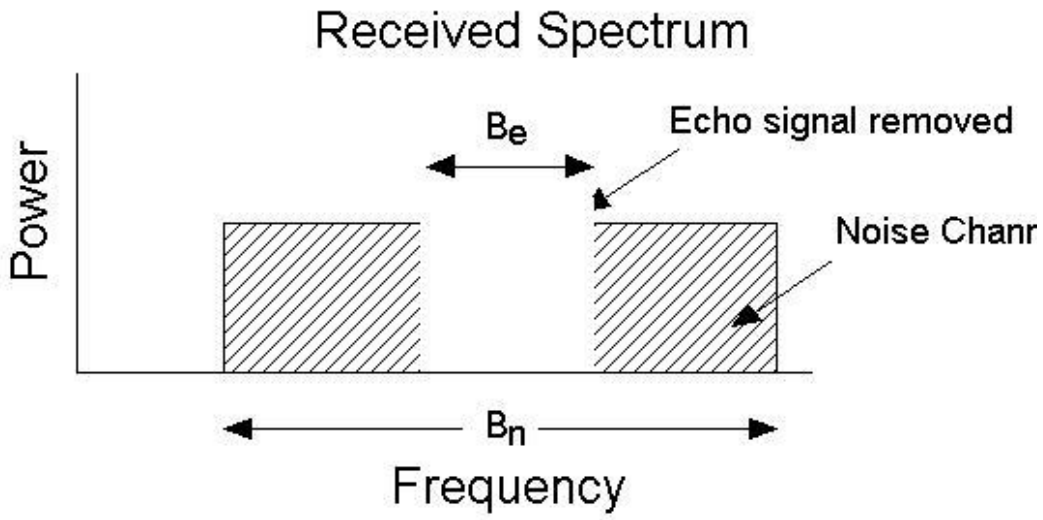

Fig 2.7: The "Noise channel" received noise power spectrum after subtracting Echo and Noise channels.

Fortunately, SeaWinds incorporated a periodic receiver gain calibration into its design. Once per antenna revolution, the input to the receiver was switched to an ambient temperature matched load (blackbody), and the echo and noise receiver channels output energies were measured. Thus, the noise channel gain is

$$g_n = \frac{E_{n\_cal}}{k * T_{Cal} * B_n * \tau} \tag{2-15}$$

where

E_{n_cal} is the noise channel energy during the calibrate interval

T_{cal} is the system noise temperature when connected to the matched load

τ is the integration time (1.8 msec)

2.5 QRad Inverse Transfer Function

The QRad transfer function and its inverse were developed by CFRSL during two master theses by Mehershahi [1] and Susanj [2]. In this section we summarize their work and explain the QRad T_b algorithm, which is used to process JPL QuikSCAT level-1A (L1A) and level-1B (L1B) data into polarized microwave brightness temperature collocated in wind vector cells in the level-2A (L2A) science data product.

According to Mehershahi, the QRad apparent brightness temperatures for the inner and outer beams (Taph and Tapv respectively) are

$$T_{aph} = \frac{C_{1A} * \left(\frac{T_{effh} - T_{wgh} - T_x - T_r}{Z} - D_A - Y_A \right)}{X_A} + C_{0A}, \text{K} \tag{2-16a}$$

$$T_{apv} = \frac{C_{1B} * \left(\frac{T_{effv} - T_{wgv} - T_x - T_r}{Z} - D_B - Y_B \right)}{X_B} + C_{0B}, \text{K} \tag{2-16b}$$

Referring to Fig. 2.5, all constants and instrument parameters are provided in Table 1.

Table 2-1: QRad Inverse Transfer Function: Constants and Instrument Parameters

Name	Description	Value
β	mean noise channel to echo channel gain ratio	2.917427
ε	mod-on to mod-off noise energy ratio	0.0617
a_{62}	2^{nd} order coefficient for calculating L6	1.4413e-6
a_{61}	1^{st} order coefficient for calculating L6	-1.8054e-3
a_{60}	0^{th} order coefficient for calculating L6	1.1213
a_{r1}	1^{st} order coefficient for calculating noise figure	5.333e-4
a_{r0}	0^{th} order coefficient for calculating noise figure	0.21226
B_n	noise channel bandwidth, Hz	9.8994e+05
c_{eff}	"effective_load_cal_factor"	0.952
C_{1A}	inner beam-A correlation slope	1.0
C_{0A}	inner beam-A offset, Kelvin	0.0
C_{1B}	outer beam-B correlation slope	1.0
C_{0B}	outer beam-B offset, Kelvin	0.0
$delT_A$	vertical to horizontal differential brightness, K	70.0
$delT_B$	horizontal to vertical differential brightness, K	-70.0
I4	beam-select switch isolation ratio	7.8886e-03
l1A	inner beam-A feed, rotary-joint & platform wg loss ratio	0.7730
l1B	outer beam-B feed, rotary-joint & platform wg loss ratio	0.7842
l4	beam-select switch loss ratio	0.9772
l5	transmit/receive switch loss ratio	0.9772
$T_{nf\text{-}ref}$	noise Fig reference temperature, K	290.0
T_x	transmitter leakage bias, K	2.0

In the remainder of this chapter, we define each variable in the inverse transfer function given in equations (2-16a) and (2-16b) respectively for H-pol and V-pol.

1. Receiver Noise (Radiometric) Temperature (T_r)

Prior to launch, the SeaWinds instrument was characterized during thermal vacuum testing at JPL. The receiver noise figure was measured over operating temperature from 0 C to +35 C, and based upon these test, the receiver noise figure (expressed as dB) is modeled as a linear function of the receiver physical temperature (T_0)

$$NF = \left[a_{r1} \times T_o + a_{ro}\right] \ , dB \tag{2-17}$$

where:

polynomial coefficients are given in Table 1

T_0 is the physical temperature of the receiver derived from the L1A data record.

The receiver noise temperature, T_r, is

$$T_r = (nf - 1) * T_{nf-ref}, \text{ K} \tag{2-18}$$

where:

$T_{nf\text{-}ref}$ is the noise figure reference temperature given in Table 1 (= 290 K)

"*nf*" is the noise figure expressed as a power ratio = $10^{(NF/10)}$.

For a typical orbit, the receiver noise temperatures is ~ 407 K.

2. Waveguide Radiometric Bias Temperature

The variable, T_{wg}, is the radiometric bias temperature contributed by the dissipative losses between the antenna aperture and the receiver input. For receiving beam-A, H-pol:

$$T_{wgh} = L6*\left[(1-L1A)*T_1*L4*L5 + (1-L4)*T_6*L5 + (1-L5)*T_6\right] + (1-L6)*T_6 \text{ , K} \tag{2-19}$$

where

losses: L1, L4, L5 and L6 are given in Table 1.

For receiving beam-B, V-pol:

$$T_{wgv} = L6*\left[(1-L1B)*T_1*L4*L5 + (1-L4)*T_6*L5 + (1-L5)*T_6\right] + (1-L6)*T_6, \text{ K} \tag{2-20}$$

where:

T_1 is the measured rotary-joint physical temperature from the L1A data record that is assumed as the physical temperature of the loss L1 given in Fig. 2-5. Over a typical orbit, T_1 is very stable with mean value of 309.5 ±0.5 K.

L6 is the receiver-protect switch loss, which was also measured during pre-launch thermal vacuum testing. Results show that *L6* is a function of the switch matrix physical temperature T_6

When expressed as a power ratio

$$L6 = a_{62} * T_6^2 + a_{61} * T_6 + a_{60} \ , \quad \text{ratio} \tag{2-21}$$

where

Coefficients for the polynomial are input constants in Table 1

Losses *L1A* and *L1B* are front-end losses for the inner and outer beam

L4 is the beam-select switch loss

L5 is the transmit/receive switch loss.

These four losses are constants given in Table 1 and T_6 is the measured transmit/receive switch physical temperature from the JPL L1A data record. For a typical orbit, T_6 is ~ 312.5 ± 0.5 K.

3. Transmitter Leakage Radiometric Temperature (T_x)

T_x is a constant radiometric temperature that characterizes the broadband noise leakage from the traveling wave tube transmitter into the receiver input. Its value is estimated to be 2 K and is provided as a constant in Table 1.

4. Effective System Noise Temperatures, T_{eff},

The effective (system) radiometric temperature calculation (T_{eff}) is

$$T_{effi} = \frac{(N_{xi} * T_{cal})}{\left(E_{n-cal} * \left(1 - 1/\alpha\right)\right)} \ , \ \text{K} \tag{2-22}$$

where

N_x is the excess noise defined as the weighted difference between the noise channel and echo channel output energies

$$N_{xi} = \left(E_{ni} - \beta * E_{ei}\right) * \frac{\alpha - 1}{\alpha - \left(1 + \varepsilon\right)}, \text{ digital number} \tag{2-23}$$

where

E_{n_cal} is the noise channel energy measured using the "load calibration" pulses from the L1A data product

i = "h" for inner beam and i = "v" for outer beam

Alpha (α) is the mean noise channel to echo channel bandwidth ratio (calculated in L1B processing)

Beta (β) is the mean noise channel to echo channel gain ratio given in Table 1

Epsilon (ε) is the mod-on to mod-off noise energy ratio given in Table 1

Echo energy (E_{ei}) is the sum of the 12 slice echo energies (power_dn), which is calculated in L1B processing.

$$E_{ei} = \sum_{j=1}^{12} power\_dn_j, \text{ digital number} \tag{2-24}$$

where

i = "*h*" for inner beam = *A* and i = "*v*" for outer beam = *B*

T_{cal} is the system noise temperature, when the receiver is connected to the matched load for the radiometric gain calibration

$$T_{cal} = (T_6 + T_r)/c_{eff}, \text{ K} \tag{2-25}$$

where

c_{eff} is the "effective_load_cal_factor", given in Table-1

T_6 is the measured transmit/receive switch physical temperature

T_r is receiver noise temperature calculated in (2-17)

5. Other Terms (X_A, X_B, Y_A, Y_B, Z_A, Z_B, and Z)

X-factor

There are separate "X-factors" for each antenna beam calculated as

$$X_A = L1A * L4 + L1B * I4, \text{ ratio} \quad (2\text{-}26a)$$

$$X_B = L1B * L4 + L1A * I4, \text{ ratio} \quad (2\text{-}26b)$$

where parameters are given in Table-1

D-factor

There are separate "D-factors" for each antenna beam calculated as

$$D_A = \Delta T_A * L1B * I4, \text{ K} \quad (2\text{-}27a)$$

$$D_B = \Delta T_B * L1A * I4, \text{ K} \quad (2\text{-}27b)$$

where parameters are given in Table-1

Y-factor

There are separate "Y-factors" for each antenna beam.

$$Y_A = (1 - L1B) * T_1 * I4, \text{ K} \quad (2\text{-}28a)$$

$$Y_B = (1 - L1A) * T_1 * I4, \text{ K} \quad (2\text{-}28b)$$

where parameters are given in Table-1

Z-factor

$$Z = L5 * L6, \quad \text{ratio} \tag{2-29}$$

where parameters are given in Table-1

In Chapter-3, we will discuss the validation of the QRad T_b algorithm using external inter-satellite radiometric calibrations.

CHAPTER 3: INTER-SATELLITE RADIOMETRIC CALIBRATION METHOD

3.1 Previous Approach for QRad Calibration

As mentioned previously, SeaWinds was designed as an active microwave scatterometer to measure wind speed and direction; and QRad does not have provisions for the usual two-point, hot and cold, absolute brightness temperature calibration [1, 2]. Fortunately, a single radiometric calibration is accommodated using an internal ambient temperature load at the receiver input, which enables the radiometric transfer function gain (slope) to be determined but not the absolute offset. The radiometric offset was established during a series of external on-orbit calibrations in 1999, 2000 & 2001, using selected rain-free ocean T_b measurement comparisons with the TRMM Microwave Imager (TMI).

3.1.1 External Radiometric Calibration Approach

Since QRad and TMI operate at different incident angles and frequencies, T_b normalizations were required before comparisons are made. Concerning channel frequencies used for the calibration, TMI operates at 10.7 and 19 GHz and QRad operates at 13.4 GHz. Also, the TMI incidence angle is 52.8° for all channels, whereas for QRad, the inner (H-pol) beam is 46° and the outer (V-pol) beam is 54°. To accomplish the normalization, a UCF radiative transfer model (RTM) was used to translate the

equivalent measurements from TMI to QRad. TMI T_b's were interpolated over frequency and extrapolated over incidence angle to create QRad equivalent T_b's using a spectral ratio (Sr) defined as

$$Sr = \frac{Tb_{13.4} - Tb_{10.7}}{Tb_{19.4} - Tb_{10.7}} \tag{2.30}$$

$$Tb_{13.4} = Tb_{10.7} + sr(Tb_{19.4} - Tb_{10.7}) \tag{2.31}$$

where $T_{b13.4}$ is the QRad "equivalent" T_b derived from TMI measurements.

Using the RTM, the spectral ratio is calculated using approximately 70,000 ocean/atmosphere environmental cases for both horizontal and vertical polarization. The spectral ratio was a function of the environmental parameters water vapor and wind speed, which were determined by match-ups of numerical weather models.

To perform radiometric calibration, global ocean T_b for QRad were compared with the equivalent $T_{b13.4}$ derived from TMI. QRad polarized T_b's were averaged for 3-days and a rain mask was applied to prevent any contamination caused by rain. Each dataset was earth gridded and averaged, and corresponding pixels (QRad-TMI) were compared and a statistical analysis performed.

3.1.2 QRad Radiometric Calibration Results

The following is a summary of the work previously performed at CFRSL [4, 8, 9, and 10]. An example of the linear regression scatter diagrams for QRad and $T_{b13.4}$ derived from TMI measurements is shown in Fig 3.1. Data are rain free, combined horizontal and

vertical polarization, three-day averaged ocean brightness temperatures. The symbols are binned and averaged QRad and TMI T_b*'s* and the error bars denote one standard deviation. The dashed line (the 45 degree line) is the perfect agreement (offset equal to zero and slope equal to unity) and the solid line shows the best-fit least square linear regression.

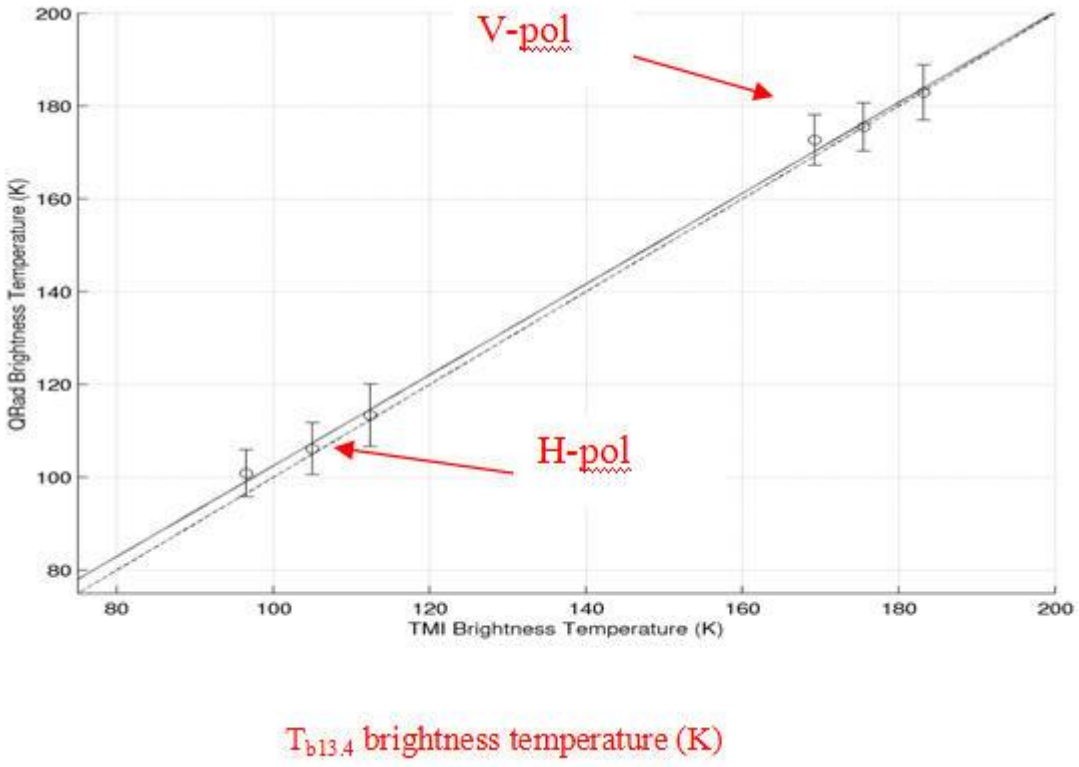

$T_{b13.4}$ brightness temperature (K)

Fig 3.1: Tb comparisons between $T_{b13.4}$ derived from TMI and QRad for 3 day averages. Solid line is best fit linear regression and dashed is 45°-line.

An example of the QRad T_b stability is illustrated in Fig 3.2, where the QRad average polarized T_b deviation (from the polarized time series mean) is displayed for Pacific Ocean repeating ground tracks. Over this two-year period, the rms difference about the

mean is 1.4 K for both polarizations, which demonstrates consistent and repeatable QRad *Tb's* [4].

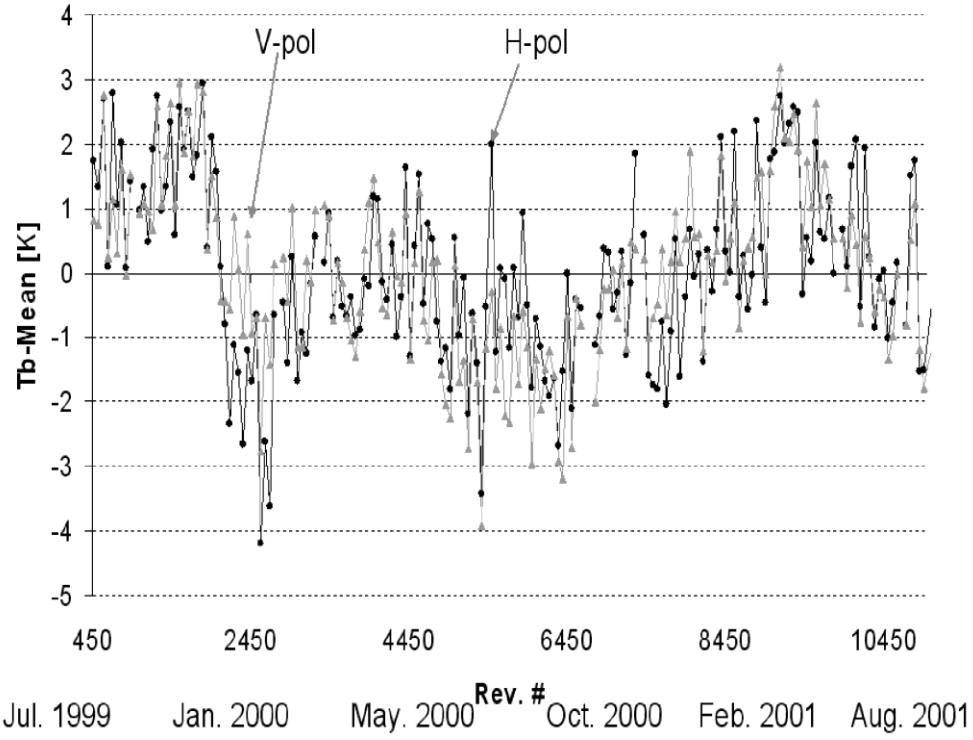

Fig 3.2: Brightness temperature deviation from the mean over the Pacific Ocean repeat ground tracks.

While these inter-satellite radiometric comparisons are encouraging, they have significant limitations and restrictions. First, TMI has coverage only exists between ± 35° latitude, so the calibration is not global in spatial extent. Also, the inter-comparisons have used only 3-day average T_b*'s* from TMI and QRad (instead of near simultaneous comparisons), so there are questions about the temporal stability and the stationary of the statistics. Finally, it has not been possible to evaluate QRad measurements during the eclipse periods, which occur during the winter season at latitudes above 60° and which are subjected to significant instrument physical temperature transients. Therefore, this dissertation

provides the first comprehensive radiometric evaluation using near simultaneous radiometric comparisons with the WindSat satellite radiometer.

3.2 QRad Brightness Temperature Validation Using WindSat

Following the approach of Hong [11, 12] and modifications by Gopalan [13, 14], we validate the QRad brightness temperature algorithm and the QuikSCAT L2A T_b product using an inter-satellite radiometric calibration technique. This approach involves the inter-comparison of two satellite radiometers (with different design characteristics) using near simultaneous brightness temperature observations of the same homogeneous earth scene. To assess the quality of the QRad instrument, we compare the QRad L2A T_b with the near simultaneous and collocated ocean brightness temperature observations from WindSat, which serves as the calibration standard.

WindSat is a polarimetric radiometer that operates at multiple frequencies at 6.8, 10.7, 18.7, 23.8 and 37 GHz, which was launched in January 2003 on the Coriolis Satellite into a Sun-Synchronous orbit [15]. WindSat has a total of 22 channels comprising five widely spaced frequencies: three frequencies (10.7, 18.7 and 37 GHz) are fully polarimetric (six Stokes polarizations) and two frequencies (6.8 GHz and 23.8 GHz) are vertical (V-pol) and horizontal (H-pol) polarizations. In this dissertation, we are only concerned with 10.7V and 10.7H channels.

The WindSat conical spinning antenna has a 1.8m reflector with a cluster of 11 dual-polarized feedhorns producing 22 channel beams, which have incident angles ranging from 50° to 55°. WindSat channel characteristics are given in Table 1 and the physical configuration is shown in Fig 3.3.

Table 3-1. WindSat Characteristics

Channel (GHz)	Polarization	B.W (MHz)	Earth Incidence angle (degree)	Spatial resolution (km)	NEDT
6.8	V, H pol	125	53.5	40 x 60	0.48
10.7	V, H pol, +/- 45, L, R	300	50.3	25 x 38	0.37
18.7	V, H pol, +/- 45, L, R	750	55.3	16 x 27	0.39
23.8	V, H pol	500	53.0	12 x 20	0.55
37.0	V, H pol, +/- 45, L, R	2000	53.0	8 x 13	0.45

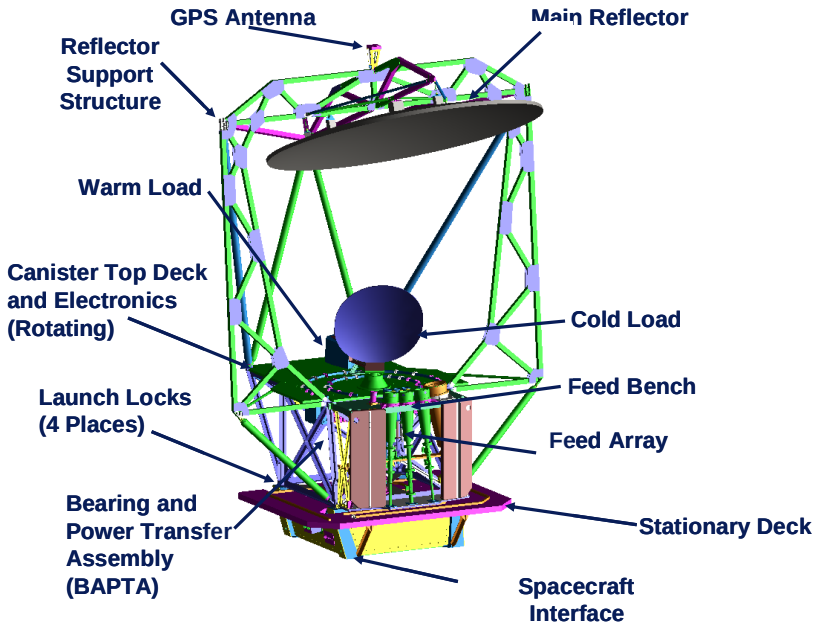

Fig 3.3: WindSat PayLoad Configuration from Gaiser [15].

The Coriolis satellite orbits the Earth at an altitude of 830 km in a sun-synchronous orbit (similar to QuikSCAT) and completes over 14 orbits per day. WindSat observations are made at 6 am and 6 pm local time (same as the local time for QRad). The main data products for WindSat are:

1. NRL Optimal Estimation EDRs
2. NOAA/NESDIS EDRs
3. WindSat SDRs (Brightness Temperatures)
4. Level 1C (L1C)

The Level 1C data are produced from the Sensor Data Record (SDR) and are used in the QRad Calibration. The WindSat 10.7 GHz Tb's (Horizontal and Vertical Polarization) are extracted from WindSat level 1C data set.

WindSat was selected in this calibration because it is a well calibrated radiometer [16] that has many suitable collocations with QuikSCAT (over ~ 400,000 oceanic collocations per month) and has a 10.7 GHz channel, which is close to QRad frequency of 13.4 GHz.

An example for a typical month (February 2006) collocation between QRad and WindSat is shown in Fig 3.4.

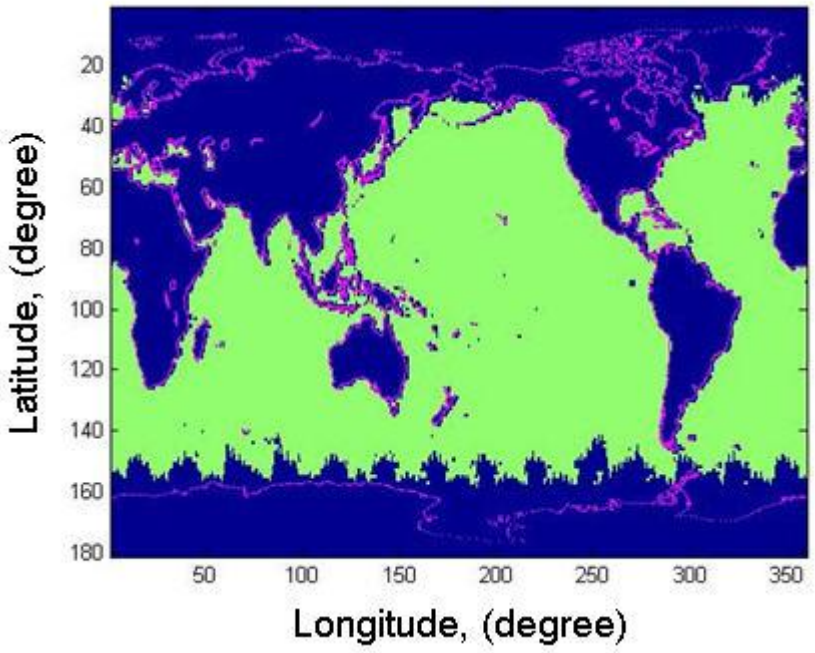

Fig 3.4: A typical one-month collocation between QRad and WindSat (February 2006).

The QRad operates at 13.4 GHz with incidence angles 54˚ (V-pol) and 46˚ (H-pol) and the closest WindSat channel is 10.7 GHz at an incidence angle of 50.3°. Since these radiometers are different, T_b normalizations (i.e. compensation for the difference in frequency and the incident angle between the QRad and WindSat) were required before comparisons were made. To accomplish this, a Radiative Transfer Model (RTM) for non-

raining oceanic scenes was used to transform the WindSat 10.7 GHz measurements to the equivalent at 13.4 GHz and the corresponding QRad incidence angles.

3.3 Data Sets and Match-ups

In this section, we describe the ocean brightness temperature dataset that has been used in the QRad calibration procedure. This comprises combined QRad, WindSat, and GDAS data for one year, July 2005 through June 2006.

3.3.1 QRad Data

Time ordered L2A and L2B QuikSCAT data products by orbit (provided by the Jet Propulsion Laboratory) are utilized in the QRad assessment. Each day has slightly greater than 14 orbits, which starts with an ascending pass, from the South Pole to the North Pole, followed by the descending pass. The Brightness temperatures (Horizontal and Vertical polarization) and the time of measurements are extracted from L2A data, while the location (latitude and longitude) for each measurements and QRad rain rate were obtained from L2B.

3.3.2 WindSat Data

The time ordered L1C data by orbits is produced by the Colorado State University. These L1C data were derived from the Sensor Data Record (SDR), which is a standard product for WindSat. The following parameters are inputs to QRad calibration:

1. The Brightness temperatures (Horizontal and Vertical polarization) at 10.7GHz channels
2. Time of measurements (day, hour, minute and second)
3. Location, latitude and longitude
4. Quality flags.

3.3.3 GDAS Data

All the environmental data needed in the RTM for T_b normalization purposes was provided by the NOAA global numerical weather model Global Data Assimilation System (GDAS) [17]. GDAS data is available every six hours (0000, 0600, 1200 and 1800 GMT) with spatial resolution of 1° (latitude/longitude). GDAS data provide sea surface temperature (SST), surface wind speed and direction, atmospheric temperature profile, relative humidity profile, cloud liquid water profile and geopotential heights for 26 constant pressure layers (between 1000 mb and 100 mb) for each 1° x 1° grid point.

3.3.4 Match-ups

Brightness temperatures for one year between July 2005 and June 2006 were spatially collocated for rain-free homogeneous ocean scenes, within 1° latitude x longitude boxes, and within a $\pm$ 60 minute window. A simplified block diagram illustrating this process of creating the match-up datasets is shown in Fig 3.5. A typical daily set of match-ups for ascending and descending passes provided wide geographic coverage as shown in Fig 3.6. To ensure high quality comparison, the standard deviation for WindSat T_b's were computed for each 1° box. Since high standard deviations are indicative of non-homogenous and/or transient environmental conditions, including rain contamination, the boxes were removed when standard deviations exceed 2 K for vertical polarization pol and 3 K for horizontal polarization. Also, to ensure good quality match ups (boxes), QRad rain retrievals from L2B were used to remove any 1° box with rain rate higher than zero. Further, individual 1° boxes were eliminated using a conservative land mask or when the collocated numerical weather model (GDAS) indicated high water vapor (> 60 mm). WindSat and QRad Tb's were averaged within 1° boxes and these were used for the radiometric inter-calibration analysis on a monthly basis as a function of latitude and separately for ascending and descending QRad passes.

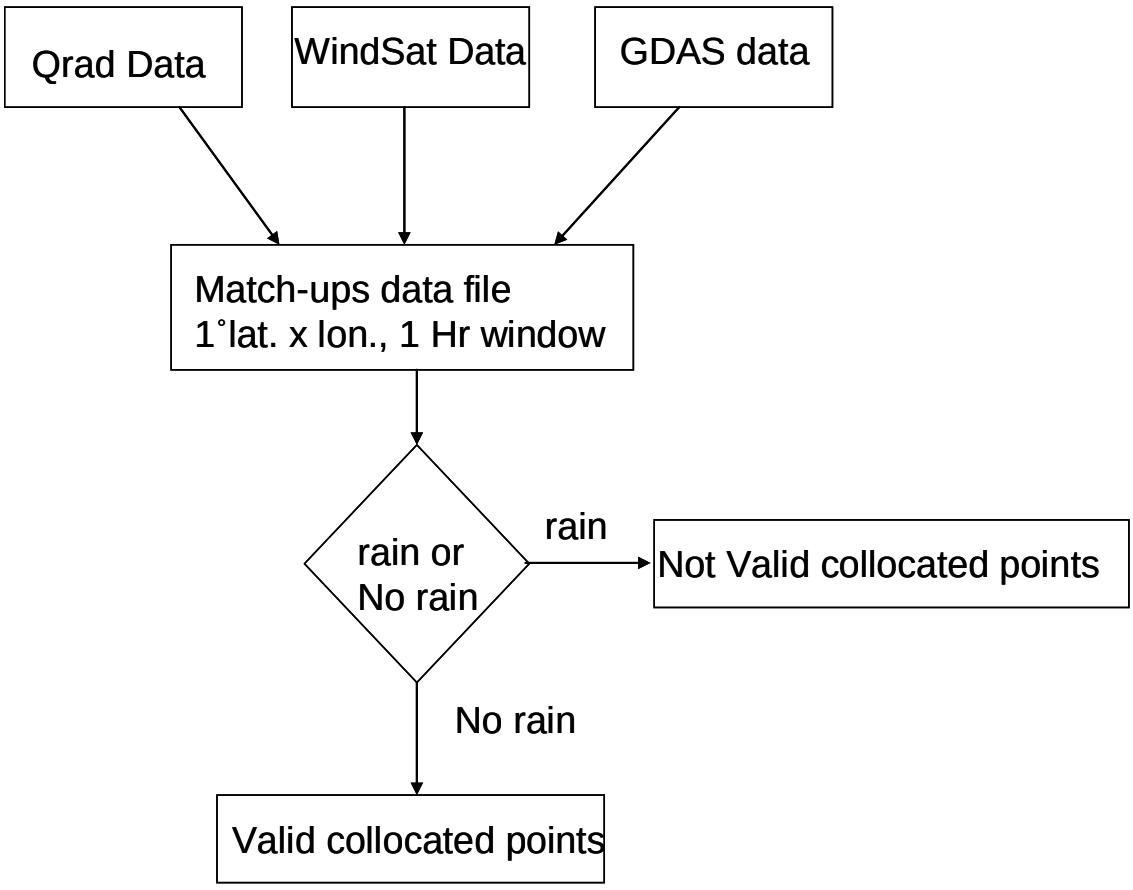

Fig. 3.5: Simplified block diagram for the match-ups.

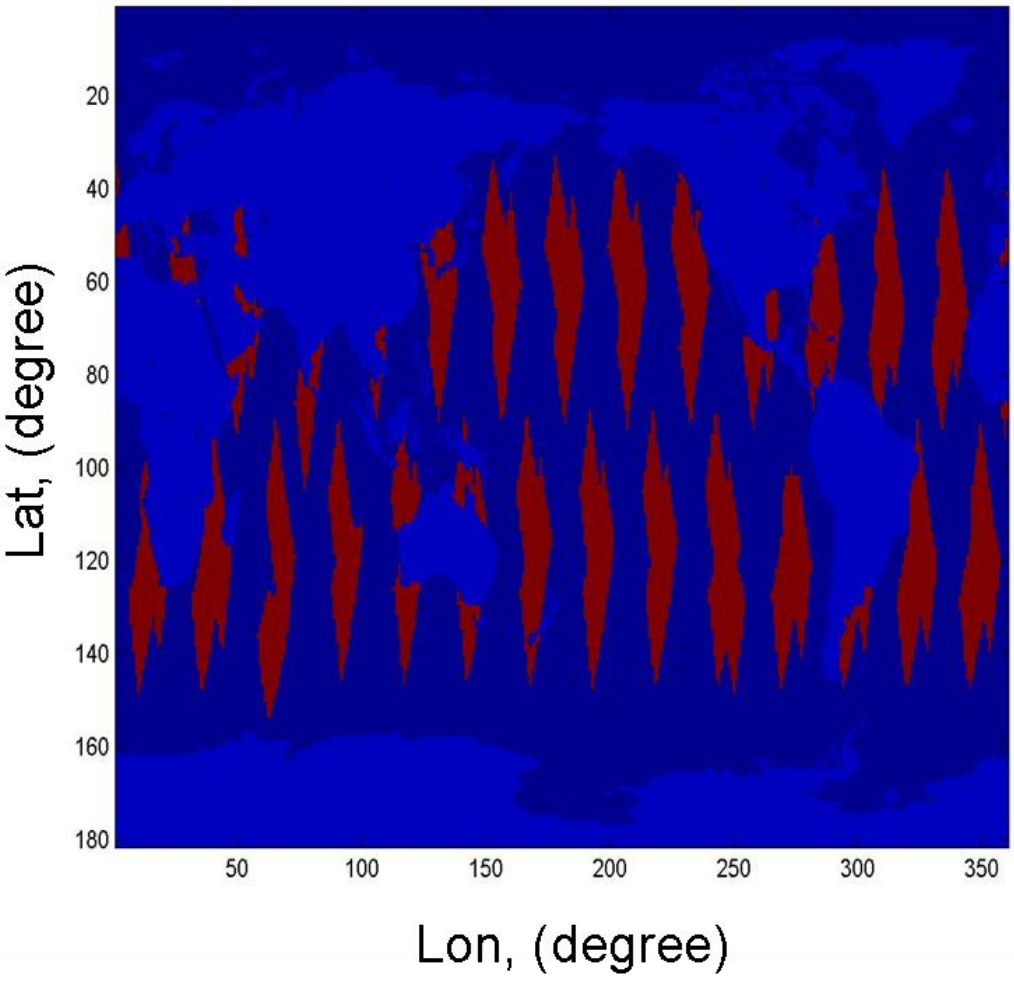

Fig.3.6: Typical one-day match-ups between QRad and WindSat for ± 60 minutes window (12/31/05).

3.4 Radiative Transfer Model

This section describes the radiative transfer model (RTM) [13, 14], which is used in this dissertation to estimates brightness temperature for a specific operating frequency and incidence angle given a match-up set of environmental parameters.

3.3.1 RTM Description

In general, radiative transfer theory states that the *Tb* measured by a space-borne radiometer is the linear sum of individual contributions from the atmosphere and surface [18]. Given that there is a high degree of homogeneity for the 1° match-up oceanic scenes, the radiative transfer model is a good fit for WindSat normalization.

The principal components that contribute to the apparent brightness temperature captured by typical radiometer antenna in space are shown in Fig 3.7. This apparent temperature is the sum of the 3 components which are T_{b_up} , $T_{b\_surface}$ and $T_{reflection}$ as given in Equation 3.1 and illustrated in Fig 3.7.

$$T_{apparent} = T_{b\_up} + \tau * (T_{b\_surface} + T_{reflection}) \tag{3-1}$$

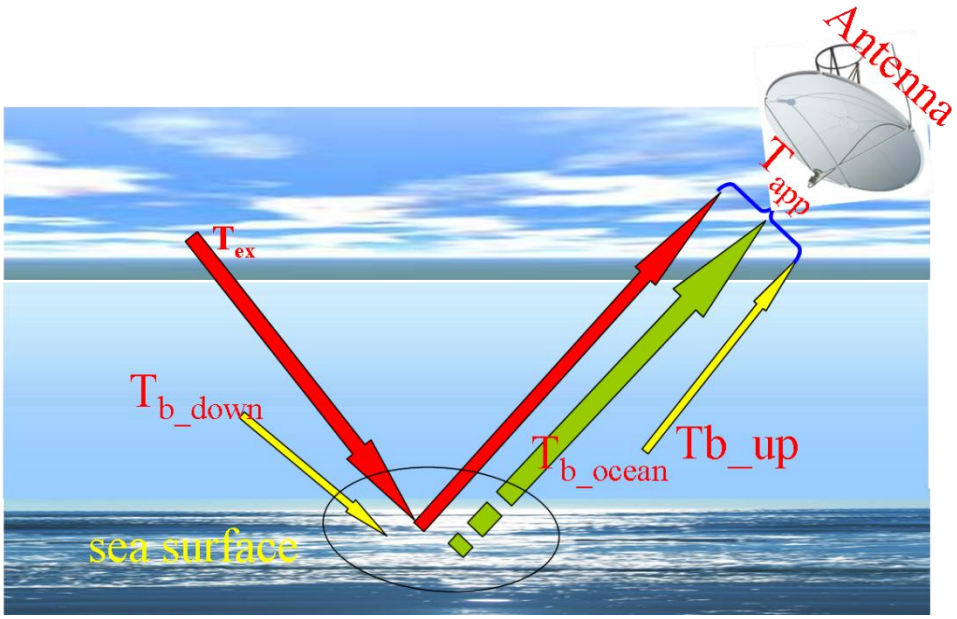

Fig 3.7: Radiative Transfer Model.

Below are the calculations for each of these components in the RTM:

1. The ocean surface reflects the sky brightness.

$$T_{reflection} = (1-\varepsilon) * T_{sky} \qquad (3-2)$$

where, ε is the ocean surface emissivity and (1- ε) is Fresnel power reflectivity. Sky brightness temperature, T_{sky} is defined as a sum of atmosphere down-welling and attenuated cold space brightness temperature.

$$T_{Sky} = \tau * T_{ex} + T_{b\_down} \qquad (3-3)$$

where τ is the atmospheric power transmissivity.

2. The ocean brightness temperature is obtained from the product between the surface emissivity (ε) and the sea surface temperature (SST) in Kelvin.

$$T_{b-surface} = \varepsilon * SST \qquad (3-4)$$

3. The upward T_{b_up} traveling atmospheric microwave radiation.

The microwave radiation is attenuated while propagating through the atmosphere. In the absence of rain, atmospheric emission and absorption are governed by three physical processes [19-23]:

1. Oxygen (O_2) absorption
2. Water vapor (WV) absorption
3. Rayleigh absorption by cloud liquid water (CLW) droplets

For sea surface emissivity, the Elsaesser model [24] was used to derive the ocean isotropic emissivity, and the sea water dielectric constant was based on the model of Meissner and Wentz [25].

All the environmental (geophysical) parameters needed to run the Radiative transfer model were obtained from the NOAA Global Data Assimilation System (GDAS) archive [17], which provides global information every six hours (i.e., 0000, 0600, 1200 and 1800 GMT) with 1° spatial resolution. The RTM provides atmospheric profiles of temperature, water vapor and pressure at twenty one levels in altitude; plus columnar cloud liquid water, sea surface temperature and ocean wind speed at 10 meter height. The GDAS's atmospheric profiles are interpolated to RTM's heights of the 100 layers, by employing a linear piece-wise distribution for temperature and exponential piece-wise distribution for

both water vapor and pressure. A uniform distribution is utilized for cloud liquid water. The heights of the clouds are obtained from ocean climatology. The monthly averaged salinity values were obtained from the National Oceanographic Data Center World Ocean Atlas salinity [26].

Finally, The main output for the RTM is the estimated brightness temperature at the defined operating frequency and incidence angle.

3.3.2 RTM Validation

To assess the ability of the RTM to accurately predict the WindSat brightness temperatures for normalization purposes, we compared measured and modeled WindSat T_b*'s* for both polarizations; and zonal averages were performed (over full 360˚ longitude) using 1° latitude bins. An example of zonal averaged T_b*'s* is given for February 2006 (typical month in winter season) in Fig 3.6, and results indicate excellent agreement over all latitudes between ±50°, which is important to consider QRad biases as a function of orbit position.

The total number of WindSat's observation used in RTM validation is ~200,000 measurements (before the zonal average). The number of collocation points for each one degree bin and its standard deviation are shown in Figs 3.7 and 3.8. These Figs show that there are more than 80,000 comparisons over ± 50° latitude with relatively few points (less than 200 points per degree bin) at higher latitudes (higher than 50 degree) which

cause poorer agreement as shown in Fig 3.8. Standard deviation for all the bins is less than 2 Kelvin as shown in Fig 3.10.

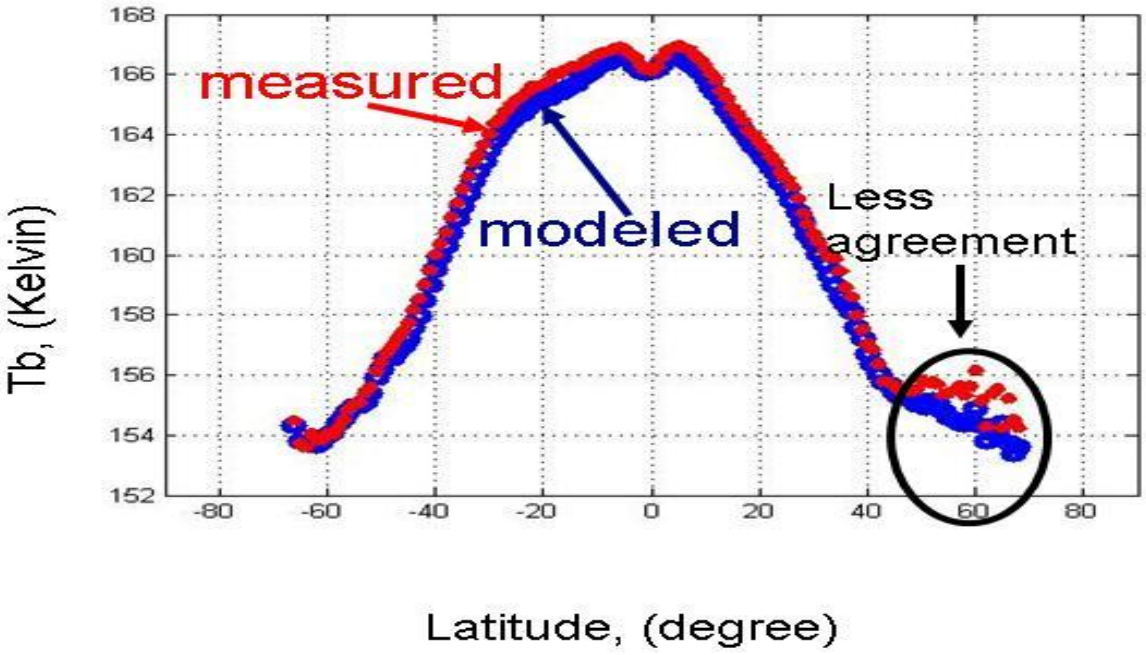

Fig 3.8: WindSat zonal averaged measured and modeled Tb's from collocated for 1° boxes during February 2006.

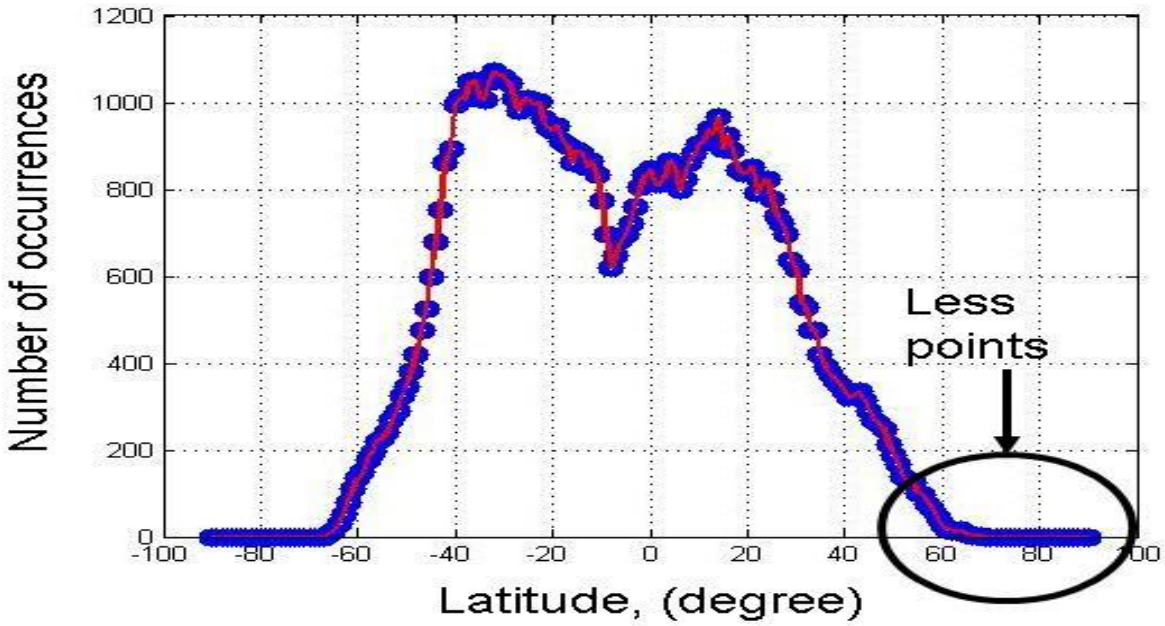

Fig 3.9: Number of the collocated points in each 1° box during February 2006.

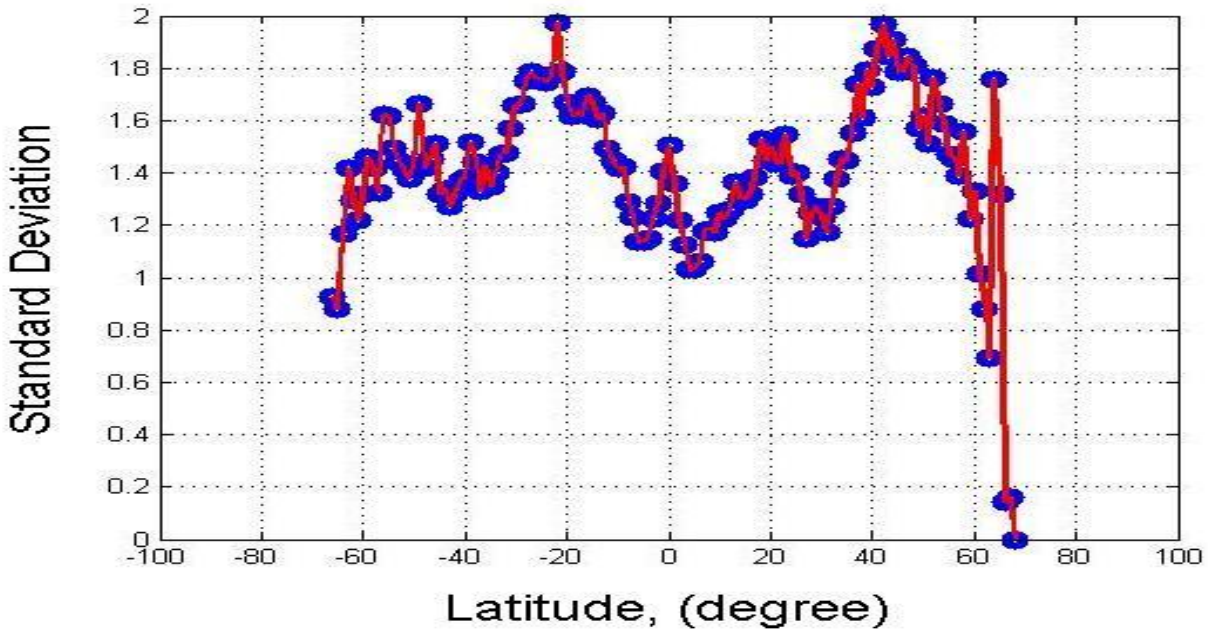

Fig 3.10: Standard deviation for each 1° box during February 2006.

To gain more confidence with the RTM, the same comparison was repeated for a different set of data (August 2005) from a different season (summer). The results were very consistent with the pervious one shown in month of February (winter season) and they illustrated in Figs 3.11-3.13.

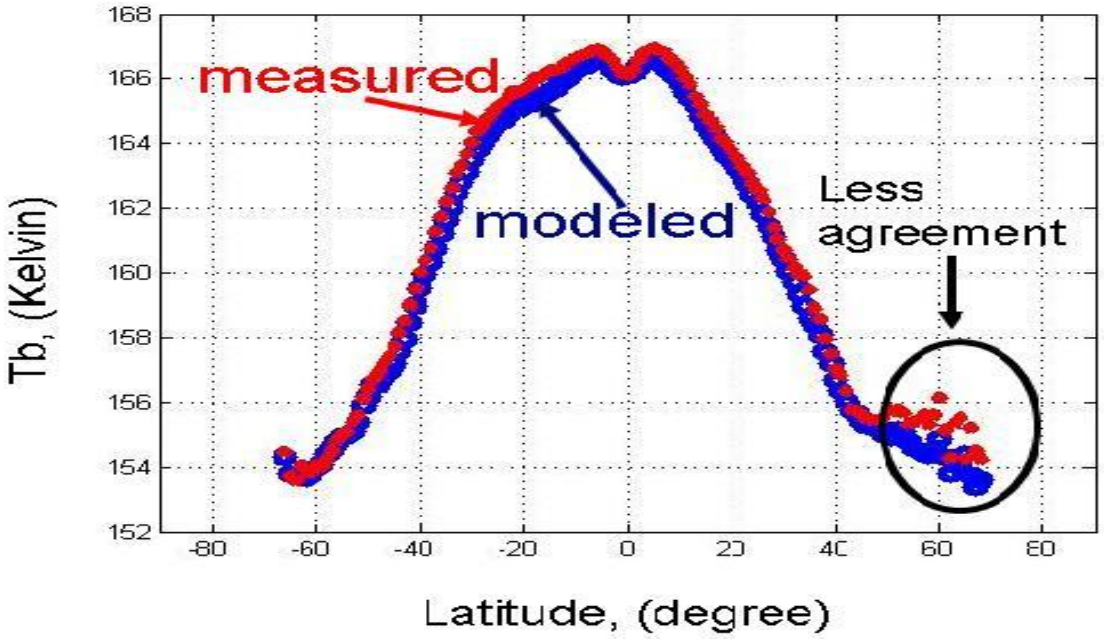

Fig 3.11: WindSat zonal averaged measured and modeled Tb's from collocated for 1° boxes during August 2005.

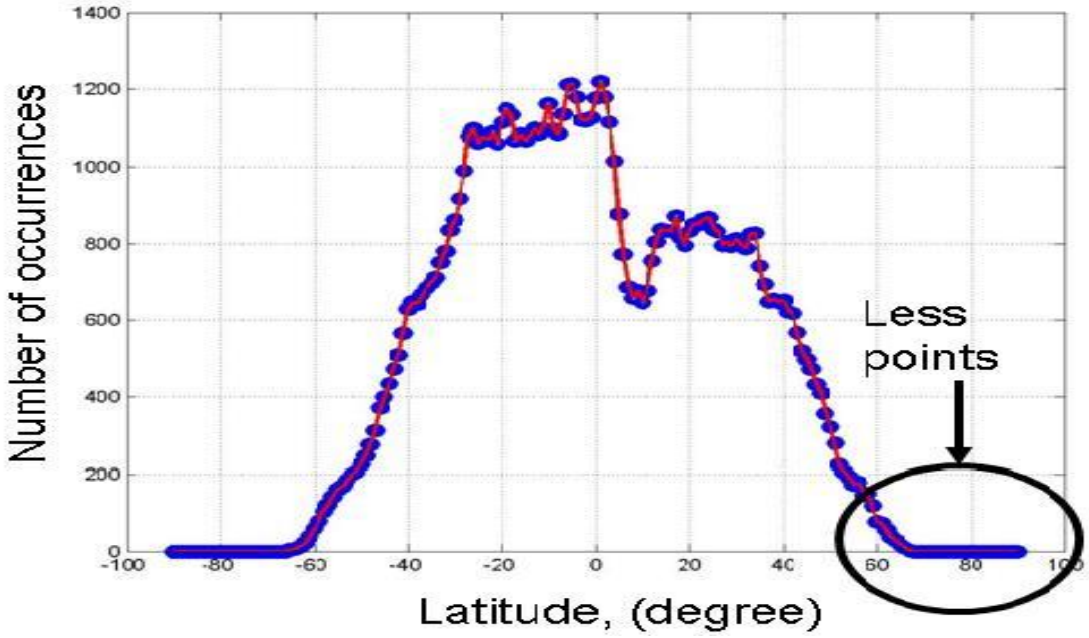

Fig 3.12: Number of the collocated points in each 1° box during August 2005.

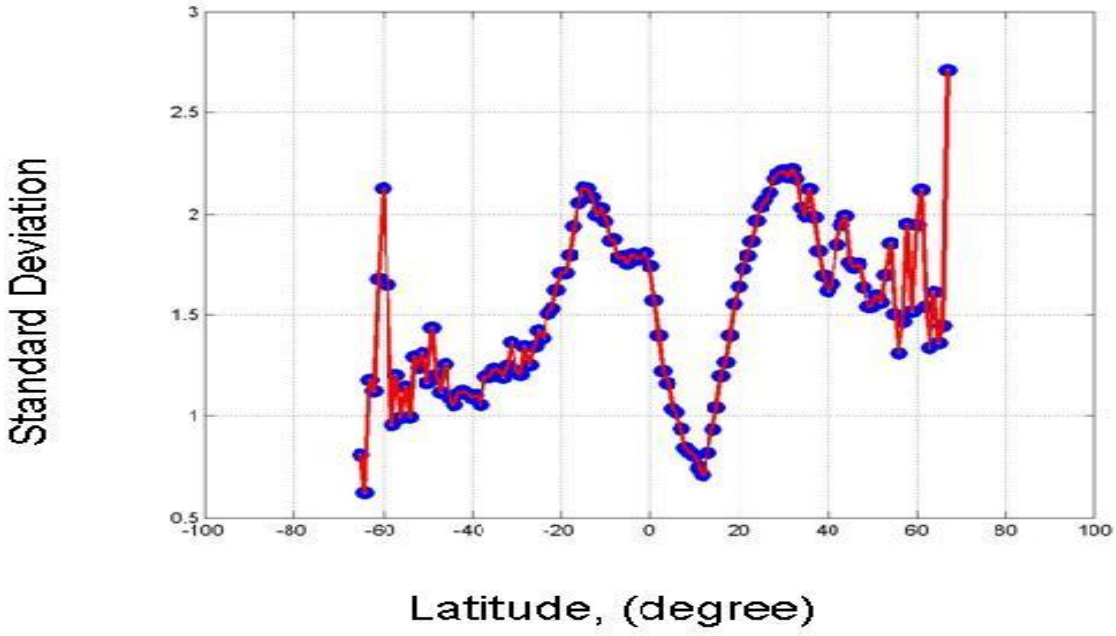

Fig 3.13: Standard deviation for each one degree box, (August 2005).

To estimate the magnitude of the RTM_bias (or Tb difference) in these comparisons, 215,000 of WindSat's *Tb* measurements in the month of February 2006 data were compared with the corresponding *Tb* estimated by the RTM. The differences between the measurement and the simulated (modeled) were zonal averaged over 1° latitude bins to determine the average value of RTM_bias, which is < ± 0.5 Kelvin as shown in Figs 3.14 and 3.15 for vertical and horizontal polarization, respectively.

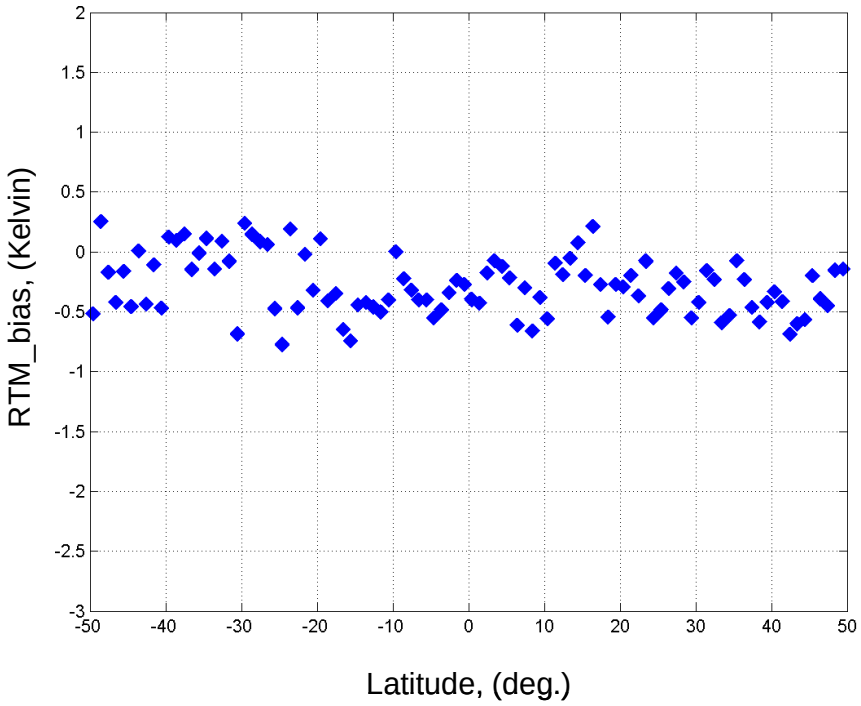

Fig 3.14: RTM_bias with respect to WindSat measurements at 10.7 GHz (V-pol), February 2006.

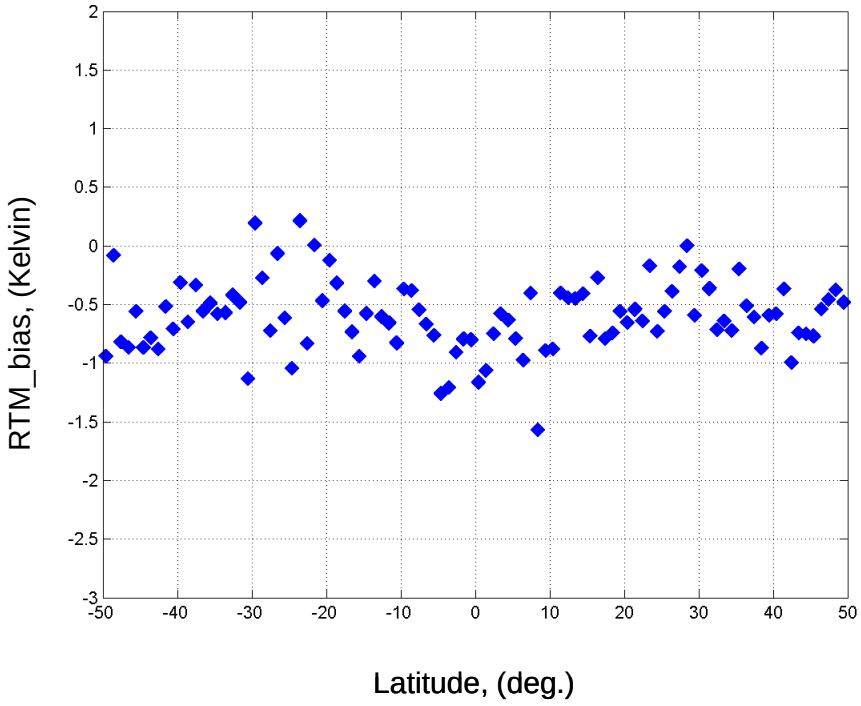

Fig 3.15: RTM_bias with respect to WindSat at 10.7 GHz (H-pol), February 2006.

The histogram of the differences between RTM results and the WindSat observation are Gaussian with mean value of -0.29 K and standard deviation of 1.01 for the vertical polarization and mean value of -0.59 K and standard deviation of 1.49 for the horizontal polarization. These histograms are shown in Figs 16 and 17.

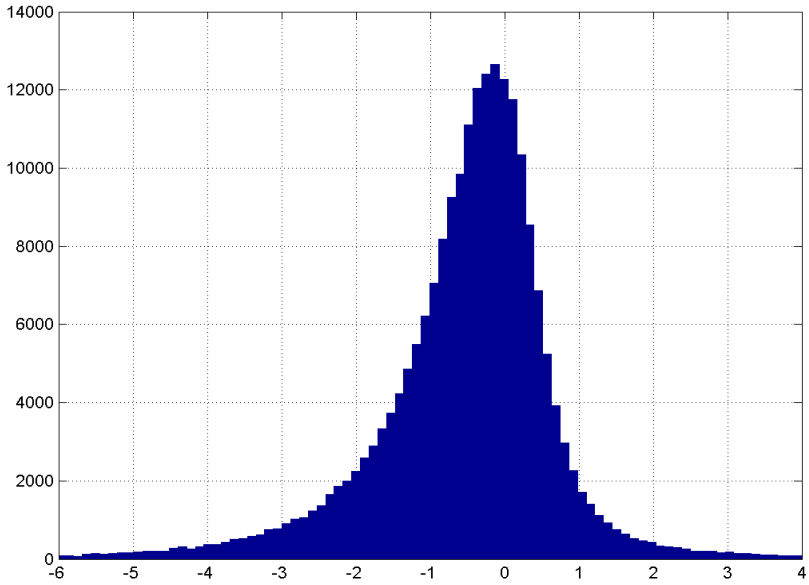

Fig 3.16: Histogram of RTM_bias for V-Pol with mean value of -0.29 K and standard deviation of 1.01.

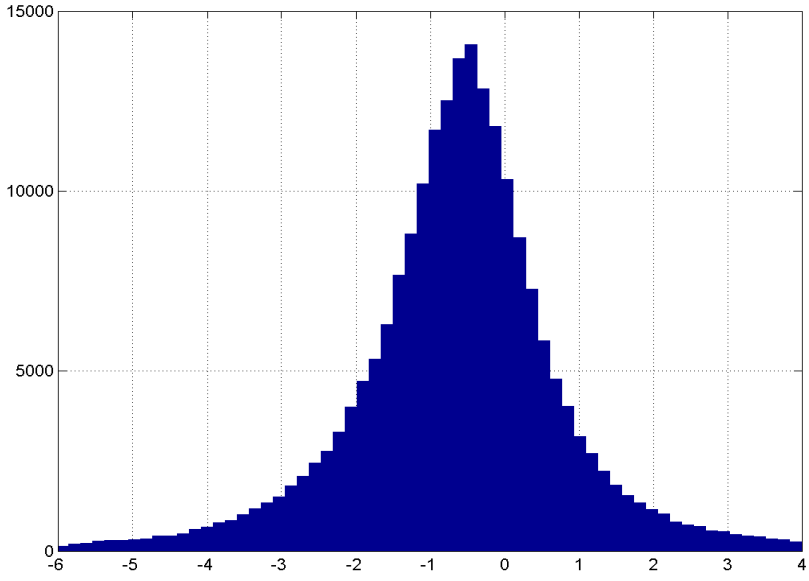

Fig 3.17: Histogram of RTM_bias for H-Pol with mean value of -0.59 K and standard deviation of 1.49.

Ideally, the RTM biases (the difference between the measured and RTM *Tb's*) should be independent of the true environmental parameters. Thus, the biases were plotted versus environmental parameters to verify this, and results are presented below for 10.7 GHz. Comparisons with water vapor and cloud liquid water are shown in Fig. 3.18, with SST and wind speed are shown in Fig. 3.19. Since the plots are essentially horizontal lines (zero slope), this proves that the RTM models the change in Tb with these significant environmental parameters correctly.

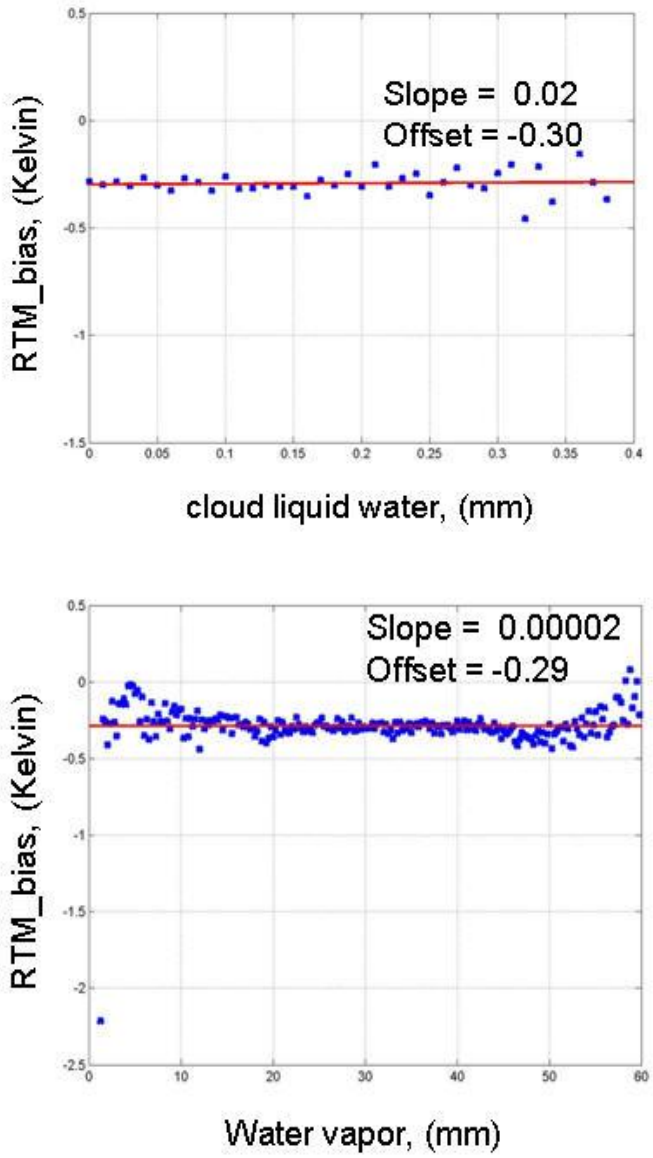

Fig 3.18: RTM bias validation using cloud liquid water and water vapor using month of February 2006.

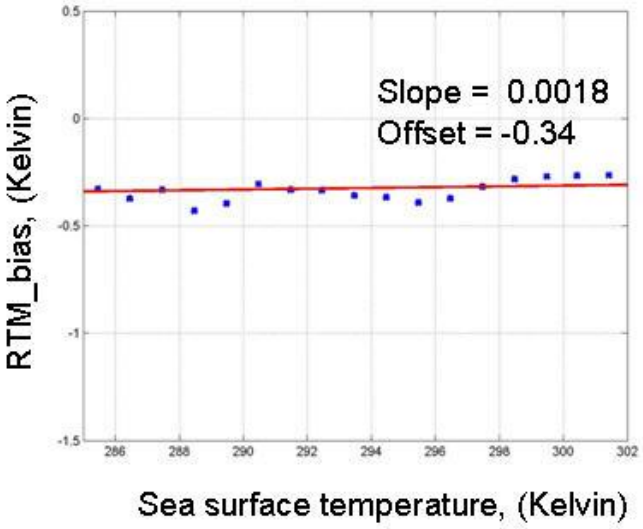

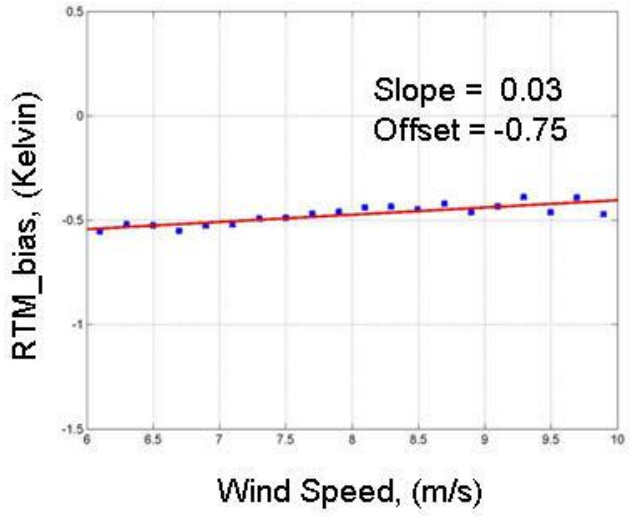

Fig 3.19: RTM validation using SST and wind speed using month of February 2006.

Thus, the suitability of the RTM model has been demonstrated by comparison with ~200,000 WindSat observations at 10.7 GHz, both H-pol and V-pol, which yield very small biases < 0.5 K. Further, these biases are independent of latitude, and there is no error correlation with the significant environmental parameters.

3.5 WindSat's Tb Normalization

Since QRad operates at 13.4 GHz with incidence angles 54˚ (V-pol) and 46˚ (H-pol) and the closest WindSat channel is 10.7 GHz at an incidence angle of 50.3°, WindSat T_b normalizations were required before QRad calibrations were made. To accomplish this, the (RTM) discussed in the previous section was used to transform the WindSat 10.7 GHz measurements to the equivalent at 13.4 GHz at the corresponding QRad incidence angles. The environmental parameter inputs for the RTM were obtained from the National Oceanic and Atmospheric Administration National Center for Environmental Prediction's Global Data Assimilation System (GDAS) data [17].

In the WindSat T_b normalization procedure, a difference parameter (ΔT_b) was computed and applied to the WindSat measurements before inter-comparison. The computed ΔT_b is the difference between the estimated brightness temperatures (using the RTM) for the parameters WindSat ($T_{b\text{-}WSsim}$) at 10.7 GHz and QRad parameters ($T_{b\text{-}QRsim}$) at 13.4 GHz for V and H pol. and is calculated as

$$\Delta T_{b\text{-}V} = T_{b\text{-QRsim-V}} - T_{b\text{-}WSsim\text{-}V} \quad (3\text{-}5a)$$

$$\Delta T_{b\text{-}H} = T_{b\text{-QRsim-H}} - T_{b\text{-}WSsim\text{-}H,} \quad (3\text{-}5b)$$

The normalization parameter ΔT_b computed for 1° latitude bins and averaged over 360° longitudes is shown in Fig 3.20. The ΔT_b ranges from 12 - 14 K for V-pol and 9 - 11 K for H-pol.

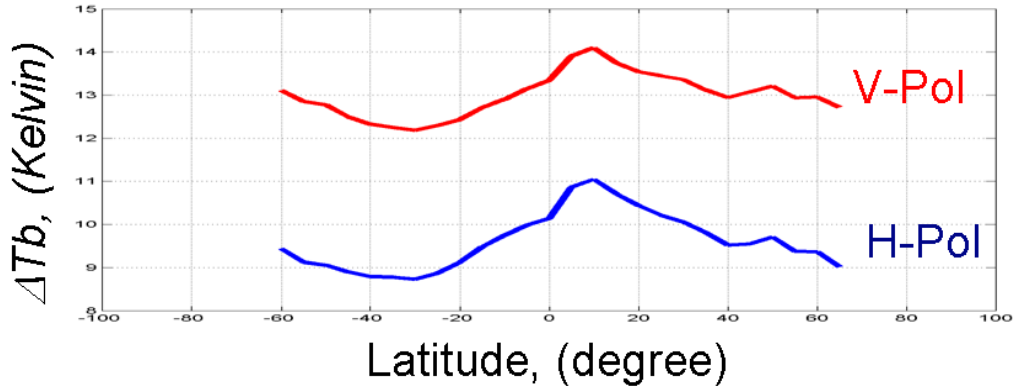

Fig 3.20a: The delta Tb *(*ΔTb) for 1° latitude zonal averages.

For each 1° box, the average WindSat 10.7 GHz brightness temperature *(*$<T_{b\_WSmeas}>$*)* was normalized to compensate for the difference in center frequency and the incidence angle using

$$T_{b\_WSnorm\text{-}V} = <T_{b\_WSmea\text{-}V}> + \Delta T_{b\text{-}V} \quad (3\text{-}6a)$$

$$T_{b\_WSnorm\text{-}H} = <T_{b\_WSmea\text{-}H}> + \Delta T_{b\text{-}H} \quad (3\text{-}6b)$$

Both $T_{b\_WSnorm\text{-}V}$ and $T_{b\_WSnorm\text{-}H}$ results are shown in Figs 3.19b and 3.19c.

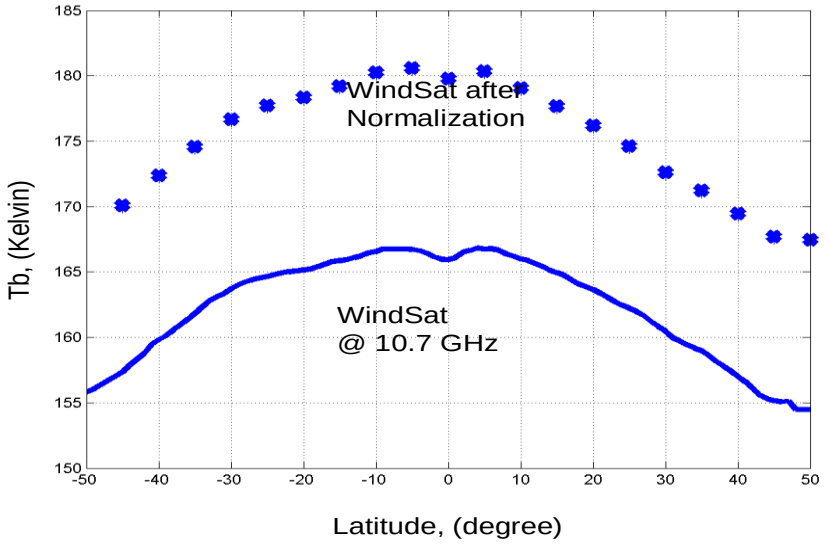

Fig 3.20b: WindSat normalization for V-pol @ 13.4 GHz and 54° incidence.

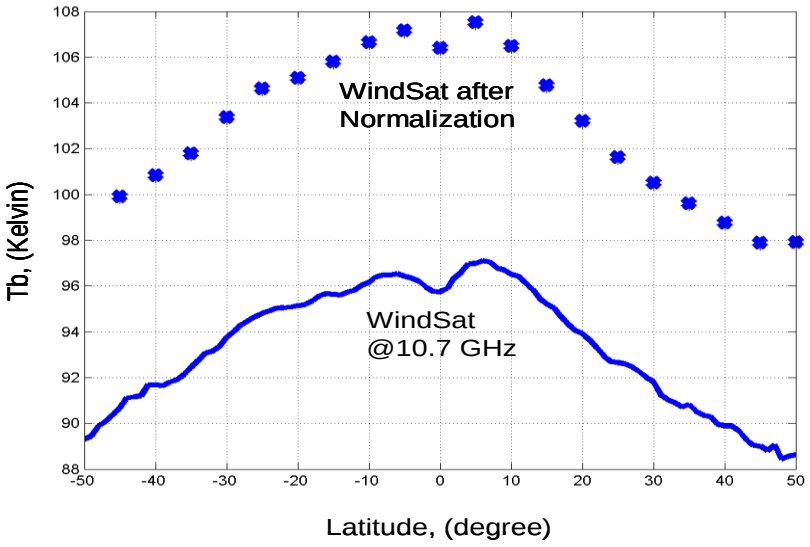

Fig. 3:20c: WindSat normalization for H-pol @ 13.4 GHz and 46° incidence.

The inter-satellite radiometric calibration can be performed, after the normalization of WindSat T_b s. The results of this radiometric calibration will be presented in Chapter 4.

CHAPTER 4: QRAD CALIBRATION RESULTS

As described in Chapter 3, approximately 200,000 near-simultaneous match-ups with the WindSat satellite radiometer were used to determine the QRad radiometric bias. Our hypothesis is that the QRad radiometric biases are solely instrument related and are independent of the scene geophysical parameters. As such, biases should have a highly repeatable pattern over any given orbit, which may vary slowly over seasons because of the instrument physical temperature changes with solar heating. Because of the poor QRad radiometric precision (ΔT_b = 27K/pulse), considerable averaging was required to extract the mean bias value, which was calculated in 1° x 1° boxes and averaged spatially (over longitude). This approach was adopted to preserve the changes which may occur in time within the period of an orbit (corresponding to changes in latitude). Further, we adopted the conservative approach of selecting only the "best points" for inter-satellite radiometric calibration; therefore strict quality control editing was applied to eliminate transient and non-homogeneous ocean brightness temperature scenes.

4.1 Primary Calibration during Continuous Sunlit Orbits

This primary calibration for QRad was performed during a 9½ month period from January 31 through November 13 during continuous sunlit orbits that represent ~80% of the total observation time. Brightness temperatures for several months during 2005 and

2006 were spatially collocated for rain-free homogeneous ocean scenes (match-ups) within 1° latitude x 1° longitude boxes and within a ± 60 minute window. To ensure high quality comparisons, these collocations were quality controlled and edited to remove non-homogenous ocean scenes and/or transient environmental conditions, including rain contamination. WindSat and QRad Tb's were averaged within 1° boxes and were used for the radiometric inter-calibration analysis on a monthly basis.

As described in Section 3.5, the difference between the T_{b_WSnorm} and the box-averaged QRad measurement ($<T_{b\_QRmeas}>$) is defined as the radiometric bias

$$T_b\_\text{bias} = <T_{b\_QRmeas}> - T_{b\_WSnorm} \tag{4-1}$$

where: T_{b_WSnorm} is the normalized WindSat T_b, see (3.6a) and (3.6b).

The first inter-comparison of QRad and WindSat Tb's are made at the highest overall level using the entire dataset of global ocean brightness temperatures for two months (August 2005 and February 2006), and results are presented as histograms in Figs. 4.1 and 4.2. These histograms of the 1° box average Tb's for both QRad and WindSat (before and after normalization) comprise nearly 170,000 match-ups. Overall, results are quite encouraging in that the histograms are very similar in the mean after the appropriate Tb normalization (to remove frequency and incidence angle differences). However, one should note that the width (standard deviation) of the histograms are much wider for QRad, which is the result of its large delta-Tb. Results shown in Table 1 illustrate that

after Tb normalization there are reasonably small differences in the mean ocean brightness temperatures between QRad and WindSat, which indicates that the QRad radiometric calibration is basically stable (within a couple of Kelvin) over one-month periods.

Table 4-1 QRad Global Ocean Tb Histogram Comparison with WindSat

Month	**Channel**	**QRad Tb Mode**	**WindSat Tb Mode**	**Tb Difference**
Before Normalization				
Aug (2005)	**V-Pol.**	179	167.8	11.2
	H-Pol.	103	95.5	7.5
Feb (2006)	**V-Pol.**	178	165.3	12.7
	H-Pol.	104	94.5	9.5
After Normalization				
Aug (2005)	**V-Pol.**	179	181.9	-2.9
	H-Pol.	103	106	-3
Feb (2006)	**V-Pol.**	178	178.8	-0.8
	H-Pol.	104	107.5	-3.5

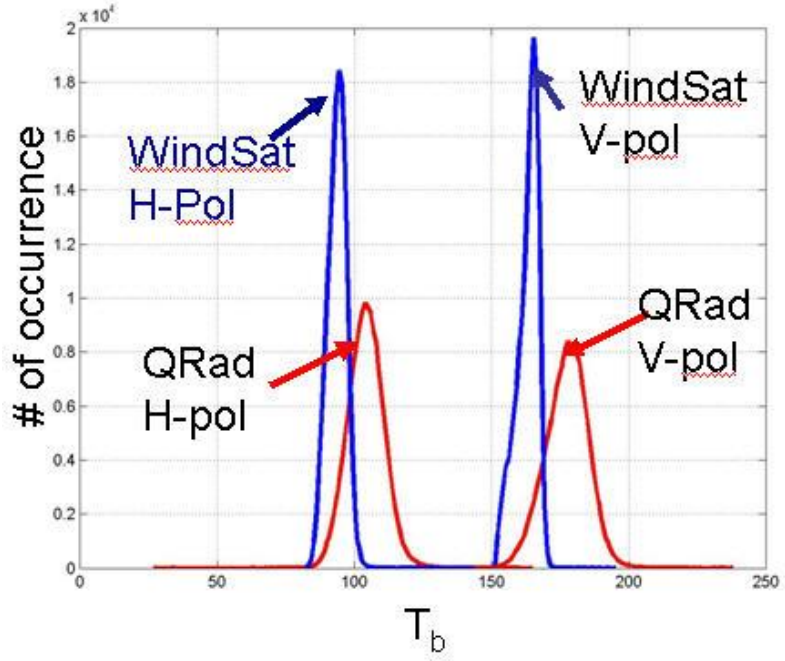

Fig. 4-1a: Histogram of 1° box average brightness temperatures for QRad and WindSat (before the normalization) for August 2005.

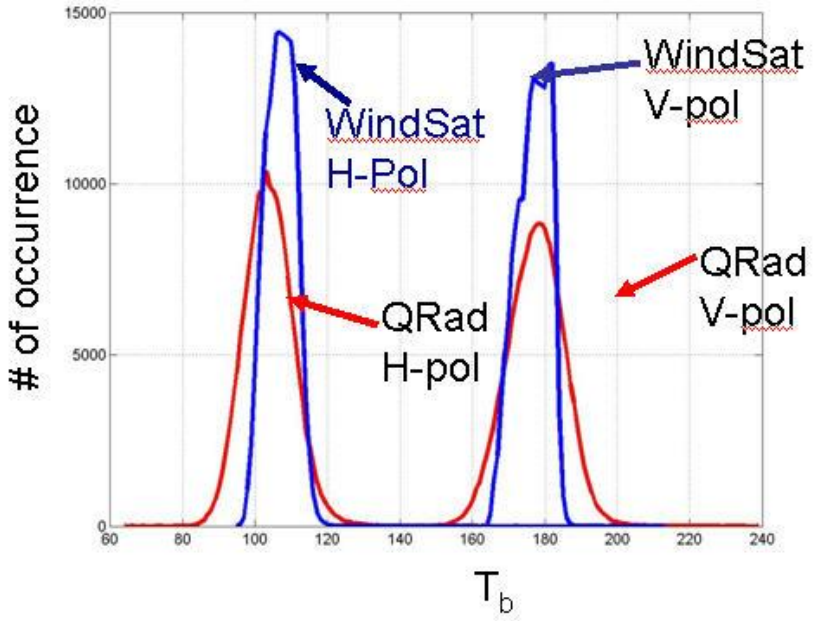

Fig. 4-1b Histogram of 1° box average brightness temperatures for QRad and WindSat (after the normalization) for August 2005.

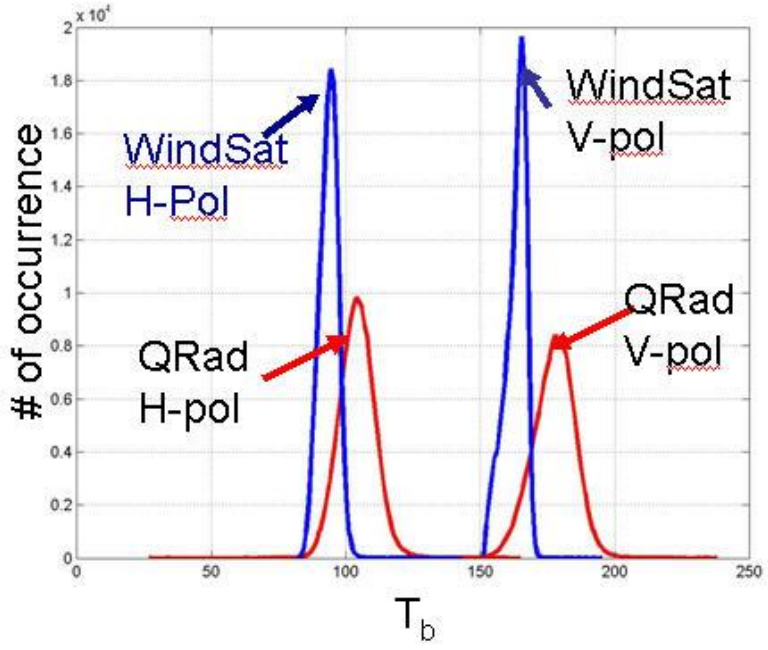

Fig. 4-2a: Histogram of 1° box average brightness temperatures for QRad and WindSat (before the normalization) for February 2006.

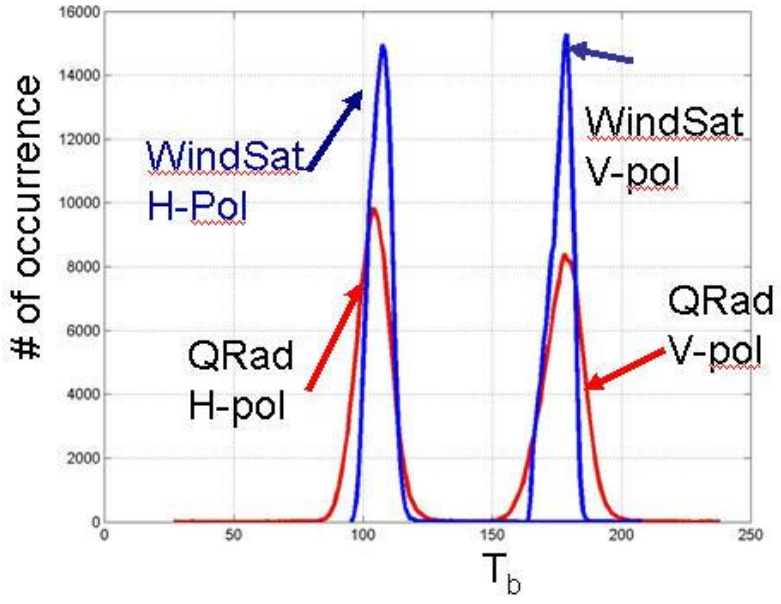

Fig. 4-2b: Histogram of 1° box average brightness temperatures for QRad and WindSat (after the normalization) for February 2006.

4.1.1 Orbital Pattern of QRad Radiometric Biases

In this section we determine the radiometric bias (H and V-pol) between the brightness temperature of QRad and the collocated WindSat's (normalized) observation in 1° boxes. Since QRad has high STD as shown in Fig. 4-1 and 4-2, it is necessary to average many 1° boxes to reduce the standard deviation of the estimated mean value. To preserve the bias changes that may be time variable (corresponding to latitude dependent), it is important that the averaging be according to different orbits (revolutions), which have different longitudes for the same corresponding relative orbit times (latitudes). Such an average over longitude is known as a "zonal" average.

To prepare the QRad data for inter-comparison with WindSat, monthly accumulations of 1° box match-ups were formed, along with the associated GDAS environmental parameters, and the biases were calculated for each box. Afterwards, zonal averages were performed over 360˚ in longitude using 1° latitude bins to form a latitude (relative orbit time) series, which preserved the once per orbit pattern of QRad's Tb, WindSat's Tb, and the QRad biases. Two monthly datasets separated by 6 months (August and February) are presented in Figs. 4-3 and 4-4. The x-axis represents match-ups over the ice-free oceans from 50° latitude-south to 50° north; and in these figures, the ascending and the descending portions of the orbits are combined.

The results show that the QRad and WindSat (normalized) "average orbit" brightness temperatures generally track with latitude with is a small systematic difference that is less than a few Kelvin. Further, there is similarity in pattern of QRad's T_b for both H and V-

pol that infers that the systematic differences are “common-mode” to both polarizations. The Tb variation within one orbit is due to the change of the environmental parameters with latitude (e.g. sea surface temperature (SST) and atmospheric water vapor (WV)), which are maximum near the equator (0˚ lat) and decrease toward the North and South poles). The orbital pattern of QRad T_b is consistent for different months (August and February) and exhibits seasonal changes whereby the peak of the curve moves from slightly above the equator in August to slightly below the equator in February, which corresponds to the expected seasonal change in WV over the inter-tropical convergence zone (ITCZ).

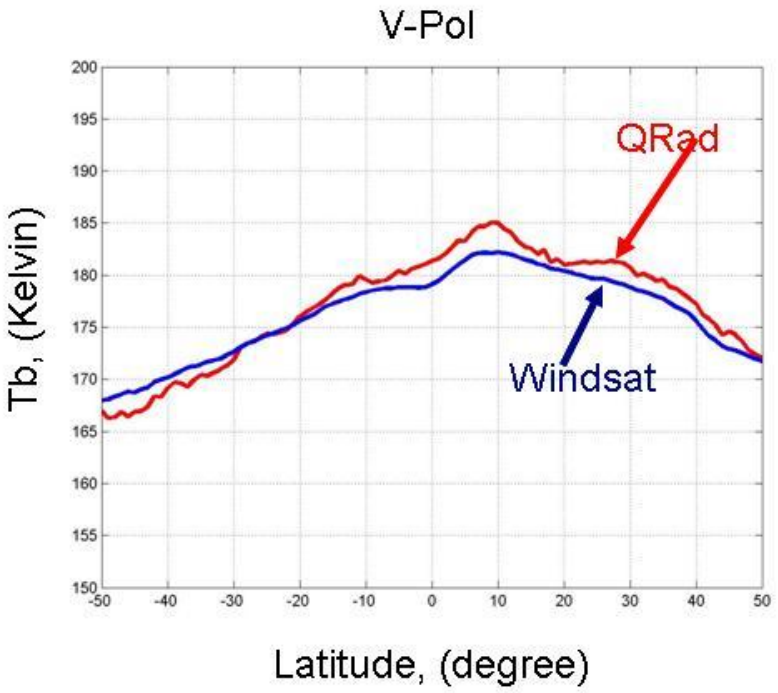

Fig. 4-3a: QRad/WindSat T_b comparison for August 2005 (V -Pol).

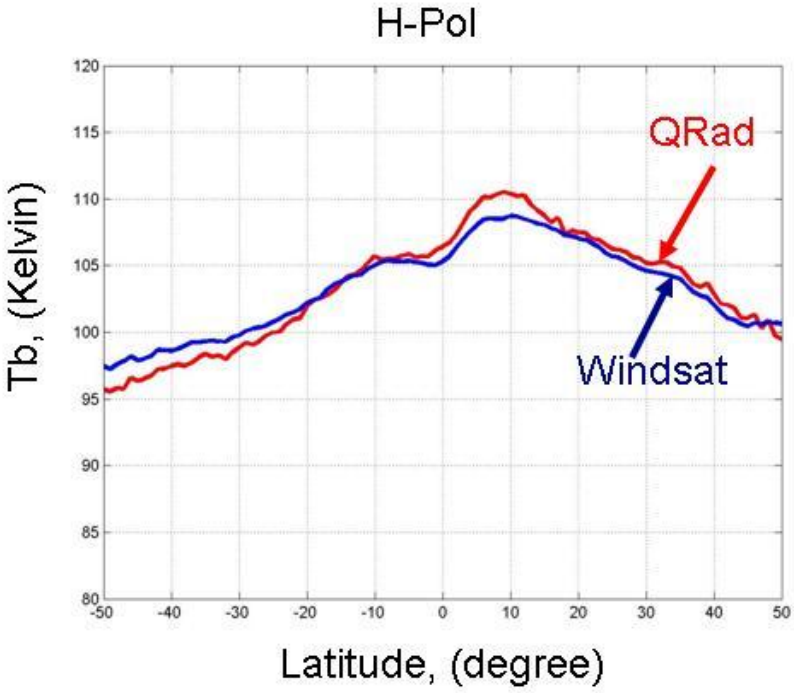

Fig. 4-3b: QRad/WindSat T_b comparison for August 2005 (H -Pol).

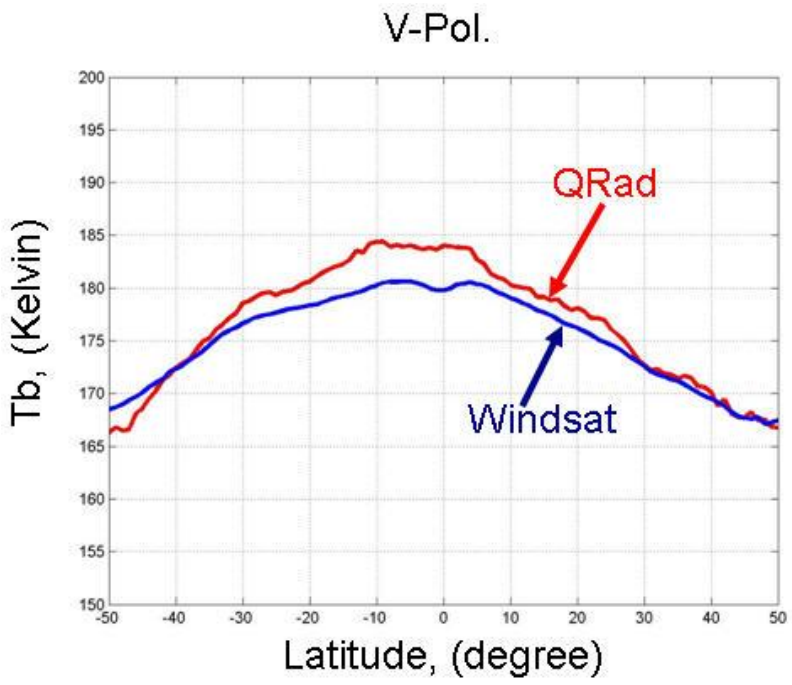

Fig. 4-4a: QRad/WindSat T_b comparison for February 2006 (V-Pol).

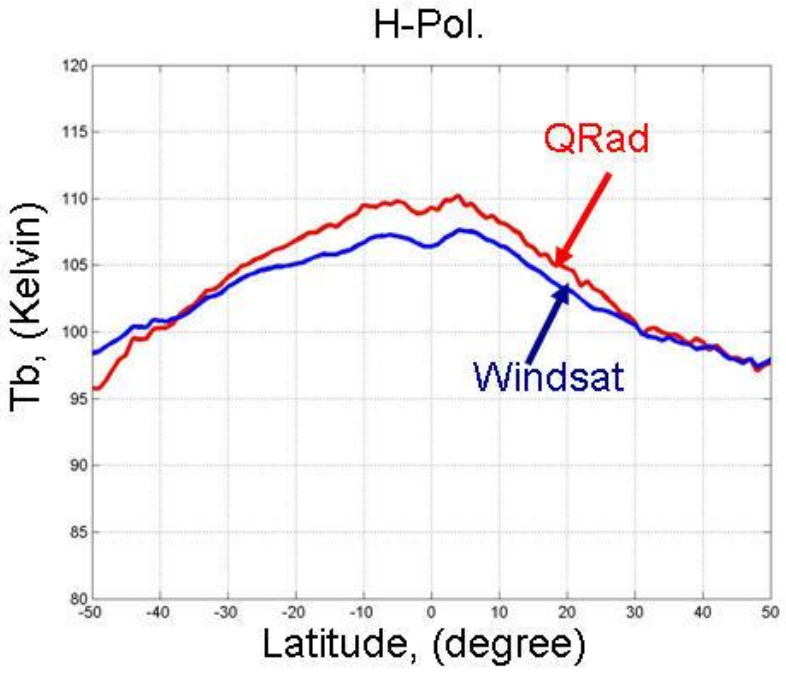

Fig. 4-4b: QRad/WindSat T_b comparison for February 2006 (H -Pol).

To investigate the cause for this systematic Tb difference between QRad and WindSat, the radiometric bias was examined separately for ascending (asc) and descending (dec) portions of the orbit. Again, zonal averages were performed, but now using 5° latitude bins (to compensate for the reduced number of samples) to form a latitude series, which preserved the once per orbit pattern of radiometric biases. Results presented in Figs. 4-5 and 4-6 indicate that the QRad's brightness temperatures were colder than the WindSat's brightness temperatures in the southern hemisphere by ~2K and warmer in the northern hemisphere by ~2-3 K for both H- and V-pol. Further, these results show that the ascending and descending portions track each other with latitude, and the difference is generally within ± 1 K.

This is a very favorable result in that the biases are nearly identical with relative orbit time (latitude) and stable during the continuous sunlit orbits for both winter and summer. This supports the notion that the bias is a common-mode effect within the QRad Tb algorithm and eliminates the possibility that the cause is related to ascending and descending effects, which are manifested in a local time of day phenomenon for the ocean Tb's.

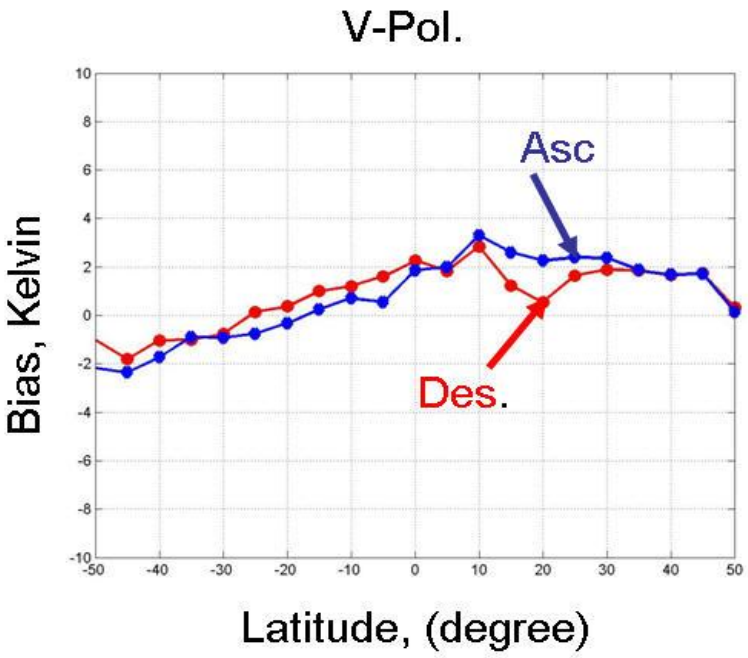

Fig. 4-5a: QRad T_b bias for August 2005 (V -Pol).

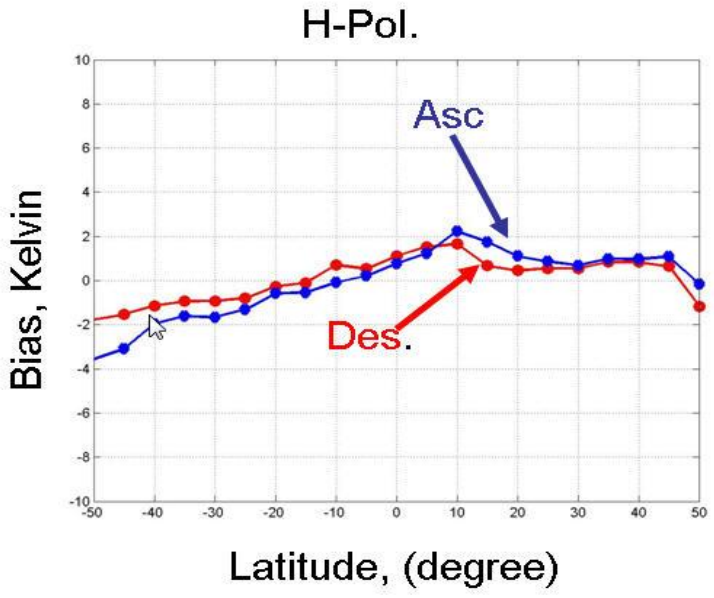

Fig. 4-5b: QRad T_b bias for August 2005 (H -Pol).

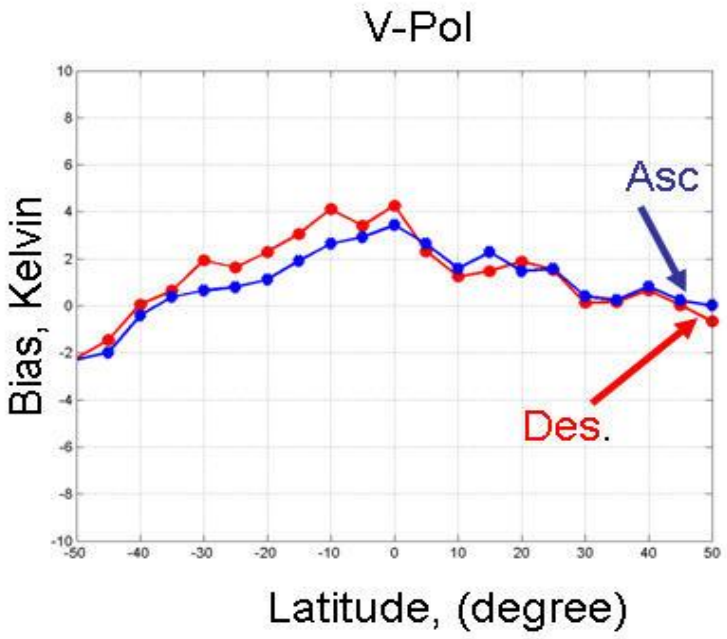

Fig. 4-6a: QRad Tb bias for February 2006 (V -Pol).

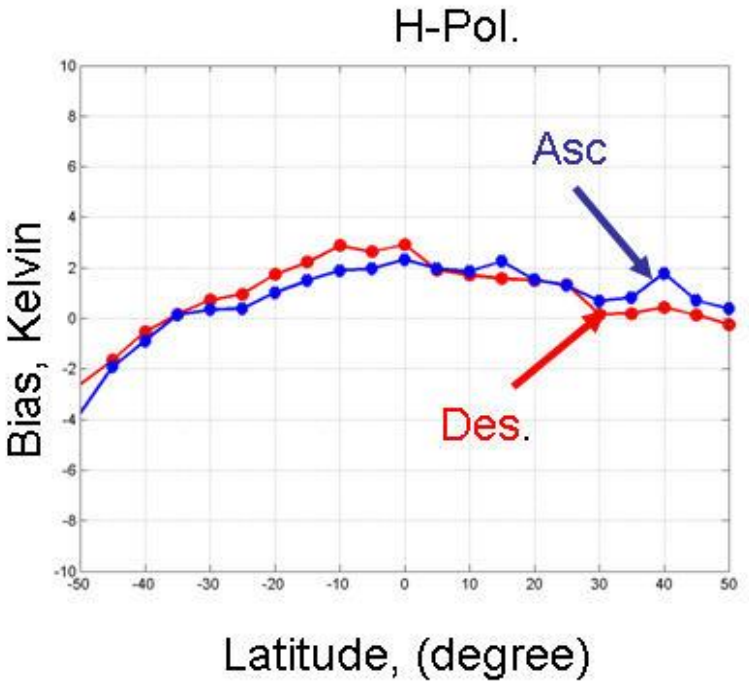

Fig. 4-6b: QRad Tb bias for February 2006 (H -Pol).

To examine the consistency of the QRad biases, the analysis (QRad/WindSat comparison) was repeated for the 9 month period (February through October) during continuous sunlit orbits. The results shows that the QRad biases are very stable during the sunlit orbits, these results were illustrated in Figs. 4.7 – 4.15.

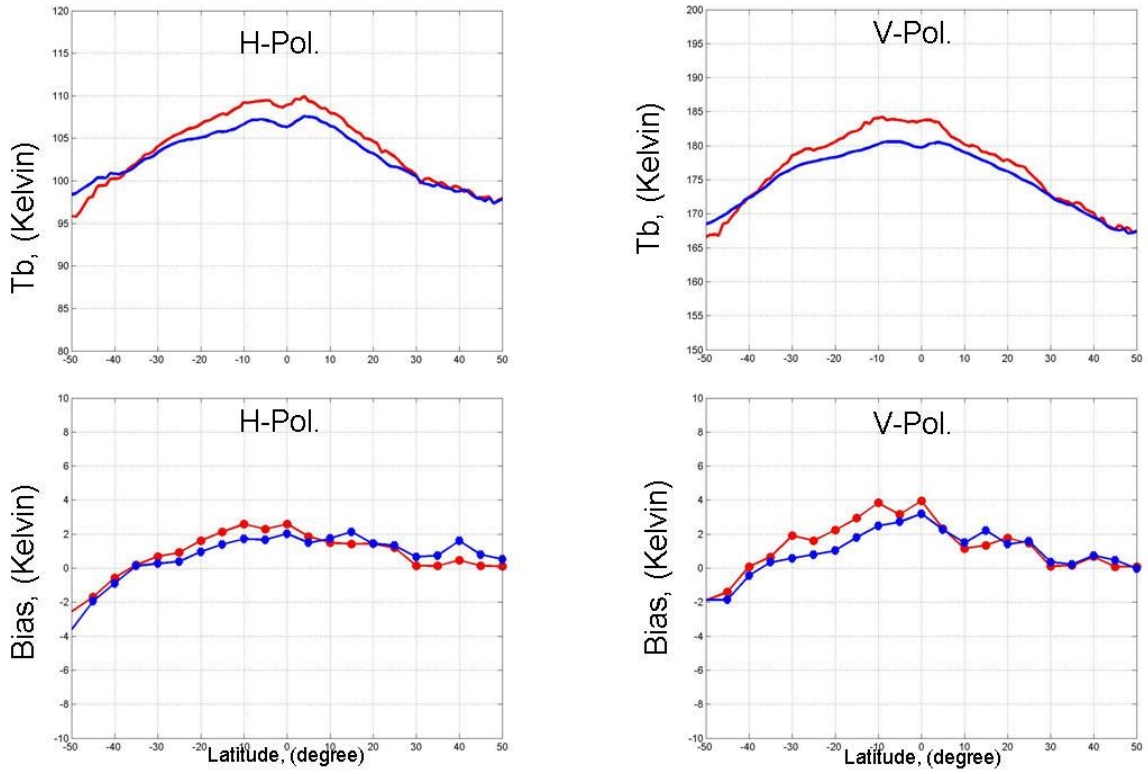

Fig. 4-7: Ocean brightness temperature comparisons in 1° boxes between QRad and WindSat (normalized) for February2006.

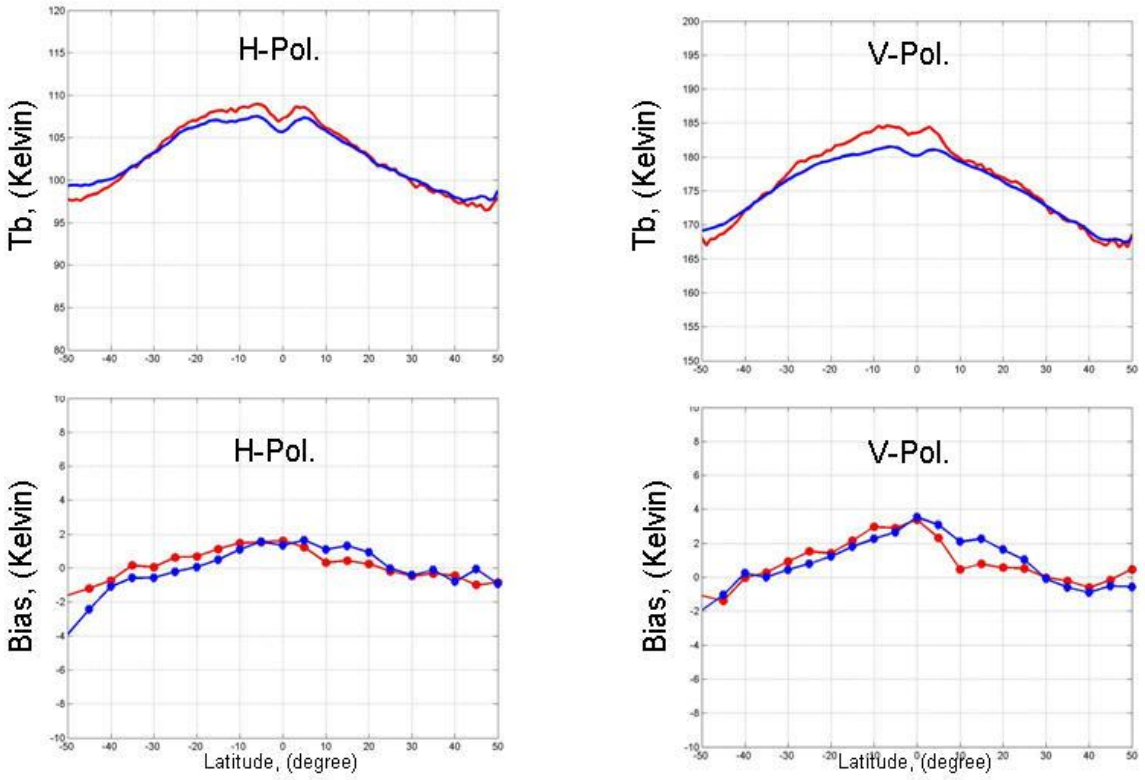

Fig. 4-8: Ocean brightness temperature comparisons in 1° boxes between QRad and WindSat (normalized) for March 2006.

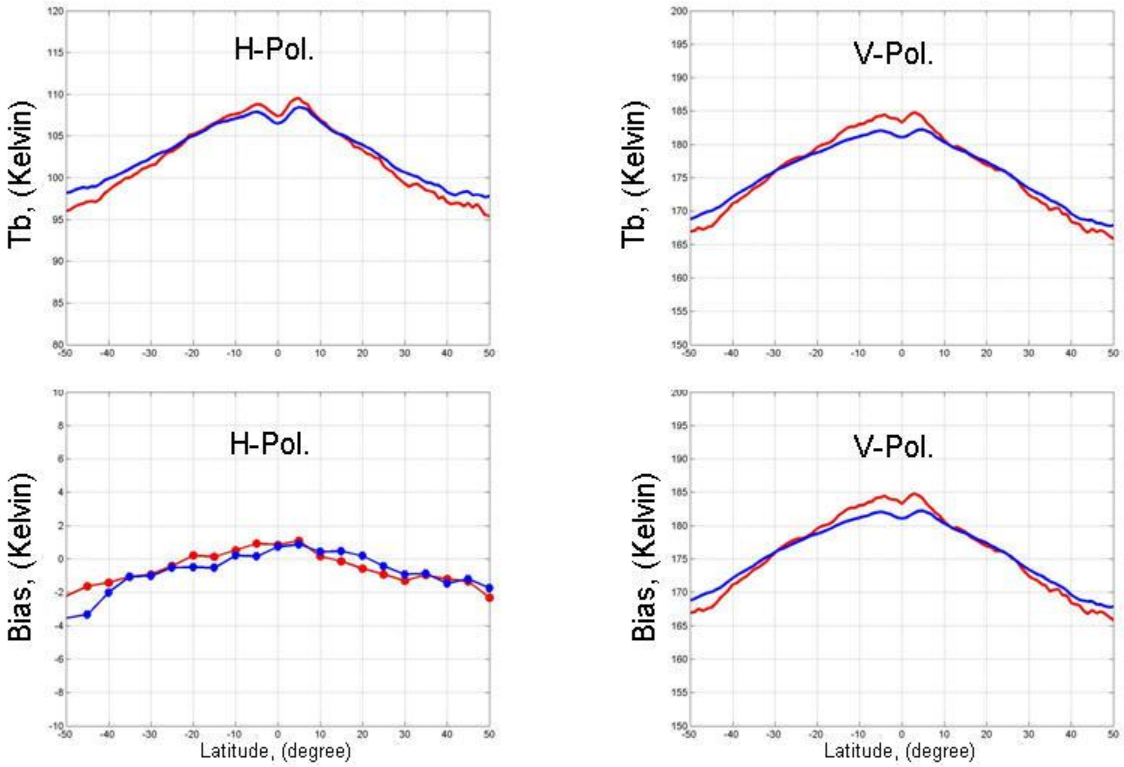

Fig. 4-9: Ocean brightness temperature comparisons in 1° boxes between QRad and WindSat (normalized) for April 2006.

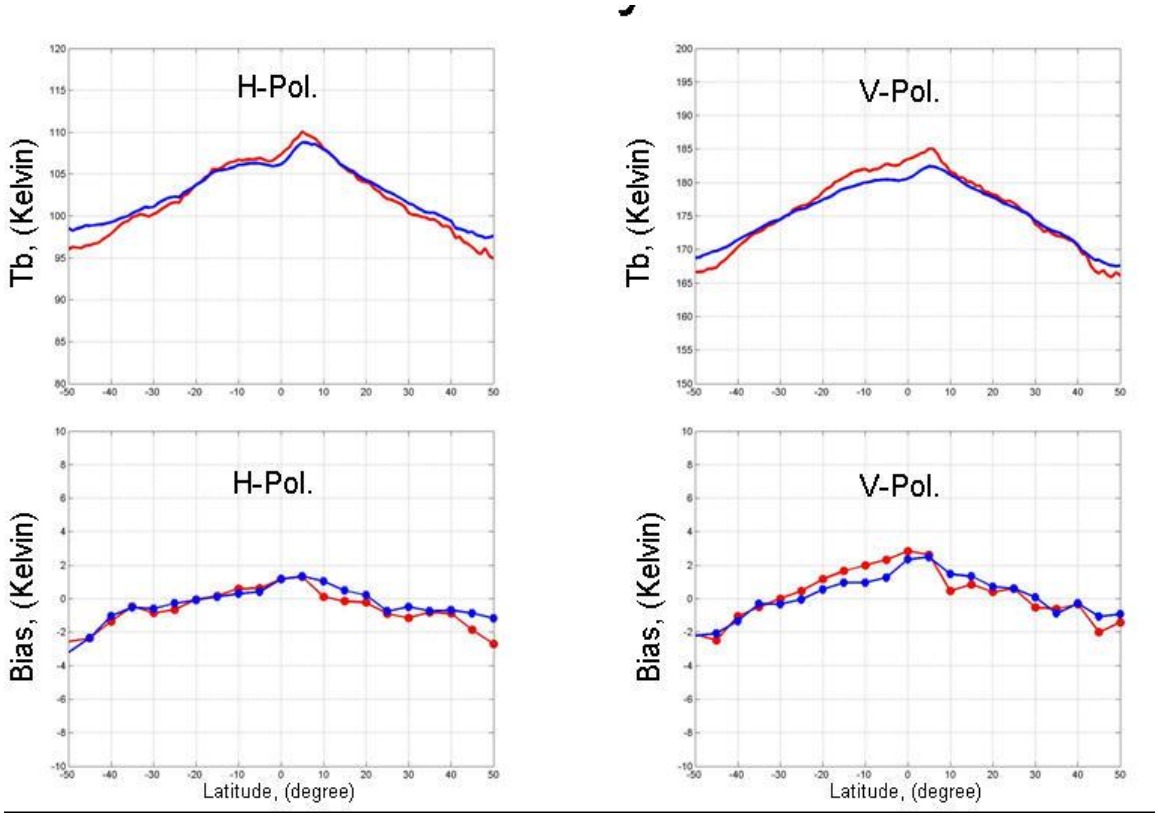

Fig. 4-10: Ocean brightness temperature comparisons in 1° boxes between QRad and WindSat (normalized) for May 2006.

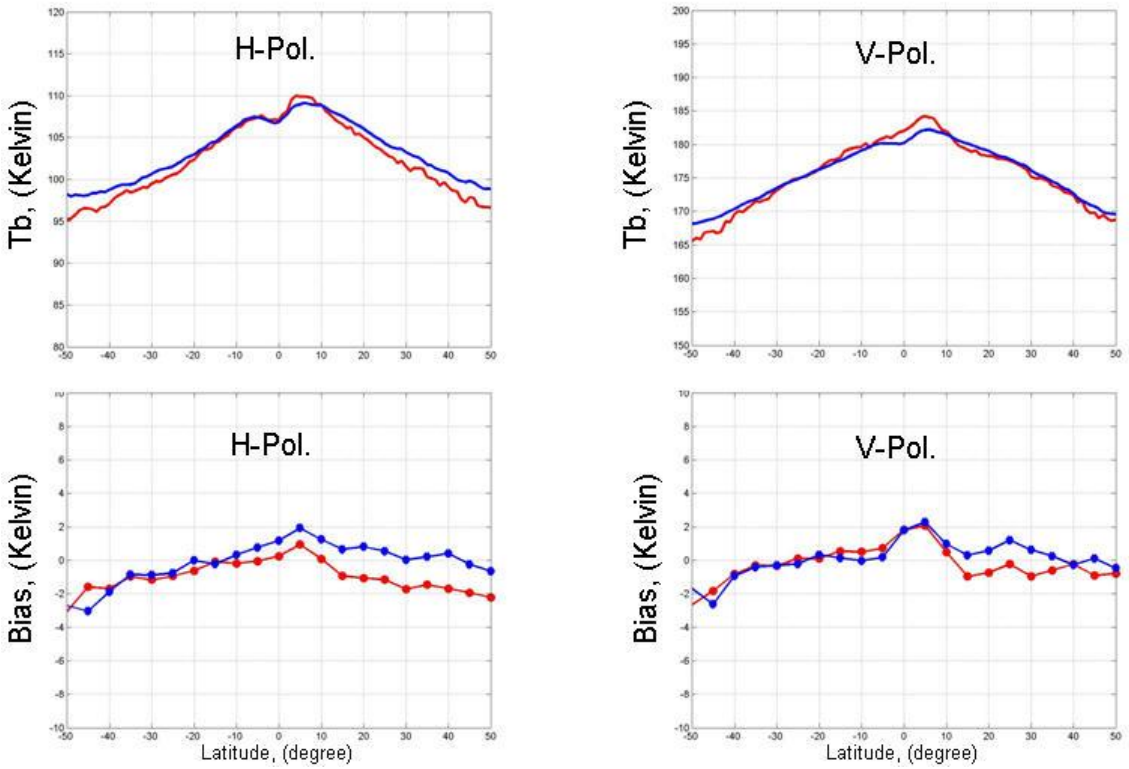

Fig. 4-11: Ocean brightness temperature comparisons in 1° boxes between QRad and WindSat (normalized) for June 2006.

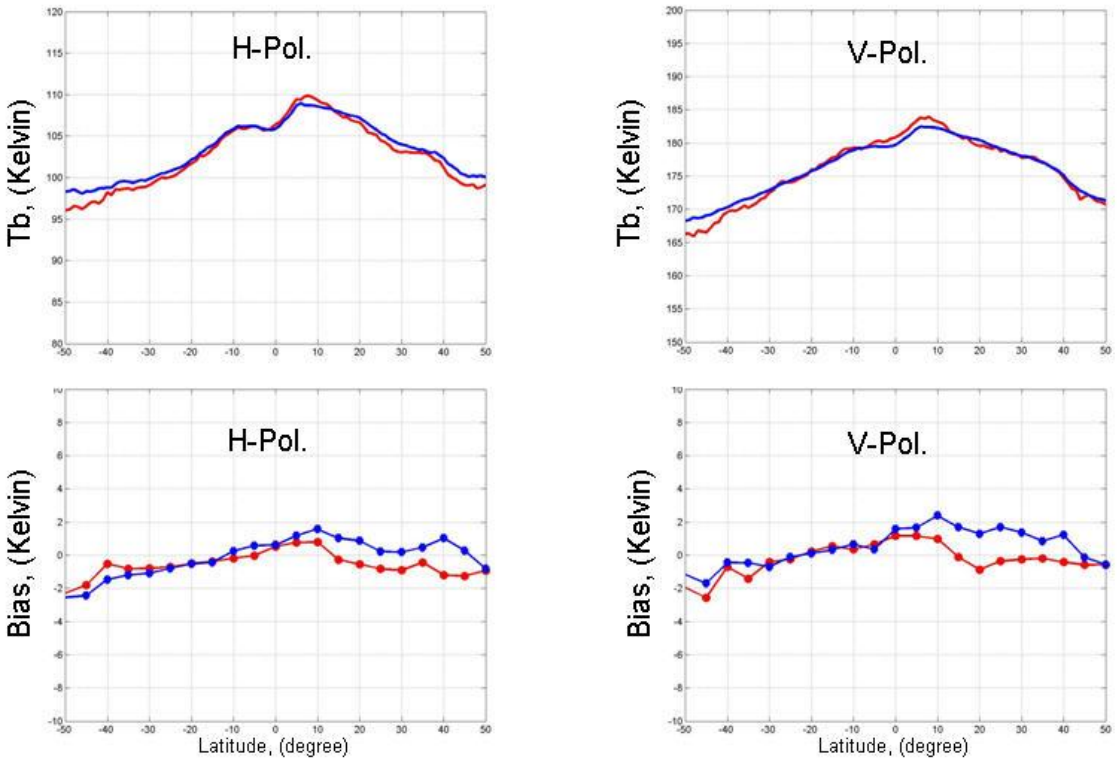

Fig. 4-12: Ocean brightness temperature comparisons in 1° boxes between QRad and WindSat (normalized) for July 2005.

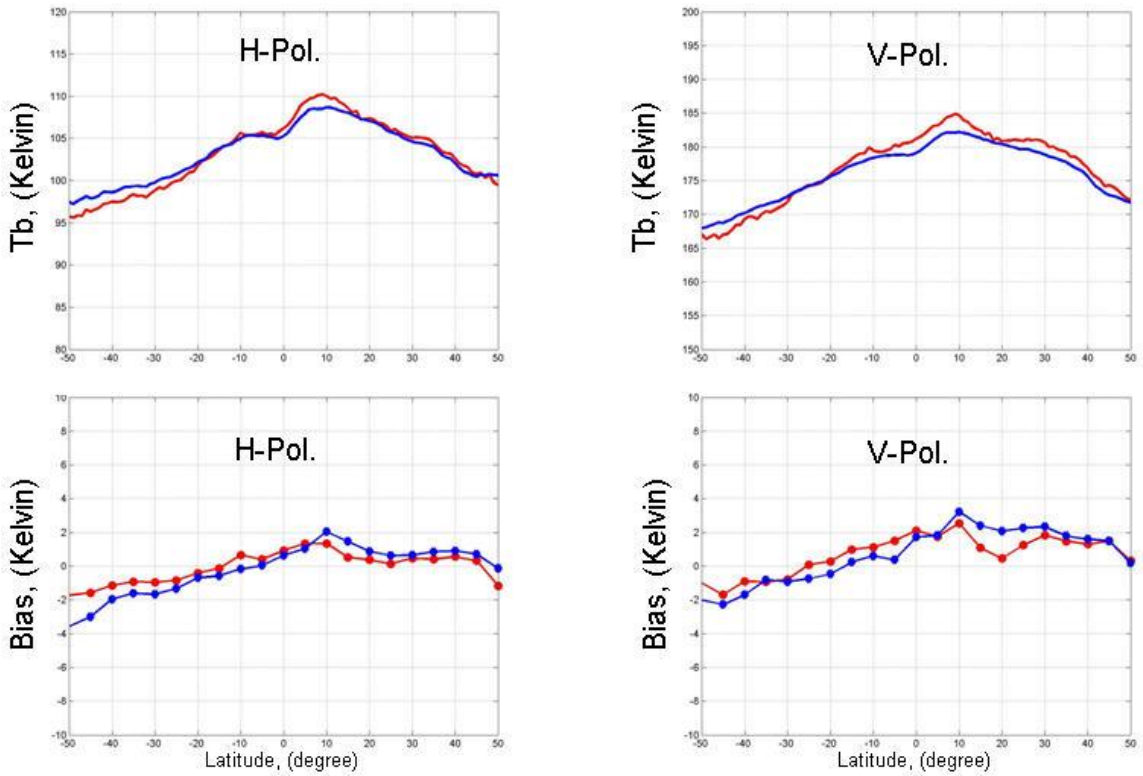

Fig. 4-13: Ocean brightness temperature comparisons in 1° boxes between QRad and WindSat (normalized) for August 2005.

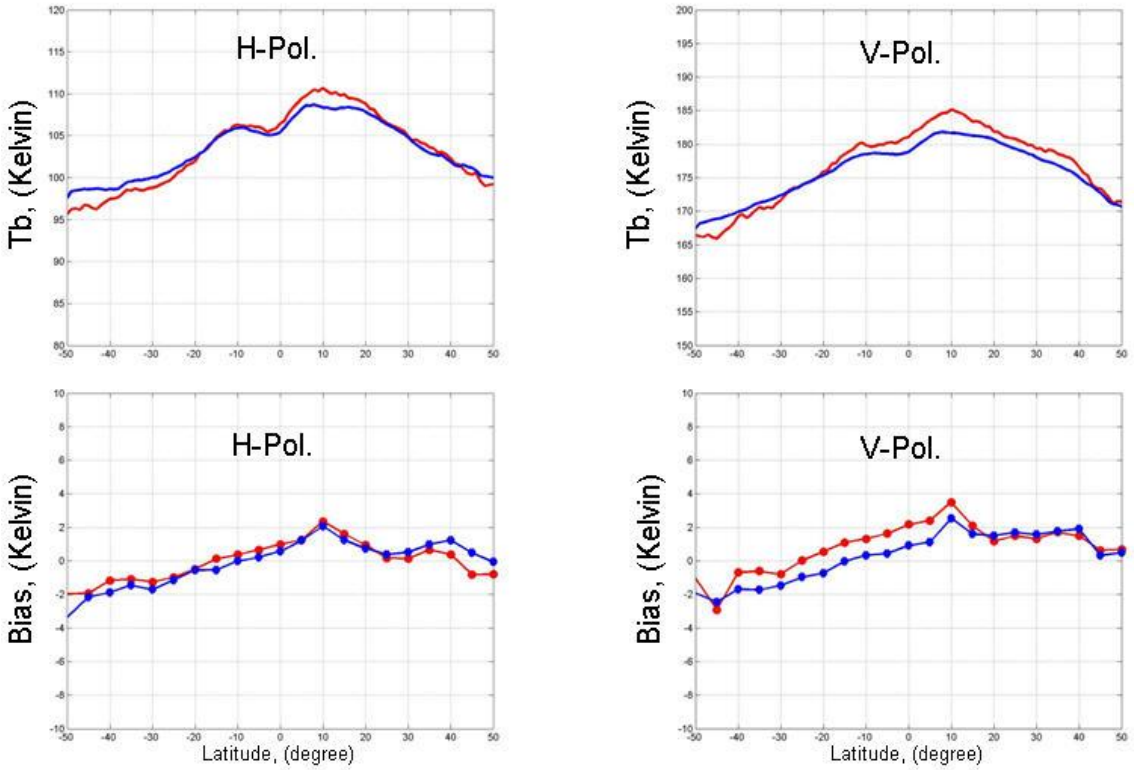

Fig. 4-14: Ocean brightness temperature comparisons in 1° boxes between QRad and WindSat (normalized) for September 2005.

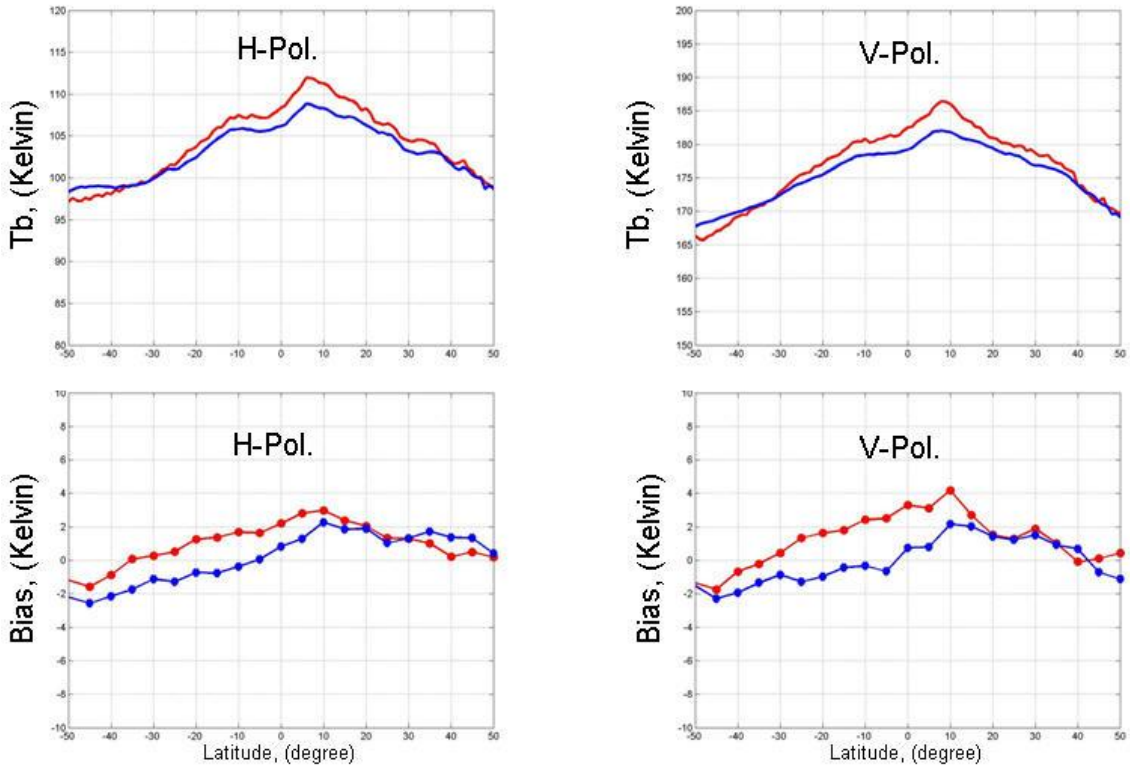

Fig. 4-15: Ocean brightness temperature comparisons in 1° boxes between QRad and WindSat (normalized) for October 2005.

Results from the QRad's biases (QRad-WindSat_normalized) latitude series (Zonal average over 360 degree longitude), presented in Fig. 4-16, shows biases of less than ± 4 K for the entire nine month sunlit period (February through October) for both H- and V-Pol.. Further since these results 6 exhibit systematic errors, there is room for improvement in future work.

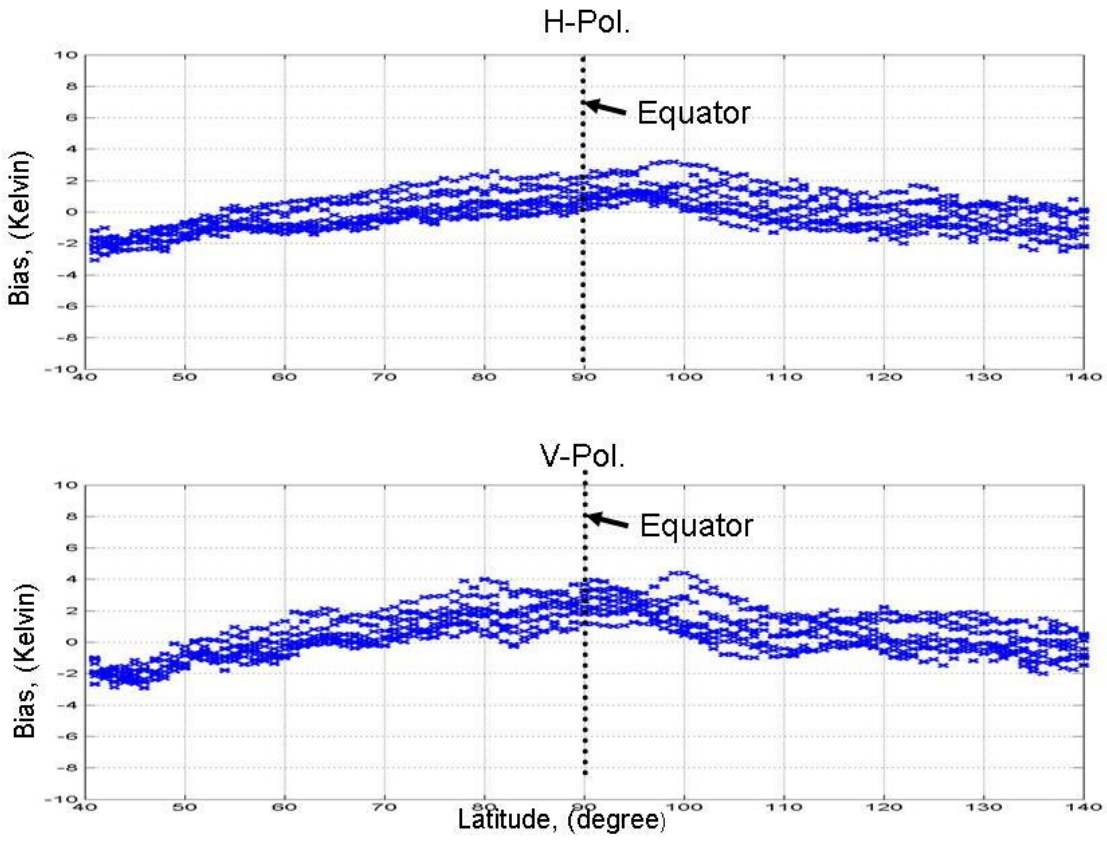

Fig. 4-16: Ocean brightness temperature biases for nine months during Sunlight between QRad and WindSat (normalized) for 2006.

And table 4-2 shows the mean values for QRad's biases on monthly basis, the results shows biases of less than ±1 K for the entire nine month sunlit period (February through October) for both H- and V- Pol.

Table 4-2: Mean/ STD Value of QRad's Brightness Temperatures Biases for nine month

Month	V-pol	H-pol
February	0.98 /1.75	0.53 /1.67
March	0.49/1.61	-0.12/1.23
April	-0.28/1.5	-0.67/1.23
May	-0.06/1.64	-0.57/1.36
June	-0.13/2.72	-0.93/1.31
July	-0.22/1.88	-0.30/1.59
August	0.43/2.04	0.15/1.33
September	0.681.69	0.03/1.25
October	0.91/2.29	0.9/2.05

4.2 Dynamic QRad Biases during Eclipse

Each year from November 14th through January 30th, QuikSCAT experiences a short solar eclipse on every orbit. During these periods, the SeaWinds instrument undergoes a significant physical temperature cooling transient (from sunlight to night). The purpose of this section is to evaluate the QRad radiometric bias during this eclipse period to assess the ability of the QRad transfer function to maintain a stable radiometric calibration.

For this purpose, we repeated the QRad/WindSat radiometric inter-calibration during eclipse periods. Our concern is that the radiometric calibration effects could depend upon duration of the eclipse, which is variable over this 2.5 month period (as illustrated in Fig. 4-17a). Therefore, it is important that this be taken into account in the analysis. During this period, the latitude at which the satellite passes into the earth shadow (night) moves southward each day until the December 21st at which time it reaches 60° North, and the maximum eclipse duration of ~ 16 minutes occurs. This is illustrated in Fig. 4-17b, where the satellite ground tracks are shown for 7 orbits (revs). Note that the sunlit portion of the orbit is shown in yellow and the night portion is shown in dark blue. During each ascending rev, the satellite enters into the eclipse; and during each descending rev, it exits the eclipse. Thus, the pre- and post-eclipse periods can be equated to ascending and descending portions of the orbit below 60° North. After December 21st, the eclipse boundary retreats northward until it vanishes on January 30th.

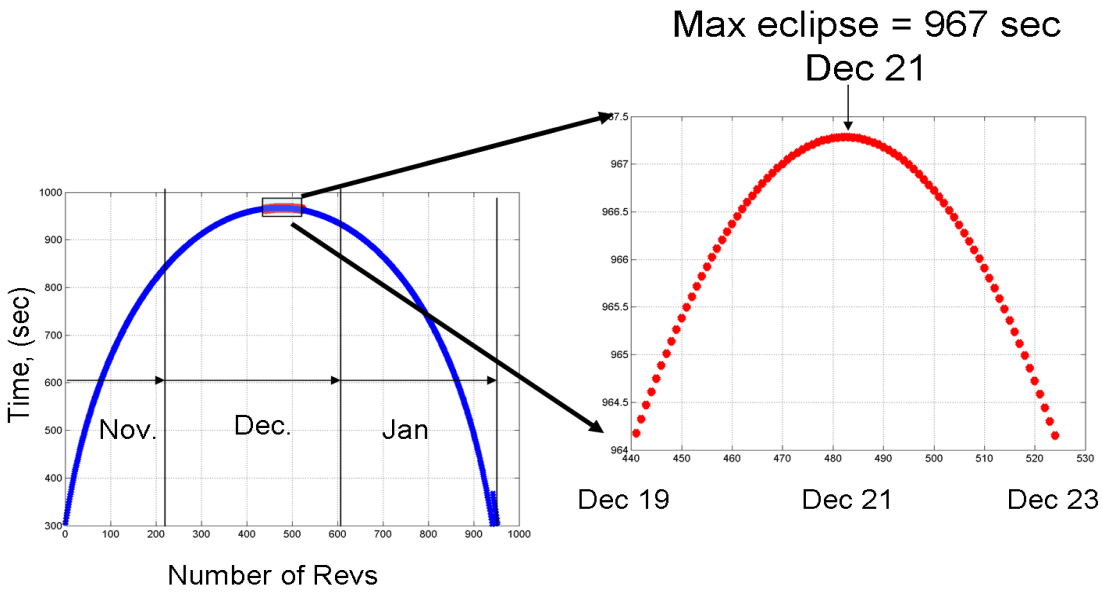

Fig. 4-17a: QuikSCAT orbit eclipse duration between mid-November and the end of January.

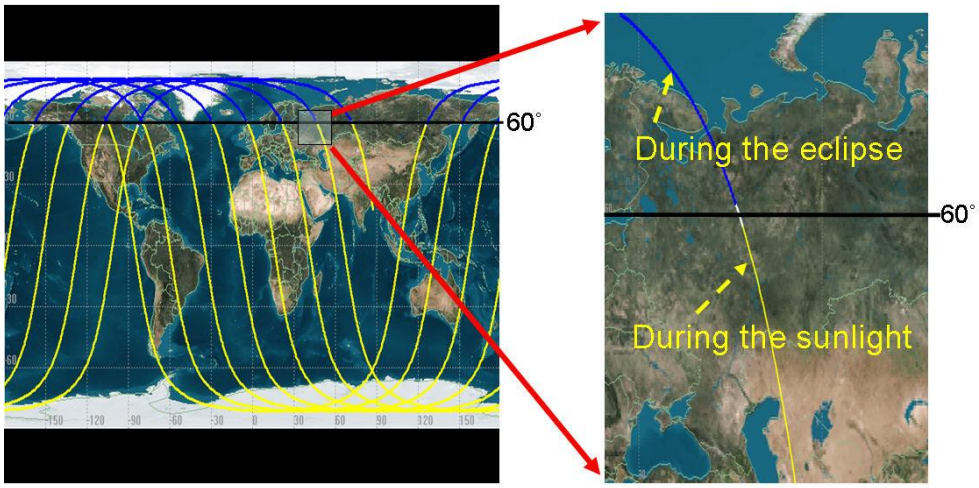

Fig. 4-17b: Orbital eclipses for QRad on December 21, 2005 for 7-revolutions. (courtesy Satellite Tool Kit www.stk.com).

To assess the dynamic (time-variable) bias of the QRad during the eclipse period, zonal averages were again performed over full 360˚ longitude but separated by ascending and descending portions of the orbit. Since eclipse occurs only at 60˚ latitude or higher, there are only a few 1° box match-ups that occur over ocean; therefore, we used 5° latitude bins (to have sufficient boxes to reduce the standard deviation). The initial evaluation created a latitude series, which was averaged for the month of January, and results are presented in Fig. 4-18. Note that the corresponding T_b_biases for ascending (pre-eclipse) and descending (post-eclipse) orbit segments at 50° N latitude differ by -6K for V-pol and -8 K for H-pol. After exiting eclipse, the biases on the descending portion of the orbit gradually approach the ascending bias values. The biases converge at the equator and remain approximately equal in the southern hemisphere, which is similar to the previous results during the continuous sunlight conditions for February (Figs. 4-5) and August (4-6).

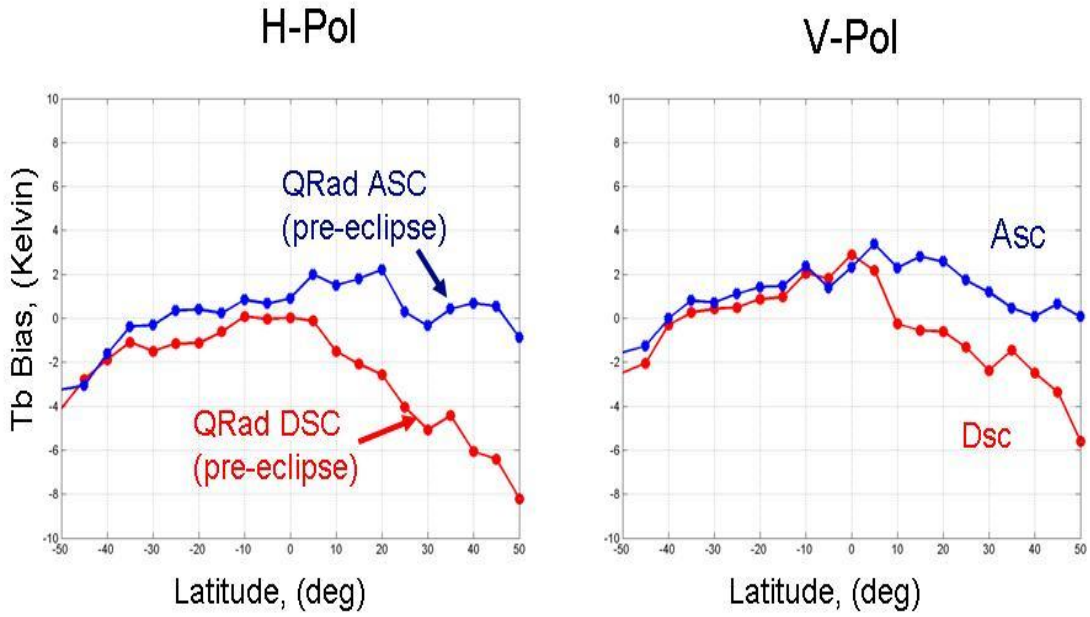

Fig. 4-18: Monthly average QRad T_b bias (during eclipse period) for January 2006 with ascending revs shown as “circle” and descending revs as “diamond”.

We believe that the failure of QRad to maintain radiometric calibration during eclipse is because the physical temperature of the antenna front-end losses is not modeled correctly. Unfortunately, the temperature of the reflector and feed are not measured on-orbit; and in the QRad transfer function, the physical temperature for the front-end loss is assumed to be equal to the rotary-joint temperature measurement, which is the closest temperature sensor. However, the rotary-joint resides in a thermal-controlled environment; thus, the large transient physical temperature swings of the feed horns and platform waveguide are most likely underestimated during the solar eclipses.

Since monthly averages for January included a wide range of eclipse times (900 sec to 300 sec), we repeated the analysis for five days (December 19 – 23, 2005), where the duration was approximately constant. For these days, the eclipse duration of 964 - 967 seconds (~16 minutes) was the maximum, and the day/night terminator was fixed at ~ 60° N.

To understand this transient effect, we examined the dynamic bias as a function of time. Results presented in Fig. 4-19 illustrate the average (5-day) orbital pattern of the QRad bias displayed versus relative orbit time (from the start of the orbit at the South Pole). Note that the satellite enters into eclipse at about 53 minutes, then there is a monotonic increase in the bias (more negative by 12 K) until the satellite re-enters sunlight, which is ~16 minutes later. Afterwards, the bias decreases (becomes less negative) at approximately the same rate until it reached an equilibrium at about 86 minutes. This time-variable orbital bias pattern agrees with our expectation of the reflector physical

temperature, which cools during the dark portion of the orbit and warms when it is exposed to the sunlight.

Further, we note that a similar result was found during the recent inter-satellite radiometric calibration between the Tropical Rainfall Measurement Mission (TRMM) Microwave Imager (TMI) and the WindSat as reported by Gopolan et al. [25]. This investigation uncovered a time-variable radiometric bias in the TMI brightness temperatures that was the result of a slightly emissive parabolic antenna main reflector with an on-orbit variable physical temperature that varied systematically around each orbit. Because of TRMM's non-sun synchronous orbit, this effect occurred on every orbit, which had both sunlit and night orbit segments.

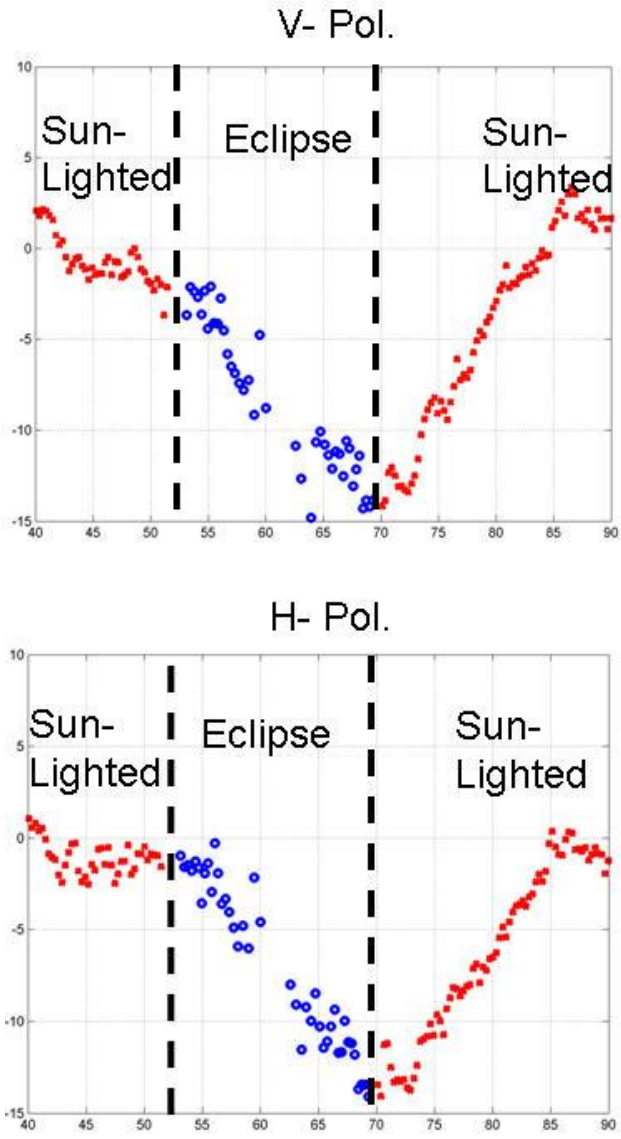

Fig. 4-19: QRad T_b bias (during max eclipse period) December 19 - 23 for V & H-pol., where x-axis represents relative orbit time (from the start of the orbit at the South Pole) in minutes and y-axis QRad bias in Kelvin.

4.3 QRad Transfer Function Analyses

4.3.1 QRad transfer function analysis during eclipse

As discussed above, the QRad brightness temperature algorithm as implemented in the JPL L2A processing system fails to maintain the expected radiometric calibration during the eclipse period from mid-November until the end of January. Because the physical temperature of the front-end losses is not measured on-orbit, a hypothesis was developed that the front-end temperature transient is not adequately modeled in QRad Tb algorithm (radiometric transfer function), which is evident through comparisons inter-satellite Tb comparisons between QRad and WindSat.

As described in chapter 2, there are 3 different losses that are combined as "front-end" losses (L1A & L1B) in the transfer function:

4. L1, the feed assembly losses (including feed and graphite waveguide)
5. L2, the microwave rotary joint loss
6. L3, the platform waveguide losses between the SeaWinds Antenna Subsystem and the SeaWinds Electronic Subsystem

where: L1A (L1B) include the total loss of L1, L2, and L3, and subscripts A and B refer to the inner and outer beam respectively

For the V-pol,

L1A = -1.12 dB,

L3 = -0.24 dB

and the microwave rotary joint loss (L2) is

L2= -0.18 dB.

Therefore, the feed assembly loss (L1) is

L1= - 0.59 dB or a power ratio = 0.863

For the H-pol,

L1B = -1.05 dB,

L3 = -0.21 dB

and the microwave rotary joint loss (L2) is

L2= -0.18 dB.

Therefore, the feed assembly loss (L1) is

L1= - 0.64 dB or a power ratio = 0.863

The radiometric Tb bias introduced by this front-end loss is

$Tb_{\_bias} = T_{phy} * (1 - \text{loss ratio});$

and the change in this bias during eclipse can be expressed as:

$(\Delta Tb_{\_bias}) = (\Delta T_{phy}) \times (1- \text{loss ratio})$

During the SeaWinds Antenna Subsystem Critical Design Review, results from a thermal analysis performed by JPL thermal engineering [27] are shown in Fig. 4-20. This analysis, using a thermal model for the SeaWinds antenna, calculated the physical temperatures for the reflector, feed horn and the connecting antenna waveguides during the eclipse transition.

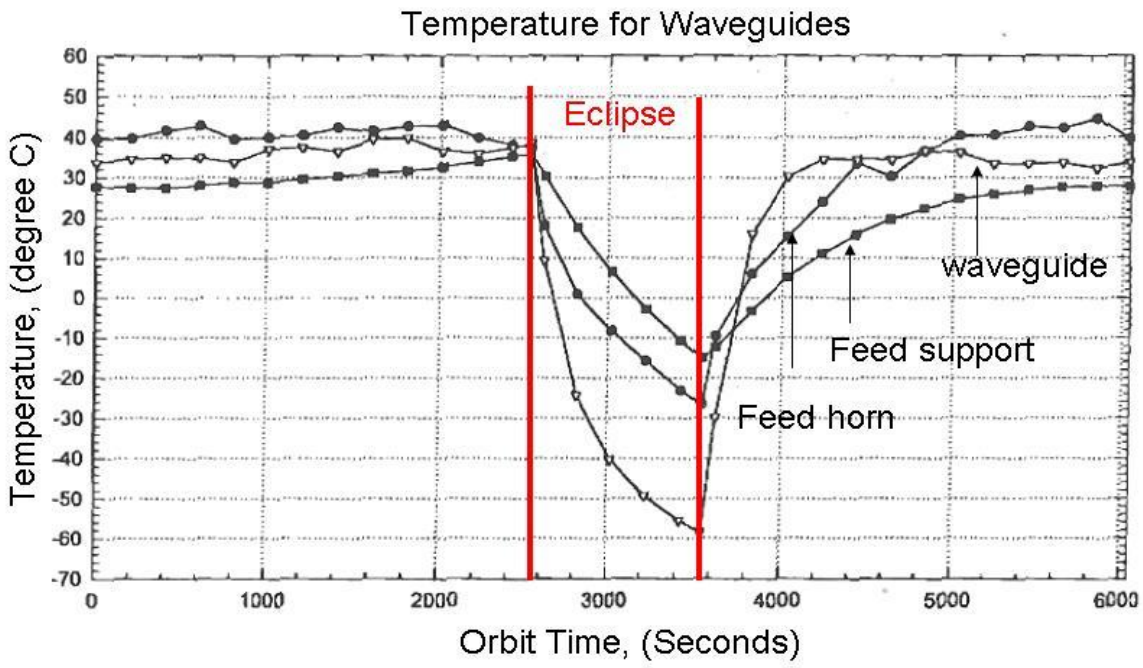

Fig. 4-20: Transient physical temperature for the SeaWinds antenna reflector, feed horn, and waveguides during the eclipse period, from pre-launch thermal analysis [27].

Since the antenna waveguides, horn and reflector, were made of composite (graphite) material which exhibited high radiative (infrared) emission and very low heat capacity, the analysis showed that there would be a wide range of physical temperature variations during eclipse. Also, because the fixed platform waveguides (following the rotary joint) were aluminum and were insulated by multi-layer blankets, their physical temperatures were predicted to be much less affected. The antenna waveguide physical temperature time history shows that under the sunlit conditions, the temperature should be stable; however during eclipse, the waveguide temperature should decrease by about 95˚ C. The other antenna elements (feed and feed support structure) are more massive and have increased thermal capacity; and as a result, their temperature swings during eclipse are less severe than the waveguide. Further, their time constants to reach thermal equilibrium

in the sunlight are longer than that associated with the antenna waveguide temperature transient.

The results observed for the QRad radiometric bias (Fig. 4-19) are more consistent with the feed waveguide time constants, which supports the hypothesis that the change of the front-end losses physical temperature is the cause for this error in the QRad Tb algorithm.

Based on the predicted change in the feed waveguide physical temperature given in Fig. 4-21, the variation of the physical temperature (ΔT_{phy}) for the feed assembly antenna loss is 95˚ C. This results in a calculated change in the waveguide brightness temperature of

For V-Pol.:

$$(\Delta Tb_{\_bias}) = (\Delta T_{phy}) \text{ x (loss ratio)}$$

$$(\Delta Tb_{\_bias}) = 95 * (1 - 0.863) = 13.01 \text{ K}$$

For H-Pol.:

$$(\Delta Tb_{\_bias}) = (\Delta T_{phy}) \text{ x (loss ratio)}$$

$$(\Delta Tb_{\_bias}) = 95 * (1 - 0.873) = 12.06 \text{ K}$$

during the eclipse, which compares well to the observed ~13 K and 12K biases (ΔT_{bias}) for V-and H-Pol respectively in Fig. 4-11.

4.3.2 QRad transfer function analysis during the sunlit orbit

As discussed in section 4.1, there is a small bias (less than 3 Kelvin) between QRad and collocated WindSat observations. As observed in Fig. 4-5 and 4-6, these biases show systematic latitude dependence for both V and H-pol. When we compare these plots for the months of August and February, there is a small overall seasonal variation. For example, the location of the peak positive bias is different in each month (i.e. -10˚ and +10˚ latitude for months February and August, respectively). The analysis performed to identify the cause for this bias will be discussed in this section.

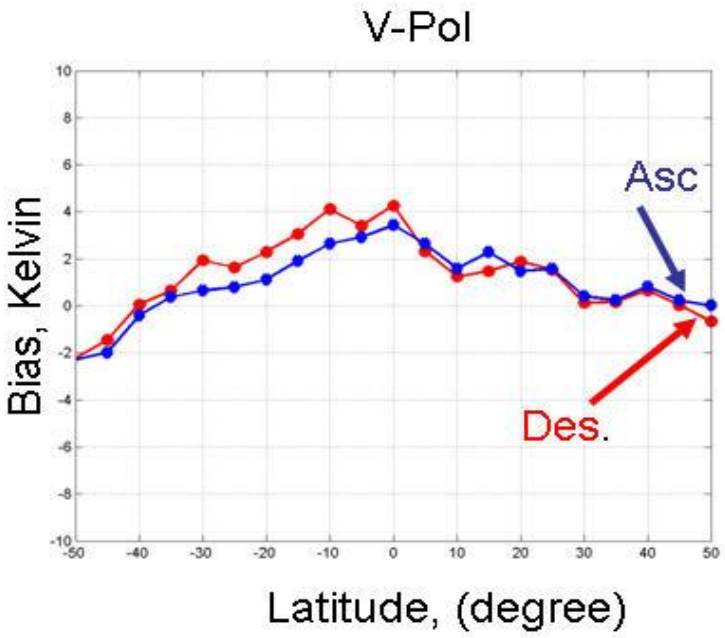

Fig. 4-6a: QRad Tb bias for February 2006 (V -Pol)

Since WindSat and QRad are in polar orbits, the change in latitude can be equated as delta time along the orbit. The instrument does not respond to changes in latitude or longitude, rather, it is the time change in the orbit. On the short scale, all changes are periodic in the orbit period (i.e. one cycle per orbit); therefore investigations were conducted to examine changes over the orbit period.

The first investigation was performed to check the variation for the receiver radiometric (noise) temperature (T_r) within one orbit. This is important because T_r is subtracted from the measured noise energy to produce T_b. The analysis was performed for two reasons:

1. To examine if there is any correlation between the patterns for T_r and QRad radiometric biases (colder in South pole and warmer in North pole).
2. To get the magnitude of the variation in T_r within one orbit,

The results show that there is no correlation between the patterns as illustrated in Figs. 4-21 and 4-22 and also the variation in Tr is less than one Kelvin (T_r ranges from 406.9 to 407.8 K).

Therefore, we can eliminate the possibility of causing the radiometric biases by the receiver radiometric temperature.

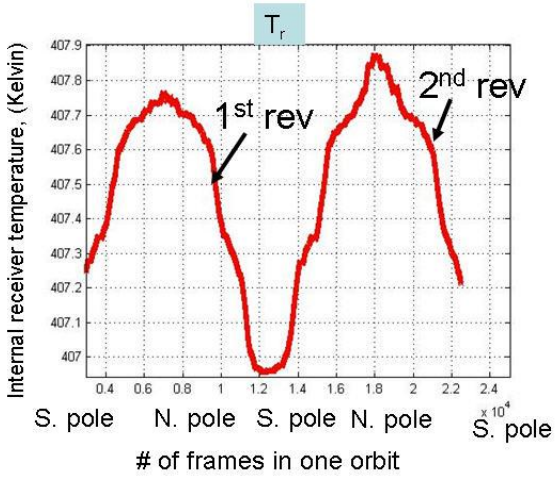

Fig. 4-21: The internal receiver temperatures for QRad

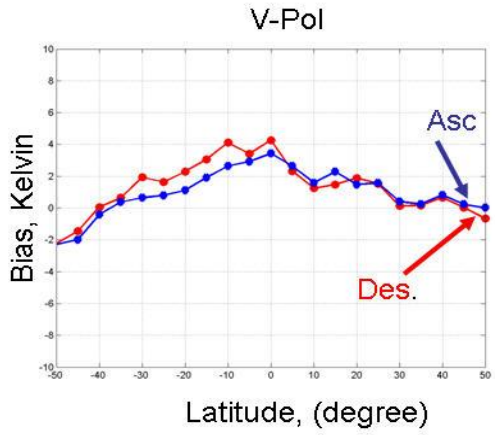

Fig. 4-22: QRad Tb bias for February 2006 (V -Pol)

The next investigation is to evaluate if the QRad radiometric bias is the result from the front-end losses on-orbit variable physical temperature, which varies systematically around each orbit.

$$\Delta T_{bias\_sun\_lighted} = \Delta T_{phy} \times (1- L1) \qquad (4\text{-}2)$$

Where L1 = 0.863 and $\Delta T_{bias\_sun\_lighted}$ = 4 K

Solving for ΔT_{phy} yields: ΔT_{phy} = 29.2 K, which is unrealistic to have such a high temperature swing in an orbit as SeaWinds in continuous sunlight.

The temperature data (Fig. 4-23) from the internal temperatures sensors in the Seawinds Electronics Subsystem are very stable also suggests that the external physical temperature does not vary this much (sun-synchronous).

The cause for the latitude dependence of this bias remains unexplained so far.

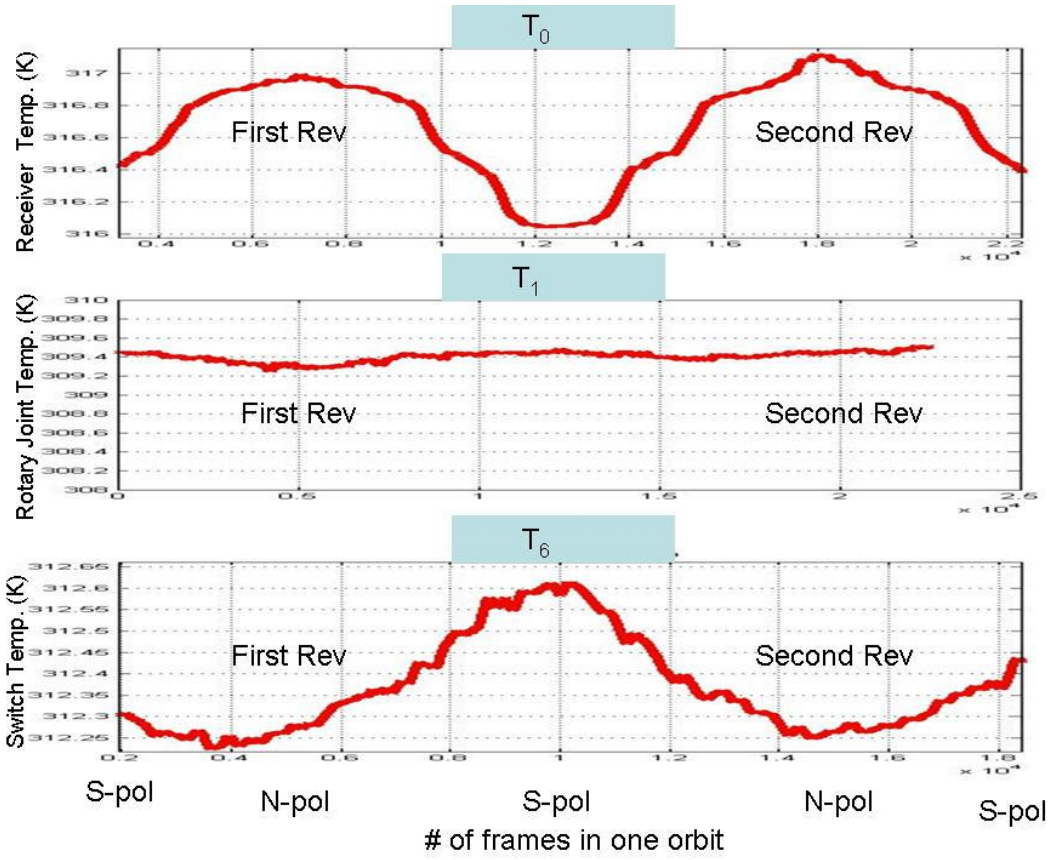

Fig. 4-23: The physical temperatures for rotary joint, switch, and receiver electronics for QRad (one orbit is 11250 frames).

4.4 QRad Evaluation Over Land

In the previous sections, the performance of QRad brightness temperatures over oceans was discussed, and this section will examine the performance of QRad Tb's over land. Over land, the average echo energy is five times larger than over oceans and Fig. 4-24 reflects this difference. Recognizing that the QRad Tb is calculated from the differential energy between the noise and echo channels: Excess Noise (N_x) = $E_n - \beta * E_e$,
which makes the differential energy calculation more critical over land and provides a worst case scenario for evaluation of the QRad transfer function.

Before comparing QRad and WindSat Tb's over land, we have to consider necessity for normalization for incidence angle and frequency. Since the dielectric characteristics of land are not spatially homogeneous and generally unknown, it is impractical to use microwave radiative transfer models to normalize the differences between QRad and WindSat. Further, because land surfaces are electromagnetically rough and emissivities are usually high (> 80%), the change in Tb with incidence angle and frequency over 10 – 15 GHz range are usually small except for open water. This means that the Tb's will be quite similar except for a small Tb offset, which should be only weakly dependent on the surface type.

For this evaluation, a 5-day (~75 revs) data set was created of QRad and WindSat Tb's over land were earth gridded in 1° pixels and averaged. These brightness temperatures images are shown in Fig. 4-25 for both QRad and WindSat (H & V pol.)

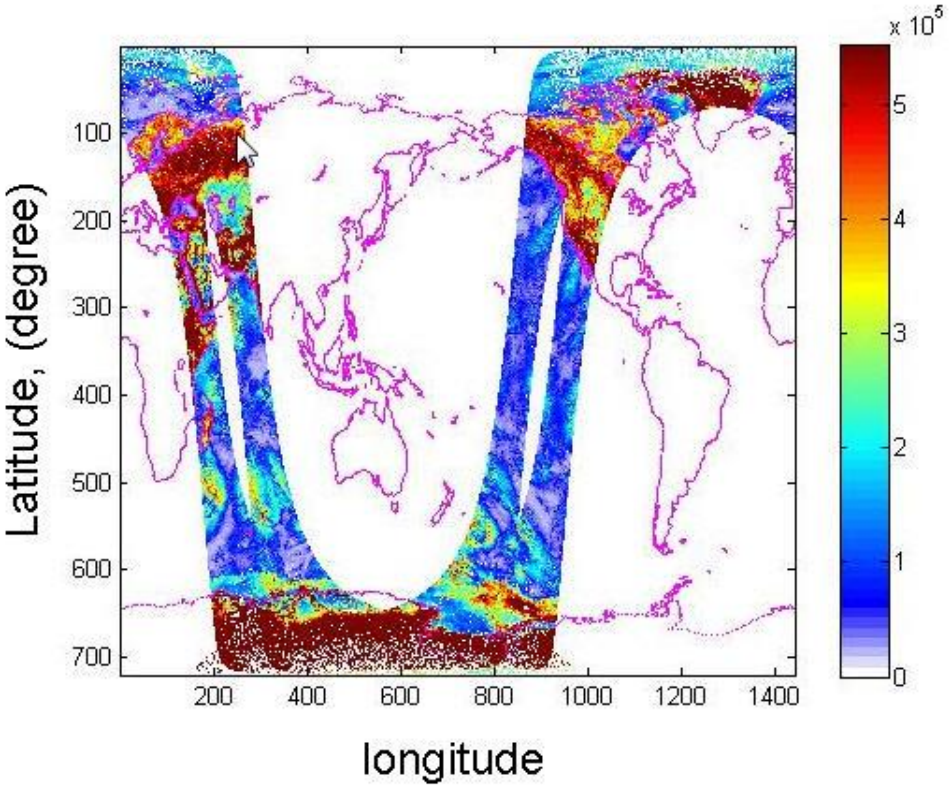

Fig. 4-24: Echo energy for two typical revolutions.

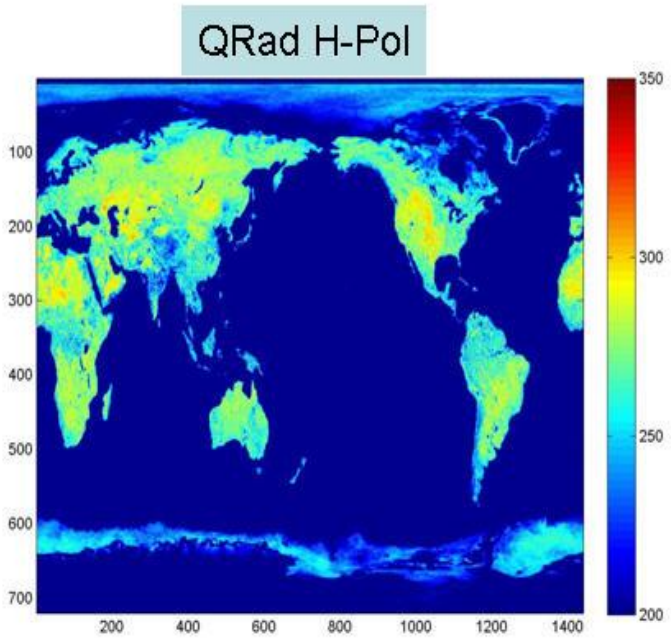

Fig. 4-25a: 5-days (August 1-5, 2005) averaged of QRad's Tb over the land.

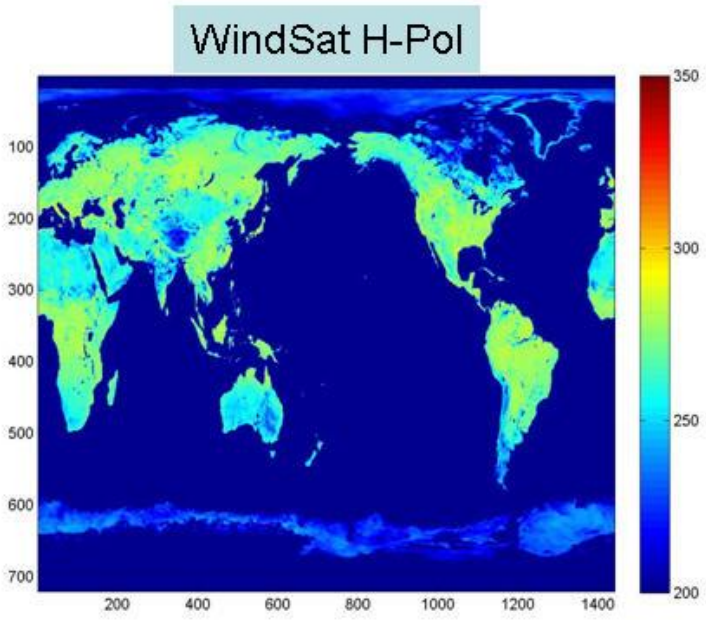

Fig. 4-25b: 5-days (Aug 1-5, 2005) averaged of WindSat's Tb over the land.

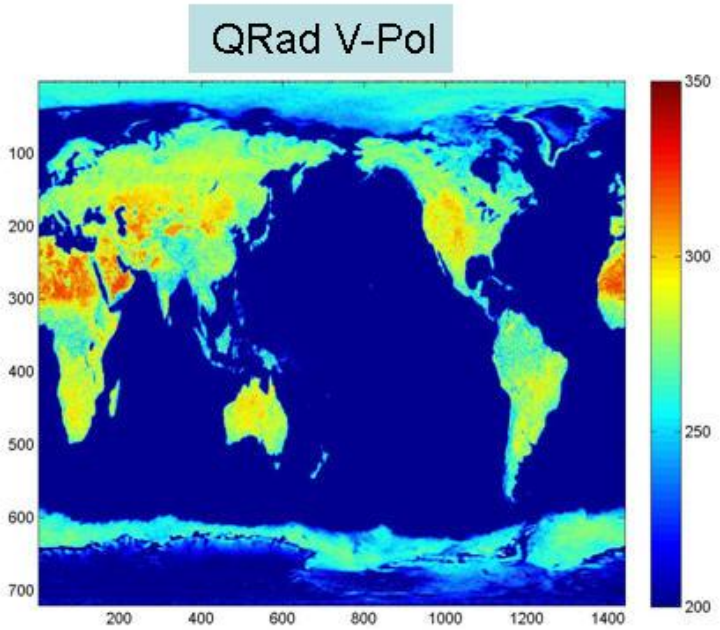

Fig. 4-25c: 5-days (Aug 1-5, 2005) averaged of QRad's Tb over the land.

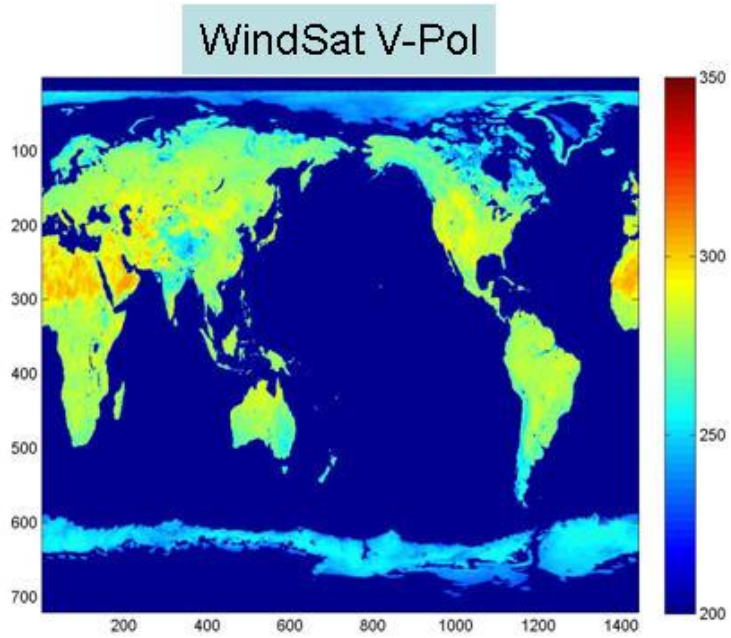

Fig. 4-25d: 5-days (August 1-5, 2005) averaged of WindSat's Tb over the land.

In this analysis, the Tb difference (ΔTb = QRad - WindSat = Tb bias) is calculated by subtracting the brightness temperatures for both polarizations (H and V), ΔTb images are shown in Fig. 4-26. In general, there are systematic differences over large regions of desert, vegetated land, and sea ice where the ΔTb's ranges between ± 20 K. For example, ΔTb is ~ -10 K (colder) over rainforest (Amazon and central Africa) and ΔTb ~ + 15 K (warmer) over deserts. So the investigation is to determine whether or not these Tb differences are caused by geophysical (dielectric) property differences or by instrumental effects?

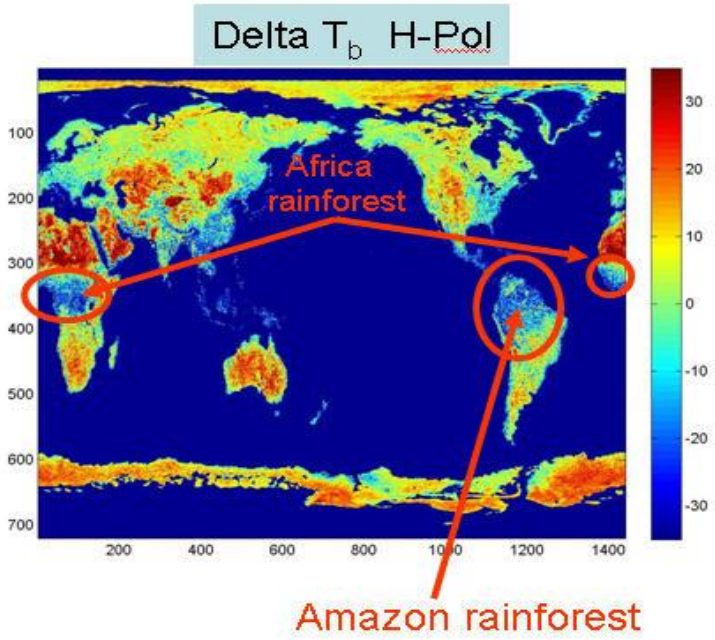

Fig. 4.26a: the difference between the QRad and WindSat T_b over the land (H-pol).

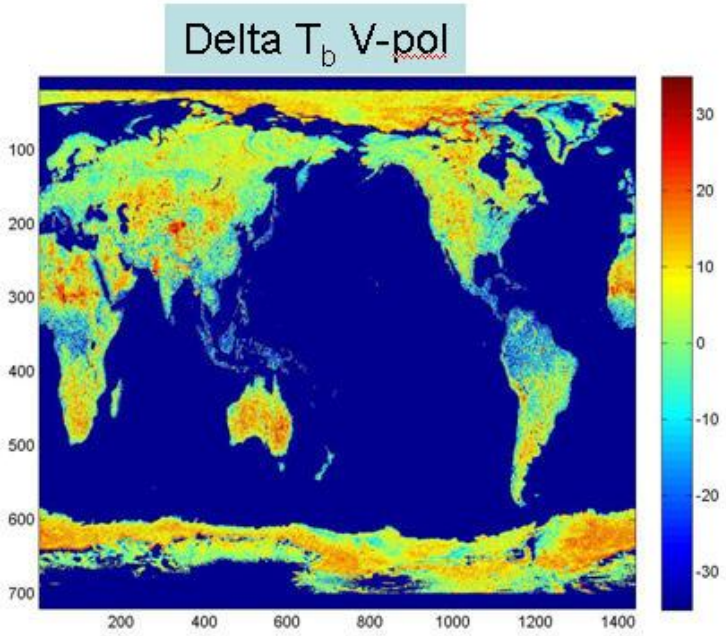

Fig. 4.26b: the difference between the QRad and WindSat Tb over the land (V-pol).

One instrumental effect, which can be easily examined, is the effect of the echo channel energy on the ΔTb. Since the echo channel energy is directly proportional to the normalized radar cross section (Sigma-0), we can test for this hypothesis by cross-correlating the images of radar reflectivity (sigma-0) and ΔTb.

To begin, we examined the transfer function

$$Nx = E_n - \beta E_e \qquad (2-23)$$

where: Beta (β) = 2.917.

The QRad Tb is proportional to the excess noise (N_x), which is the normalized difference in the energy between the noise and echo channels, where:

$$Echo\_chan\_Energy(E_e) = Gain\_echo\_chan * \tau * (radar\,signal\ power + k * T_{sys} * B_e)$$

$$Noise\_chan\_Energy(E_n) = Gain\_noise\_chan * \tau * (radar\,signal\ power + k * T_{sys} * B_n)$$

Before subtraction, the echo channel gain must first be normalized to the noise channel gain, then the signal power may be exactly cancelled in the noise channel by subtraction. If the gain normalization factor (β) is in error, then there will be a residual signal left (too much or too little). Further, this residual will be proportional to the signal power i.e., a percentage of the signal power. From the above equations, we can see that the error in excess noise (Tb bias) depends upon the residual magnitude compared to the system noise power = $k*T_{sys}*(B_n - B_e)$.

Over ocean, the radar echo channel energy is small compared to the system noise power, so the Tb bias is also small. Over land, the radar echo energy is much larger and the

residual signal after subtraction is likewise larger than the ocean case; so the Tb bias will depend upon the beta and the radar echo energy.

The transfer function given in (2-23) needs to be optimized, which occurs when the beta parameter is correct. The Beta coefficient determines the exact amount of normalized echo energy to be subtracted from the noise energy. For instance, having a high Beta value will give more weight to the echo energy in the objective function, and decrease the excess noise energy (N_x) after subtraction (i.e. the brightness temperatures are under-estimated). Similarly, a low Beta value will increase the excess noise energy (i.e. the brightness temperatures are over-estimated).

From the radar equation the echo power is proportional to the target cross section (σ):

$$P_r = \frac{X * \sigma}{R^4} \quad Where \ X = \frac{P_t G_t^{\ 2} \lambda^2}{(4\pi)^3} \tag{4-12}$$

$$\sigma = \frac{P_r * R^4}{X} \tag{4-13}$$

$$\begin{aligned} Nx &= E_n - \beta E_e = E_n - \beta P_r \tau - \beta k T_{sys} B \\ &= E_n - \frac{\beta X \sigma \tau}{R^4} - \beta k T_{sys} B_e \end{aligned} \tag{4-14}$$

A 5-day data set of land surface radar cross section (σ) was produced from the SeaWinds L2A product that was earth gridded was averaged and the results are shown in Fig. 27 for both polarizations. The results show that the σ is high over the tropical rainforest (i.e. Amazon and Central Africa tropical rainforest) and low over deserts.

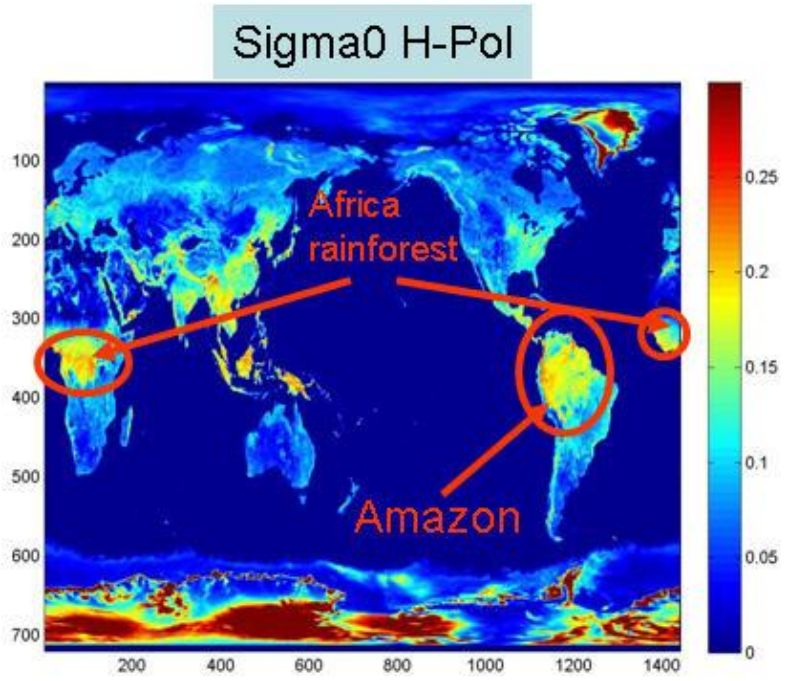

Fig. 4.27a: Normalized radar cross section over the land (H-pol.)

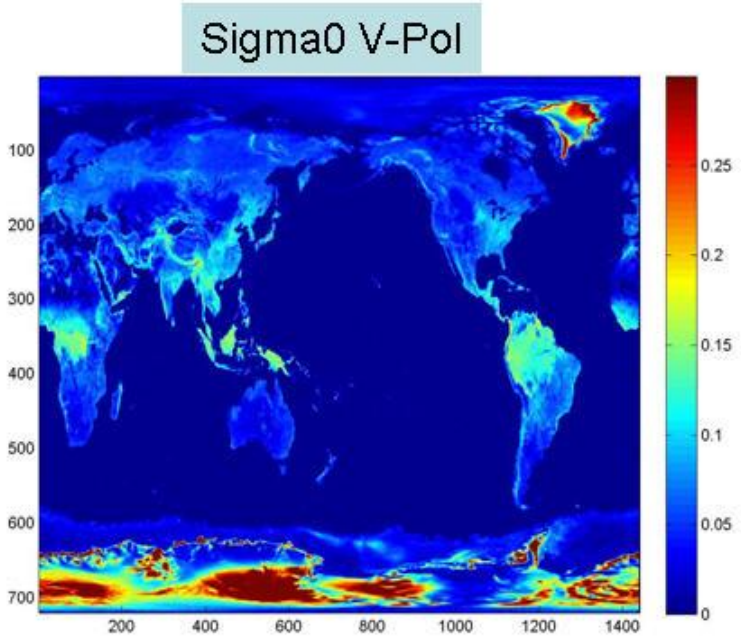

Fig. 4.27b: Normalized radar target cross section over the land (V-pol.)

By examining the images of sigma-0 and ΔTb, there seems to be an anti-correlation i.e., high sigma-0 correlated with low ΔTb bias and vice versa. We performed a cross-correlation analysis, by making scatter plots of ΔTb versus sigma-0 for land surfaces as shown in Fig. 4.28. Data were averaged using 0.01 m^2 sigma-0 bins to establish the mean trend for both polarizations. Results clearly indicate an approximately linear correlation with a negative slope for both H- and V-pol, which shows that the ΔTb is linearly proportional with respect to σ over land.

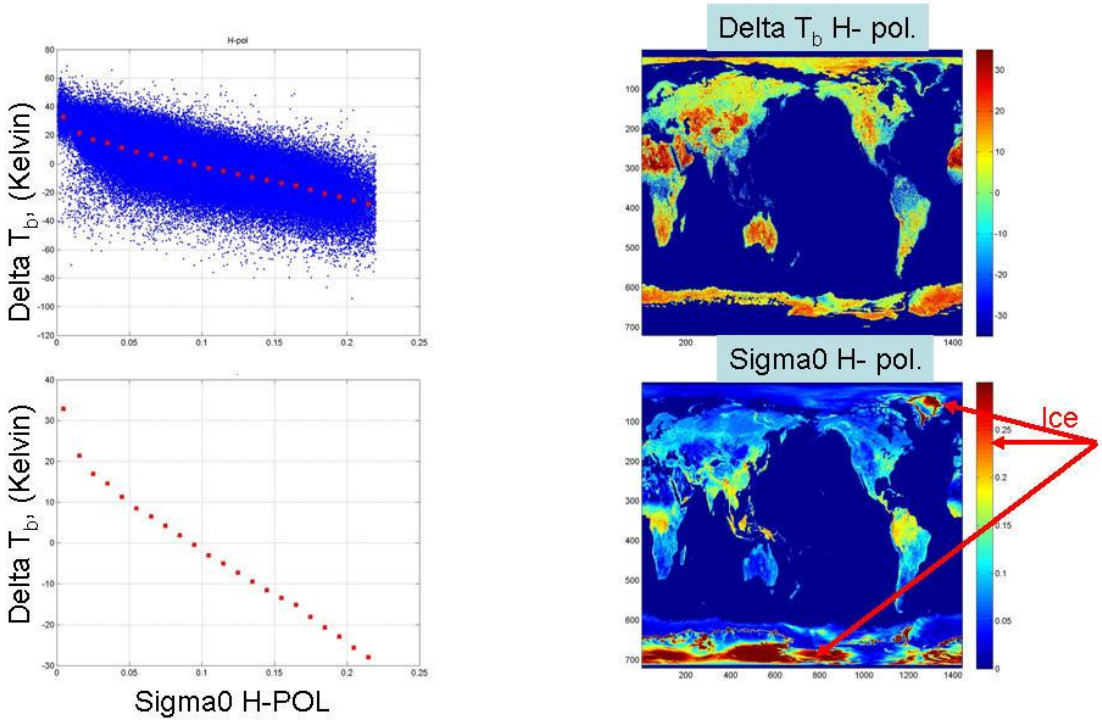

Fig. 4.28a: Relationship between surface normalized radar cross section and QRad Tb bias over the land (H-pol.).

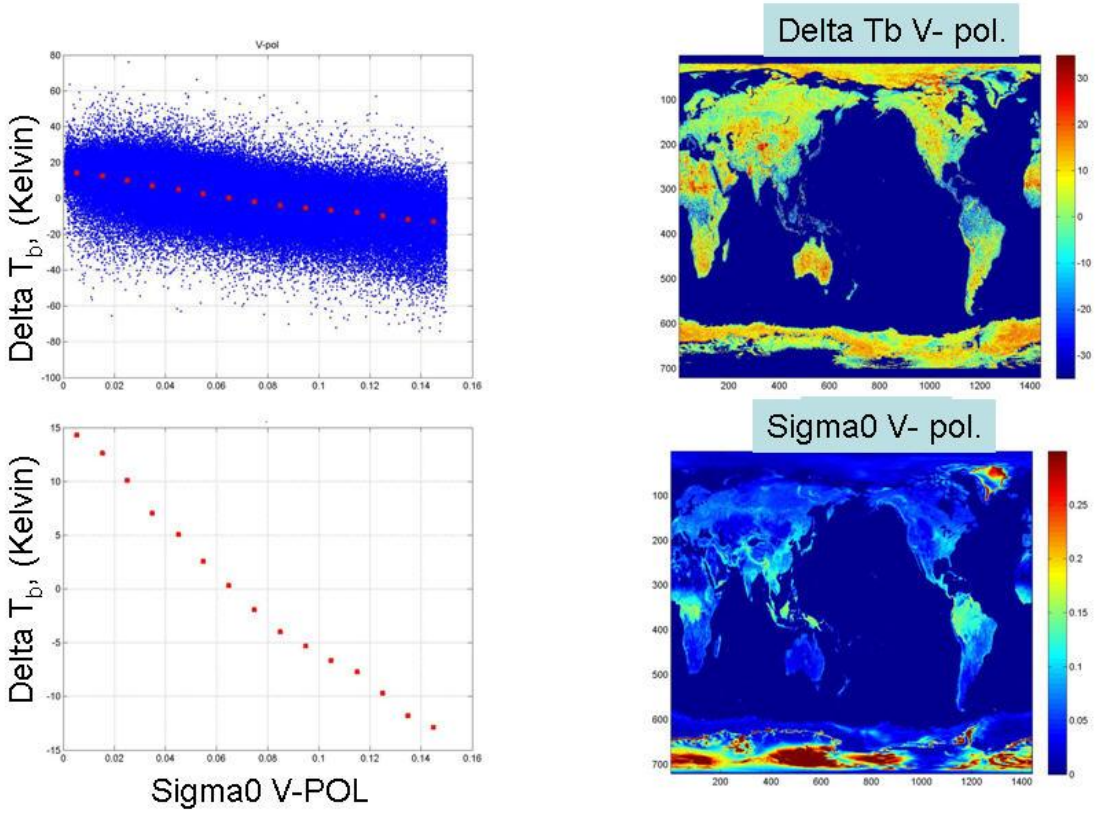

Fig. 4.28b: Relationship between surface normalized radar cross section and QRad Tb bias over the land (V-pol.).

As mentioned earlier, the transfer function given in (2-23) must be optimized to make the QRad brightness temperature independent (not correlated) with the radar cross section. This will occur when a scatter diagram of ΔTb versus sigma-0 is random or flat with zero slope. Since the Beta parameter determines the exact amount of normalized echo energy to be subtracted from the noise energy, the optimum value for beta makes the error independent of σ.

As described in chapter 2, the beta parameter is one of the inputs to the QRad algorithm, and changing the value of beta will result in a different output (brightness temperature).

QRad Tb used in this evaluation is generated by L1A and L1B data to produce the equivalent L2A brightness temperatures using our MATLAB version of the Tb algorithm. 5-days (~75 revs) were processed to generate the corresponding Tb. During the analysis, we varied the beta parameter from 2.90 to 2.92 and calculated the difference between QRad and WindSat brightness temperatures over land, and plotted these data against the surface radar cross section. This process was repeated until we obtained the optimum value of beta, which makes the difference (bias) nearly independent of σ. This optimum value was determined to be 2.914 (instead of 2.917 previously determined). Results are presented in Figs 4-29a and 4-29 b.

It is recommended that the Beta parameter be set to 2.914 for the next version of the QRad Tb algorithm.

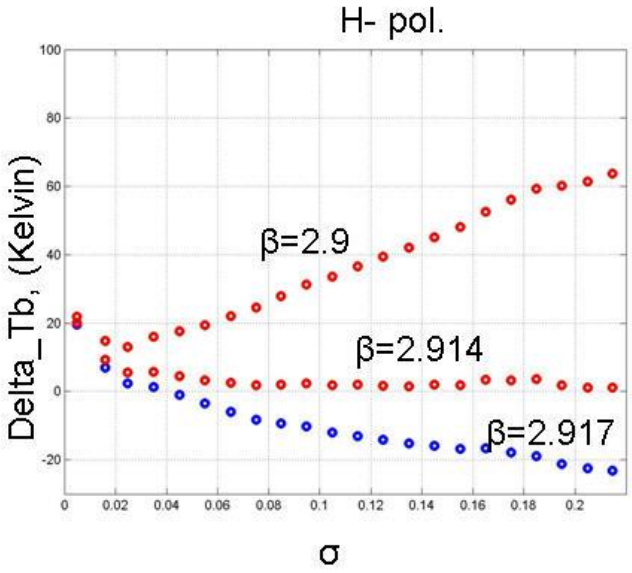

Fig.4.29a: Beta optimization for H-pol.

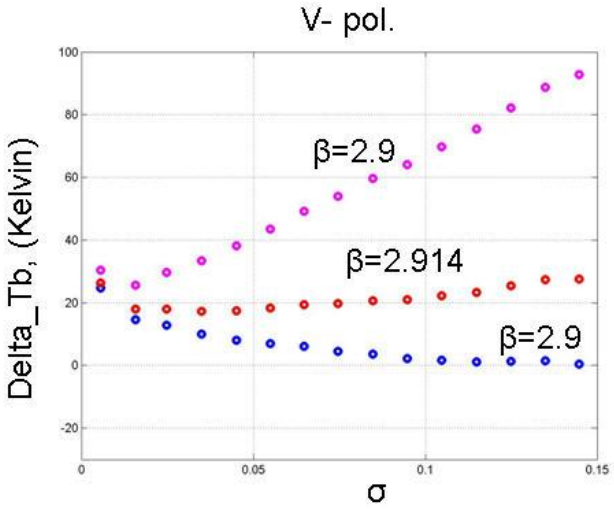

Fig.4.29b: Beta optimization for V-pol.

4.5 Antenna Pattern Effects on Ocean Brightness Temperature

As described in Chapter 2, the antenna brightness temperature is the input to the QRad transfer function. This antenna temperature is the result of the convolution of the antenna radiation pattern $F_n(\theta,\Phi)$ with the apparent brightness temperature (T_{AP}) over sphere, which surrounds the antenna. Based upon the discussion in Appendix, the antenna temperature represents the power at the output terminals of a lossless receiving antenna, T_A , and it is calculated as,

$$T_A = \eta_M T_{ML} + (1-\eta_M) T_{SL} \tag{4-3}$$

Because SeaWinds is a radar, its antenna was designed to provide peak gain and -3 dB beamwidth spatial resolution (not high beam efficiency usual for radiometer antennas); therefore, for ocean brightness temperatures near land or sea ice boundaries, there is significant "T_b contamination" due to sidelobes viewing radiometrically hot land (ice).

For this evaluation, we examined the QRad radiometric biases (QRad – Windsat_normalized) in 0.25° pixels for a ten-day period in August 2005 along the west coast of North America. This was accomplished by comparing QRad ocean Tb images with a corresponding pixel in a WindSat Tb images (as shown in Figs. 4.30a and 4.30c). Next, data were rearranged in a ΔTb series as a function of distance from land and then averaged over latitudes between 25° - 40°.

Results presented in Fig. 4.30 c shows the ocean brightness temperatures image for QRad near the West Coast of USA. The typical brightness temperatures in the open ocean are approximately 105 ~ 110 Kelvin for H-Pol. The highest brightness temperatures are observed in pixels near the land edges with values up to 135 Kelvin, which is due to the sidelobe land contamination. Results given in Fig. 4-30.d represents the brightness temperature differences between QRad and WindSat as a function of the distance from land in Km for both polarizations. As observed, the biases decrease dramatically as the antenna progressively views away from land and becomes more stable at ~ 400 km from the land. Results also show that the H-Pol Tb bias at 0 Km from land is relatively higher than the V-Pol by approximately 3 Kelvin, which is due to the fact that the sidelobe contribution is a greater percent given the lower ocean Tb at H-pol. The effect of these observations is that a conservative land mask must be used to prevent land contaminations or that an antenna pattern correction be applied using (see Appendix).

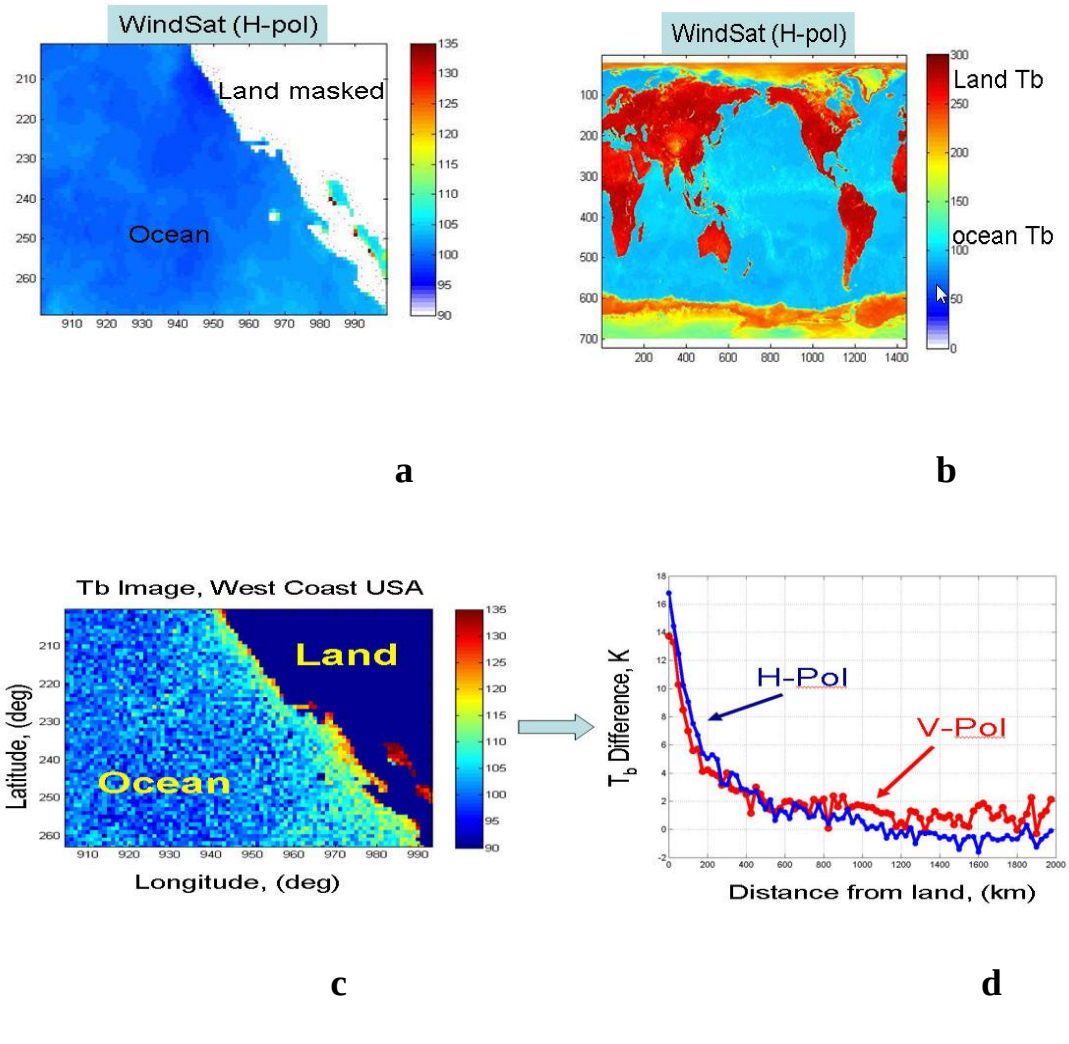

Fig. 4.30 a & c is the brightness temperature image for the west coast of America observed by WindSat, (b) is the global brightness temperature observed by WindSat, (d) is The error in brightness temperature measurement due to land contamination in the SeaWinds antenna pattern.

4.6 Noise Equivalent Differential Temperature

The noise equivalent differential temperature (NEDT) is a measure of the sensitivity of the measured Tb to changes in the scene brightness [28]. Because QRad is equivalent to a total power radiometer, we use (4-4) to calculate system NEDT as a function of the bandwidth, integration time, and system parameters.

$$NEDT = T_{sys}\sqrt{\frac{1}{B\tau}+\left(\frac{\Delta G}{G}\right)^2} \qquad (4\text{-}4)$$

Where

Tsys system noise temperature ($T_{antenna} + T_{receiever}$)

B channel bandwidth;

τ channel integration time;

G channel gain;

ΔG channel gain variation over τ.

For WindSat, the estimated NEDT is ~0.44 Kelvin for the 10.7 GHz channel, 300 MHz bandwidth, and integration time 3.93 msec [15]. In contrast, the NEDT for QRad is expected to be high due the following reasons:

1- QRad's bandwidth (~750 kHz) is much lower than WindSat (300MHz)

2- Integration time (1.8 ms) for QRad is less than half the integration time for WindSat.

To determine the QRad NEDT, we required a large number of QRad observations with constant apparent brightness temperatures to construct histograms and determine the standard deviation. This created a challenge because it was not possible to observe a long time series of QRad measurements at a constant antenna brightness temperature. Within a typical SeaWinds wind vector cell (WVC), about 6 pulses are averaged to produce the L2A brightness temperature product, which is used to estimate the system NEDT.

To estimate the value of NEDT for QRad brightness temperatures, we use (4-4):

$$NEDT\_V = T_{SYS\_V}\left(\sqrt{\frac{1}{B\tau n}} + \left(\frac{\Delta G}{G}\right)^2\right) \tag{4-5a}$$

$$NEDT\_H = T_{SYS\_H}\left(\sqrt{\frac{1}{B\tau n}} + \left(\frac{\Delta G}{G}\right)^2\right) \tag{4-5b}$$

where

G	channel gain;
Tcal	the temperature during the calibration pulses = switch temperature (T6)
En_cal	noise energy during the calibration (measured once/antenna scan)
B_n	noise channel bandwidth = 750 KHz;
τ	channel integration time = 0.0018sec;
K	Boltzmann constant =$1.38*10^{-23}$.
n	number of pulses per wind vector cell = 6 (typical)

The gain for noise channel is calculated as follows:

$$G = \frac{En\_cal}{K\tau B_n T_{cal}} \tag{4-6}$$

To calculate the ΔG/G, we can examine the receiver noise channel output energy during the internal load calibration (cal pulse), which occurs once per antenna scan. Over one orbit, there are ~11,250 samples of this parameter which are used to construct a time series. Because the internal load temperature is nearly constant over an orbit, and because the receiver gain is also stable in the mean, we can estimate the ΔG/G as the standard deviation of the noise cal pulse time series:

$$\frac{\Delta G}{G} = \frac{std(G)}{<G>} - mean(T_{cal}) * \left(\sqrt{\frac{1}{B_n * \tau * n}} \right)^2 = 0.021 \tag{4-7}$$

During the noise calibration measurement, the system noise temperature for V- pol. is:

$$Tsys\_v = <T_b\_v> * L_{sys} + (1 - L_{sys}) T_{ph} + T_r = \sim 635 Kelvin$$
$$where: L_{sys} = \mathrm{L1A} * \mathrm{L4} * \mathrm{L5} * \mathrm{L6} \tag{4-8}$$

and the system noise temperature for H- pol. is:

$$Tsys\_H = <T_b\_H> * L_{sys} + (1 - L_{sys}) T_{ph} + T_r = \sim 593 Kelvin$$
$$where: L_{sys} = \mathrm{L1B} * \mathrm{L4} * \mathrm{L5} * \mathrm{L6} \tag{4-9}$$

Then NEDT was solved for both polarizations (H and V) as followed:

$$NEDT\_V = 635 \left(\sqrt{\frac{1}{750{,}000 * 0.0018 * 6}} + (0.021)^2 \right) = 15.08 Kelvin \tag{4-10a}$$

$$NEDT\_H = 593\left(\sqrt{\frac{1}{750{,}000*0.0018*6}+(0.021)^2}\right) = 14.09\,Kelvin \qquad (4\text{-}10b)$$

where the mean value for Tsys for V-pol = ~635 Kelvin and H-pol = ~593 Kelvin,

The variance analysis used individual L2A T_b*'s* that were collocated in 1° boxes and the standard deviation about the mean computed for each box to produce samples of differences (δT_b) defined as

$$\delta T_b = \mathrm{Tb}_{\_QRmeas} - \langle T_{b\_QRmeas} \rangle \qquad (4\text{-}11)$$

where Tb_QRmeas is the L2A Tb measurement and <Tb_QRmeas> is the mean brightness temperature for each 1° box. The histogram for ~ 50,000 samples (from month of August) was found to be a zero mean Gaussian and the resulting NEDT was 15.6 K for V-pol (Fig. 4.31 a) and 12.5 K for H-pol (Fig. 4.31 b), which compares well with the instrument noise (NEDT) averaged over a WVC, plus a few Kelvin of additional variation due to other spatial, temporal, and geophysical variation in each data set .

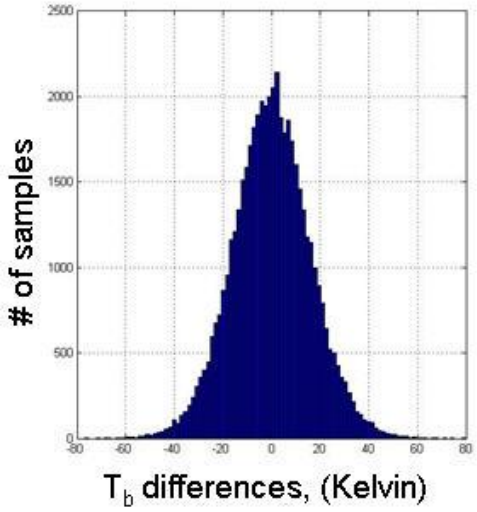

Fig. 4.31a: Histogram of 1° box differences (δTb) for QRad

Typical orbit in August 2005 (V -Pol).

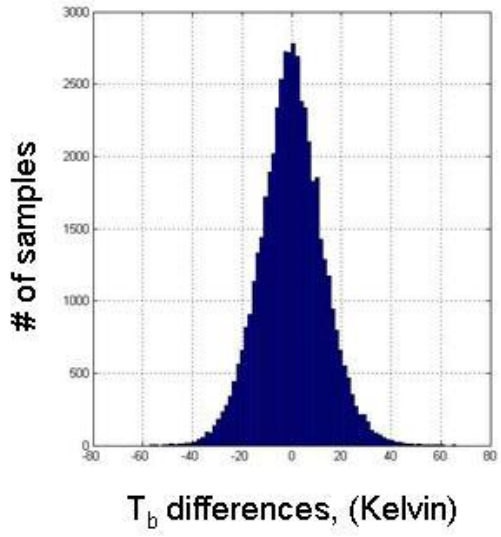

Fig. 4:31b: Histogram of 1° box differences (δTb) for QRad

Typical orbit in August 2005 (H -Pol).

To examine the stability of these results, the same procedure was performed for 3 different seasons (fall, winter, summer). Results show that it is very consistent with only a small variation less than 0.5 K and 0.3K for V and H-Pol, respectively, as shown in Table 4-3.

Table 4-3: The standard deviation for QRad T_b

Month	**V-pol**	**H-pol**
January	15.99 K	12.72 K
August	15.59 K	12.52 K
November	16.15 K	12.98 K

CHAPTER 5: SUMMARY AND CONCLUSIONS

After the launch of NASA's SeaWinds scatterometer in 1999, a radiometer transfer function (QRad) was provided by Central Florida Remote Sensing Lab (CRSL), and implemented in the Science Ground Data Processing Systems to allow the measurement of the earth's microwave brightness temperature. QRad brightness temperatures are used to infer rain rate over the oceans, which can be used as a quality flag for wind vector retrievals of SeaWinds. The purpose of this dissertation was to evaluate the QRad's transfer function by determining how well the algorithm works during sunlit orbits and eclipse periods.

5.1 Summary of QRad Evaluation

5.1.1 QRad Evaluation During Sunlit Orbits

To assess the quality of the QRad instrument and to calibrate it, we compared the QRad derived brightness temperatures with the near simultaneous observations from WindSat (calibration standard). Since QRad operates at 13.4 GHz with incidence angles 54˚ (V-pol) and 46˚ (H-pol) and the closest WindSat channel is 10.7 GHz at an incidence angle of 50.3°, T_b normalizations (i.e. compensation for the difference in frequency and the incident angle between the QRad and WindSat T_bs) were required before comparisons were made. To accomplish this, a radiative transfer model (RTM) was used to transform the WindSat 10.7 GHz measurements to the equivalent at 13.4 GHz and the

corresponding QRad incidence angles. The RTM estimates brightness temperature (T_b) for a specific operating frequency and the incidence angle, as a function of 14 physical properties of the ocean and intervening atmosphere.

To assess the ability of the RTM to accurately predict the WindSat brightness temperatures for normalization purposes, we compared measured and modeled WindSat *T_b's* for both polarizations. To demonstrate the process of creating the match-up datasets, zonal averages were performed over full 360˚ longitude using 1° latitude bins. Results indicate excellent agreement over all latitudes between +/-50 degree which is important because our analysis considers QRad biases as a function of orbit position.

Brightness temperatures for nine months during 2005 and 2006 were spatially collocated for rain-free homogeneous ocean scenes (match-ups) within 1° latitude x longitude boxes and within a ± 60 minute window. To ensure high quality comparison, these collocations were quality controlled and edited to remove non-homogenous ocean scenes and/or transient environmental conditions, including rain contamination. WindSat and QRad Tb's were averaged within 1° boxes and these were used for the radiometric inter-calibration analysis on a monthly basis. Results show that QRad calibrations during sunlit orbits are stable in the mean within ± 2K over the yearly seasonal cycle.

5.1.2 QRad Evaluation during Eclipse

The performance of QRad during the eclipse periods was examined by comparing with WindSat for the month of January 2006. The results show that the corresponding Tb_biases for ascending (pre-eclipse) and descending (post-eclipse) orbit segments at 50° N latitude differ by -6K for V-pol and -8 K for H-pol. After exiting eclipse, the biases on the descending portion of the orbit gradually approach the ascending bias values. The biases converge at the equator and remain approximately equal in the southern hemisphere, which is similar to the previous results during the continuous sunlight conditions.

QRad was evaluated during the maximum eclipse period, where the duration was approximately constant. In this analysis, we have examined the dynamic bias as a function of time. Results indicate that when the satellite enters into eclipse, there is a monotonic increase in the bias (more negative by 12 K) until the satellite re-enters sunlight, the bias decreases at approximately the same rate until it reached equilibrium near the equator. This time-variable orbital bias pattern agrees with our expectation of the reflector physical temperature cooling during the dark portion of the orbit and of the heating of the reflector when it is exposed to the sunlight.

5.1.3 QRad Evaluation near the land

QRad was then examined to determine the antenna pattern effects on ocean brightness temperature. Because SeaWinds is a radar, its antenna pattern was designed to provide spatial resolution and not the high beam efficiency usual for radiometer antennas; therefore there is significant "T_b contamination" for pixels near land. Our results show that the biases decrease dramatically as the measurement cell moves away from land and asymptotically approaches an equilibrium at ~ 400 km from the land.

5.1.4 QRad Evaluation over the land

The performance of QRad brightness over land was examined using inter-comparison with WindSat Radiometer. The land provides a worse case scenario for evaluation of the QRad transfer function. In this evaluation, QRad's T_bs were averaged and compared with the WindSat satellite radiometer and the ocean T_b s were removed, to get the comparison only over land. Our findings indicate that the QRad's brightness temperatures over a hot target was under estimated, and over estimated within a desert area like North Africa. This discrepancy was corrected by tuning value of beta; the optimum value of beta was 2.914 instead of 2.917.

5.1.5 NEDT

In this dissertation, the NEDT in QRad measurements was estimated for both inner and outer beam (V and H-pol.). The NEDT for the L2A Tb product (25 km wind vector cell average) was ~15.6 K for V-pol and ~12.5 K for H-pol.

5.2 Conclusion

In summary, an inter-satellite radiometric calibration was performed to assess the quality of QRad radiometric (brightness temperature) calibration using a comparison of near-simultaneous ocean brightness temperature (Tb) between QRad and WindSat radiometer on Coriolis. Results show that QRad calibrations during sunlit orbits are stable in the mean within ± 4K over the yearly seasonal cycle. Results also indicate that during the eclipse period, which runs between mid-November and the end of January, transient cooling of front-end losses cause time-varying calibration biases that are linearly proportional to the eclipse duration.

5.3 Future Work

The evaluation of QRad's brightness temperatures in this dissertation confirmed that the present value of the gain ratio (β) is off by 0.003. Therefore the correct value of β=2.914 (the input of QRad transfer function) should be provided to JPL to reprocess the L2A

product and generate the new Tb. Then, similar analyses should be performed to validate that the systematic biases during sunlit orbits have been minimized. Also, analyses should be performed to estimate the front-end physical temperatures using solar beta angles and time after entering eclipse.

APPENDIX: ANTENNA BRIGHTNESS TEMPERATURE

APPENDIX: ANTENNA BRIGHTNESS TEMPERATURE

As described in Chapter 2, the antenna brightness temperature is the input to the QRad transfer function. This antenna temperature is the result of the convolution of the antenna radiation pattern $F_n(\theta,\Phi)$ with Aperture Antenna temperature (T_{AP}) over sphere, which surrounds the antenna as seen in (A-1a). According to Ulaby, Moore and Fung [18],

$$T_A = \frac{\iint_{4\pi} T_{Ap}(\theta,\phi) F_n(\theta,\phi) * \sin\theta d\theta d\phi}{\iint_{4\pi} F_n(\theta,\phi) * \sin\theta d\theta d\phi} \qquad \text{(A-1a)}$$

The perfect design for any radiometer's antenna is having a very narrow pencil beam and no sidelobes. Practically, in addition to the emission received through the main beam of the antenna, the antenna receives other contributions through the remainder of the antenna pattern as shown in Fig.A-1. To investigate the significance of these undesirable contributions on QRad, let us split the numerator of (A-1a) into two parts, the first part for the main beam and the second represents the contributions received in other directions outside the antenna main lobe:

$$T_A = \frac{\iint_{\text{main-lobe}} T_{Ap}(\theta,\phi) F_n(\theta,\phi) * \sin\theta d\theta d\phi}{\iint_{4\pi} F_n(\theta,\phi) * \sin\theta d\theta d\phi} + \frac{\iint_{4\pi\text{-main-lobe}} T_{Ap}(\theta,\phi) F_n(\theta,\phi) * \sin\theta d\theta d\phi}{\iint_{4\pi} F_n(\theta,\phi) * \sin\theta d\theta d\phi} \qquad \text{(A-1b)}$$

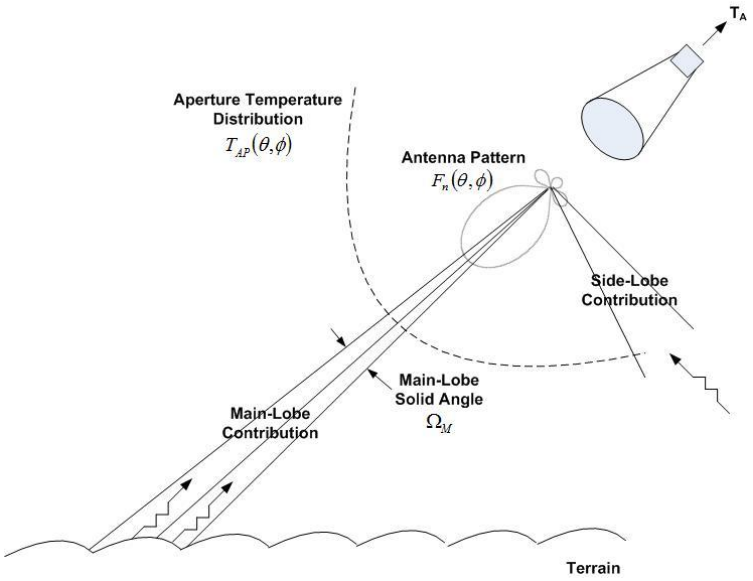

Fig. A-1: Main lobe and side lobe contribution to the antenna temperature by Ulaby, Moore and Fung [18].

We will refer to the second term in Equation A-1b as the side-lobe contribution. Next we will introduce the quantity of the effective apparent temperature (T_{ML}) of the main-lobe contribution,

$$T_{ML} = \frac{\iint_{\text{main-lobe}} T_{Ap}(\theta,\phi) F_n(\theta,\phi) * \sin\theta d\theta d\phi}{\iint_{main-lobe} F_n(\theta,\phi) * \sin\theta d\theta d\phi} \qquad \text{(A-2)}$$

Antenna Main Beam Efficiency, η_m , was defined as,

$$\eta_M = \frac{\iint_{\text{main-lobe}} \mathrm{F_n}(\theta,\phi) * \sin\theta \mathrm{d}\theta \mathrm{d}\phi}{\iint_{4\pi} \mathrm{F_n}(\theta,\phi) * \sin\theta \mathrm{d}\theta \mathrm{d}\phi} \tag{A-3}$$

$$\eta_{SF} = \frac{\iint_{4\pi\text{-main-lobe}} \mathrm{F_n}(\theta,\phi) * \sin\theta d\theta \mathrm{d}\phi}{\iint_{4\pi} \mathrm{F_n}(\theta,\phi) * \sin\theta \mathrm{d}\theta \mathrm{d}\phi} = 1 - \mu_M \tag{A-4}$$

Then the new definition for the antenna temperature represents the power at the output terminals of a lossless receiving antenna, T_A , and it is calculated as,

$$T_A = \eta_M T_{ML} + (1 - \eta_M) T_{SL} \tag{A-5}$$

For an ideal antenna with radiation efficiency = 1 and main beam efficiency = 1 reduces the T_A to T_{ML} .The typical value for the main beam efficiency for any radiometer is > 90% (e.g. WindSat has 95% beam efficiency). However, the antenna beam efficiency for a typical radar is much lower (60 - 80%).

LIST OF REFERENCES

[1] Rushad J. Mehershahi "Ocean Brightness Temperature Measurements using Quickscat Radiometer", M.S. Thesis, Univ. Central Florida, June 2000.

[2] Maladen Susanj "An Algorithim for measurements Rain over oceans using the QuikSCAT Radiometer", M.S. Thesis, Univ. Central Florida, August 2000.

[3] Yanxia Wang "A Statistical Algorithm for inferring Rain Rate from the QuickScat Radiometer", M.S. Thesis, Univ. Central Florida, December 2001

[4] Khalil Ahmad, W. Linwood Jones, Takis Kasparis, Stephen Vergara, Ian Adams and Jun Park, "Oceanic Rain Rate Estimates from the QuikSCAT Radiometer: A Global Precipitation Mission Pathfinder", J. GeoPhy. Res – Atms, VOL. 110, 2005.

[5] Ahmad, Khalil A., Jones, W. Linwood and Takis Kasparis, "QuikSCAT Radiometer (QRad) Rain Rates for Wind Vector Quality Control", Proc. Oceans 2005 MTS/IEEE, Sept. 20-22, 2005, Wash DC.

[6] Khalil Ahmad, W. Linwood Jones and Takis Kasparis, "An Improved Oceanic Rainfall Retrieval Algorithm for the SeaWinds Scatterometer ", Proc. IEEE IGARSS 08, Jul. 6 - 11, 2008, Boston, MA.

[7] Khalil A. Ahmad, Estimation of Oceanic Rainfall using Passive and Active Measurements from SeaWinds Spaceborne Microwave Sensor. Ph.D. dissertation, Univ. Central Florida, 2004.

[8] Rastogi, Mayank, Jones, W, Linwood and Ian Adams, "SeaWinds Radiometer (SRad) on ADEOS-II Brightness Temperature Calibration/Validation, Proc. IEEE

IGARSS-05, July 25-29, 2005, Seoul, Korea.

[9] Hanna, R; Jones, W.L., "Brightness Temperature Validation for SeaWinds Radiometer using Advanced Microwave Scanning Radiometer on ADEOS-II", Proc. IEEE IGARSS-05, July 25-29, 2005, Seoul, Korea.

[10] Jones,W. L., Mehershahi, R., Zec, J. and D. G. Long, "SeaWinds on QuikScat Radiometric Measurements and Calibration", Proc. IEEE IGARSS'00, July 24-28, 2000, Honolulu, HA

[11] Hong, Liang, "Inter-satellite Microwave Radiometer Calibration", Ph.D. dissertation, Univ. Central Florida, 2004.

[12] Hong, Liang, Jones, W. Linwood, Wilheit, Thomas T. and Takis Kasparis, " Two Approaches for Inter-satellite Radiometer Calibrations between TMI and WindSat", *J. of Meteorological Society of Japan*, Vol. 87A, pp. 223-235, 2009.

[13] Gopalan, Kaushik, "A Time-Varying Radiometric Bias Correction for the TRMM Microwave Imager", Ph.D. dissertation, Univ. Central Florida, 2008.

[14] Kaushik Gopalan, Linwood Jones, Sayak Biswas, Steve Bilanow, Thomas Wilheit and Takis Kasparis, "A Time-Varying Radiometric Bias Correction for the TRMM Microwave Imager, *IEEE Trans. GeoSci. Rem. Sens*, vol. 99, NO. 1, Oct 2009.

[15] Peter W. Gaiser, Karen M. St. Germain, Elizabeth M. Twarog, Gene A. Poe, William Purdy, Donald Richardson, Walter Grossman, W. Linwood Jones, David Spencer, Gerald Golba, Jeffrey Cleveland, Larry Choy,Richard M. Bevilacqua, and Paul S. Chang, "The WindSat Spaceborne Polarimetric Microwave

Radiometer: Sensor Description and Early Orbit Performance" *IEEE Trans Geosci. Rem. Sens*, Vol. 42, No. 11, Nov 2004.

[16] W. Linwood Jones, Jun D. Park, Seubson Soisuvarn, Liang Hong, Peter Gaiser and Karen St. Germain, "Deep-Space Calibration of WindSat Radiometer", *IEEE Trans. GeoSci. Rem. Sens.*, Vol. 44, N0. 3, Mar 2006, pp. 476-495.

[17] http://dss.ucar.edu/datasets/ds461.0/, "U.S. National Centers for Environmental Prediction, updated monthly: NCEP ADP Global Surface Observational Weather Data, daily, April 2000 - continuing. *Dataset ds461.0 published by the CISL Data Support Section at the National Center for Atmospheric Research, Boulder, CO,."*

[18] F. T. Ulaby, R. K. Moore, and A. K. Fung, Microwave Remote Sensing: Active and Passive, vol. 1, chap 4 & 5, Norwood, MA: Artech House Publishers, 1981.

[19] P. W. Rosenkranz, "Shape of the 5 mm oxygen band in the atmosphere," *IEEE Trans. Antennas Propag*, vol. AP-23, pp. 498-506, 1975.

[20] P. Rosenkranz, "Water vapor microwave continuum absorption: A comparison of measurements and models," *Radio Science*, vol. 33, pp. 919 - 928, 1998.

[21] P. W. Rosenkranz, "Absorption of Microwaves by Atmospheric Gases," in *Atmospheric Remote Sensing By Microwave Radiometry*, M. A. Janssen, Ed., 1993, pp. 37–+.

[22] H. J. Liebe and D. H. Layton, "Millimeter-wave properties of the atmosphere: Laboratory studies and propagation modeling," Nat. Telecomm. and Inf. Admin., Boulder, Colorado NTIA Rep. 87-224, 1987.

[23] H. J. Liebe, P. W. Rosenkranz, and G. A. Hufford, “Atmospheric 60-GHz oxygen spectrum: New laboratory measurements and line parameters,” *J. Quant. Spectrosc. Radiat. Transfer*, vol. 48, pp. 629 - 643, 1992.

[24] G. Elsaesser, “A parametric optimal estimation retrieval of the non-precipitating parameters over the global oceans”, Master’s Thesis, Colorado State University, Fort Collins, 2006.

[25] T. Meissner and F. Wentz, “The complex dielectric constant of pure and sea water from microwave satellite observations,” *IEEE Trans on Geosci and Rem Sens*, vol. 42, no. 9, pp. 1836–1849, Sept. 2004.

[26] "Annual Mean Salinity (PSS) at the Surface," World Ocean Atlas 2001, Ocean Climate Laboratory/NODC.

[27] Private communication: JPL thermal engineering, SeaWinds CDR package.

[28] F. T. Ulaby, R. K. Moore, and A. K. Fung, Microwave Remote Sensing: Active and Passive, vol. 1, chap 6, Norwood, MA: Artech House Publishers, 1981.